Author:
Gumussoy Girgin, Merve

Title:
Synthesis of pyridine-based conjugated microporous polymers for CO capture and conversion

SYNTHESIS OF PYRIDINE-BASED CONJUGATED MICROPOROUS POLYMERS FOR CO_2 CAPTURE AND CONVERSION

BY

MERVE GUMUSSOY GIRGIN

School of Chemistry

UNIVERSITY OF BRISTOL

A dissertation submitted to the University of Bristol in accordance with the requirements for award of the degree of MASTER BY RESEARCH in the Faculty of Science

July 2022

Word count: Twenty four thousand one hundred and eighty-eight

“Çoğu insan zekaya inanır, ben inanmıyorum. Bizi birbirimizden ayıran emektir, ben çalışmaya inanıyorum”

– Aziz Sancar

Abstract

In this study, novel nitrogen-rich conjugated microporous polymers (CMPs) based on pyridine derivatives were synthesised and investigated for CO_2 capture and conversion applications. The CMPs were synthesised via Buchwald-Hartwig cross-coupling reaction, where ratios of monomers were varied to tune their properties. The synthesized polymers were characterised using X-Ray Diffractometry (XRD), UV-Vis-NIR spectroscopy, FT-IR spectroscopy, and scanning electron microscopy (SEM) methods. The total surface area of the materials were determined by the Brunauer–Emmett–Teller (BET) method, and the pore size distributions (PSD) determined by nonlocal density functional theory (NLDFT) method. Surface areas up to 75 m^2/g^{-1} were found for these novel CMPs. To understand and find an optimal solvent for the synthesis to optimise the yield and surface area, solubilities of CMPs were evaluated by calculating the Hansen solubility parameters (HSPs). Determination of HSPs relies on the interaction between the solvent and polymer by the influence of three major intermolecular interactions; dispersion interaction (δ_D), hydrogen-bonding component (δ_H), and permanent dipole-dipole interaction (δ_P). This approach, the so-called Bristol-Xi'an Jiaotong (BXJ) approach, did not yield conclusive results in terms of tuning surface areas or PSDs. Finally, exploiting the presence of the well-known metal-binding motifs incorporated in the CMPs, metal-containing CMPs were also prepared. The effects on porosity and CO_2 uptake properties by direct cross-coupling with metal–organic co-monomers, and post-synthesis functionalized CMPs, treated with a metal, were investigated. The synthesised metal-containing CMPs showed a massive increase in the surface area of up to 229 m^2/g^{-1}, and CO_2 uptake of up to 5.7 wt%. The electrocatalytic CO_2 reduction and adsorption properties of the synthesised polymers were investigated, with initial results showing opportunities for CO_2 conversion using these novel functional CMP systems.

Key words: Conjugated microporous polymers, Hansen solubility parameters, Metal-containing CMPs, CO_2 capture, CO_2 conversion

Acknowledgements

This study was carried under the assistance of General Directorate of the Mineral Research & Exploration of Turkey, funded by the Republic of Turkey Ministry of National Education. I thank them for supporting me through my education and making my dreams come true.

I would like to express my deepest appreciation to my supervisor, Prof. Charl FJ Faul, for his marvellous supervision, guidance and encouragement. Sincere gratitude is extended to his generous participation in guiding, constructive feedback, kind support, and advice during every step of my MRes study. I would like to thank Prof. Charl for offering me a place for joining the Faul Research Group. I improved my chemistry knowledge even more and gained a lot of confidence in myself which has ultimately helped me to get where I am now by joining the group.

Next, I would like to thank my colleagues in Faul Research Group for their willingness to impart their knowledge in all matters. It has been an honour and pleasure for me to be part of this group, and to meet and work with so many talented scientists. I would especially like to thank my lab colleagues Safa Ali Al Siyabi, Nouf Zaghloul, Neha Yadav, Ulzhalgas Karatayeva for their invaluable friendship and support, Basiram Brahma Narzary, Xue Fang and Maximilian Hagemann for all the great guidance. I also thank my APM assessor Dr Sébastien Rochat for offering lots of advice in the development of this project.

I would like to thank all the staff and teams helping with the instrumental and theoretical work. Many thanks to Dr Jean-Charles Eloi from School of Chemistry's Imaging Facility; and Dr Natalie E. Pridmore from Structural Chemistry Laboratory.

I am grateful for my lovely parents, whose constant love and support keep me motivated and confident. No words are adequate to express my indebtedness to them. Deepest thanks to my siblings Münevver and Arif, who keep me grounded, remind me of what is important in life, and are always supportive in my adventures. Finally, I owe my deepest gratitude to my wonderful husband Hakan, who I am forever thankful for his infinite love and support throughout the entire thesis process and every day.

Author’s Declaration

I declare that the work in this dissertation was carried out in accordance with the requirements of the University's Regulations and Code of Practice for Research Degree Programmes and that it has not been submitted for any other academic award. Except where indicated by specific reference in the text, the work is the candidate's own work. Work done in collaboration with, or with the assistance of, others, is indicated as such. Any views expressed in the dissertation are those of the author.

SIGNED: ..... DATE:.....

Table of Contents

List of Figures

List of Schemes

List of Tables

List of Abbreviations

Table 1 List of abbreviations

Abbreviation	Full name
ACN	Acetonitrile
°C	Degree Celsius
BET	Brunauer–Emmett–Teller
B-H Coupling	Buchwald-Hartwig coupling
BP	4,4'-dibromo-2,2'-bipyridine
CMPs	Conjugated microporous polymers
COF	Covalent-organic framework
CO_2RR	CO_2 Reduction Reaction
DMF	N,N-dimethylformamide
DMSO	Dimethyl sulfoxide
EDX	Energy Dispersive Energy X-ray
EtOH	Ethanol
i-PrOH	Isopropanol
IUPAC	International Union of Pure and Applied Chemistry
FT-IR	Fourier transform infrared spectroscopy
GHG	Greenhouse gases
HSPs	Hansen Solubility Parameters
MALDI	Matrix-assisted laser desorption/ionization
MOF	Metal-organic framework
nm	Nanometre
NMP	N-Methyl-2-pyrrolidone
POPs	Porous Organic Polymers
PTPA	Poly(triphenylamine)
$Pd(dba)_2$	Bis (dibenzylideneacetone) palladium(0)
PPDA	p-phenylenediamine
PSD	Pore size distribution

PXRD	Powder X-ray diffraction spectroscopy
Ph-	Phenyl (functional group)
RHE	Reversible hydrogen electrode
RT	Room Temperature
SEM	Scanning Electron Microscopy
SCE	Saturated calomel electrode
TBPA	tris(4-bromophenyl)amine
THF	Tetrahydrofuran
TP	4'-(4-bromophenyl)-2,2':6',2''-terpyridine
NaOtBu	Sodium tert-butoxide
UV-Vis-NIR	Ultraviolet–visible-near infrared spectroscopy
XPhos	2-Dicyclohexylphosphino-2’,4’,6’-triisopropylbiphenyl
λ	Wavelength

1. Introduction

In accordance to NASA, the average temperature on Earth has increased by at least 1.1 °C since 1880 (Figure 1).[1] Long-term change in the average weather patterns is unfortunately leading to a global warming. This is mainly caused by human activities such as burning fossil fuels and deforestation, which is leading to an increase in the concentration of greenhouse gases (GHG) within the atmosphere. GHG, such as carbon dioxide (CO_2), methane (CH_4), nitrous oxide (N_2O) and fluorinated gases, trap the heat in the atmosphere by absorbing the thermal radiation emitted by the Earth's surface and raises the average temperature of the planet.[2, 3]

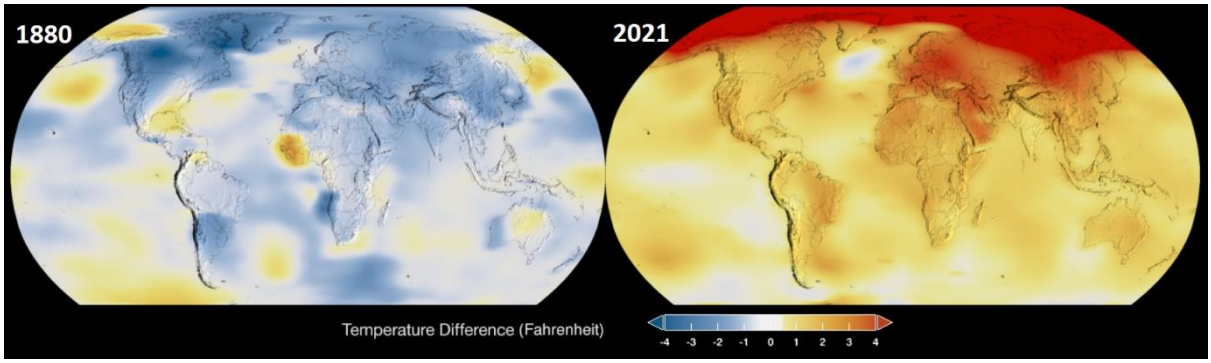

Figure 1 The temperature change of the Earth's surface from 1880 to 2021. Reproduced from reference [4]

During the past decades, the atmospheric CO_2 concentration has massively increased to become the primary greenhouse gas emitted through mostly burning of fossil fuels like oil and coal and altering the carbon cycle (Figure 2).[3, 5] This increase has become a great threat to the environment, including events such as species extinction, extreme weather, ocean acidification, all of which leads to a considerable problem; global warming.[6, 7] It is necessary to reduce the CO_2 concentration accumulated within the atmosphere to mitigate these problems.

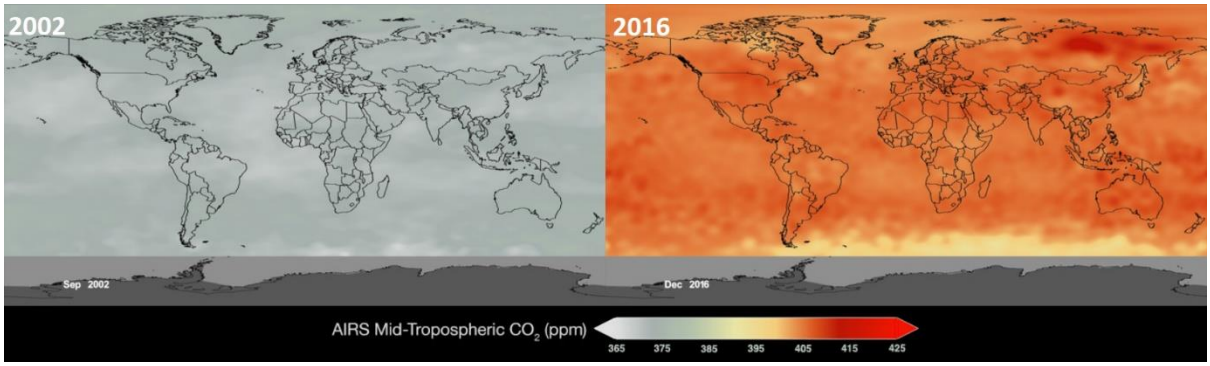

Figure 2 The change in atmospheric concentration of CO_2 from 2002 to 2016. Reproduced from reference [8]

In 2015, 193 Parties (192 countries plus the European Union) have joined the Paris Agreement to prevent climate change by committing to reducing the net GHG emissions to zero. The goal is to keep the global temperature rise below 2 °C relative to pre-industrial levels, and by pursuing efforts with limiting the increase even further to 1.5 °C.[9, 10]

At this stage, owing to their high CO_2 uptake capability, high chemical and thermal stability, and easy preparation, porous materials have become a promising option for CO_2 capture and conversion.[11, 12] As a class of porous material that will be discussed in this study, conjugated microporous polymers (CMPs) are unique amorphous porous organic polymers (POPs), which comprise extended π-conjugated skeletons that possess 3-dimensional (3D) networks.[13] CMPs are up-and-coming adsorbents for CO_2 because of their high surface area and tunable pore size.[14, 15] In recent research, it has been substantiated that CO_2 adsorption capability can be improved by incorporating electron-rich heteroatoms (such as nitrogen and sulphur) in their porous skeletons.[16, 17] The lone pair of electrons found on the heteroatoms, which provides high electronegativity, increases the interaction between the adsorbate and adsorbent.[11, 14, 18, 19]

The Faul group has recently shown that fine control over surface area, porosity and function could be possible by adjusting the Hansen Solubility Parameters (HSPs) of solvents in the synthesis of CMPs in their Bristol–Xi'an Jiaotong (BXJ) approach.[14] Thus, finding an optimal solvent could narrow the pore size distribution to micropores and enlarge the surface area of the materials.[14]

In this chapter, on account of explaining the background of this research, literature review will be presented in 5 main topics 1) porous materials, by mainly focusing on CMPs, 2) calculation of HSPs to have control over surface area, porosity and function, 3) gas adsorption process in porous materials, 4) electrochemical reduction of CO_2 and 5) the principles of the characterization methods for the materials synthesized in this study.

1.1. Porous Materials

Porous materials are mostly known as solid adsorbents that are pointed out as useful products that play important roles in many fields of science.[20] They gained interest owing to their ability to interact with molecules, ions and atoms on all their surfaces (internal and external).[21] Owing to their chemical structures and various properties, they can be used in a variety of research fields; such as catalysis,[22, 23] gas adsorption and storage,[24, 25] chemical separation processes,[26-28] electrodes,[29] and energy storage.[30, 31]

In adherence to the International Union of Pure and Applied Chemistry (IUPAC), the classification of porous materials based on their pore size (i.e., the interval between the sides of a pore), is based on their diameter (d), and divided into three classes: macroporous ($d > 50$ nm), mesoporous (2 nm $< d < 50$ nm), and microporous ($d < 2$ nm). Micropores are also classified into two classes: ultramicropores (small micropores, with pore widths smaller than 0.7 nm), and supermicropores (large micropores, with pore widths smaller than 2 nm but larger than 0.7 nm)[32] as shown in Figure 3. This classification is mainly based on different mechanisms that occur in the pores throughout isothermal N_2 adsorption at ≤1 atm pressure and 77 K.

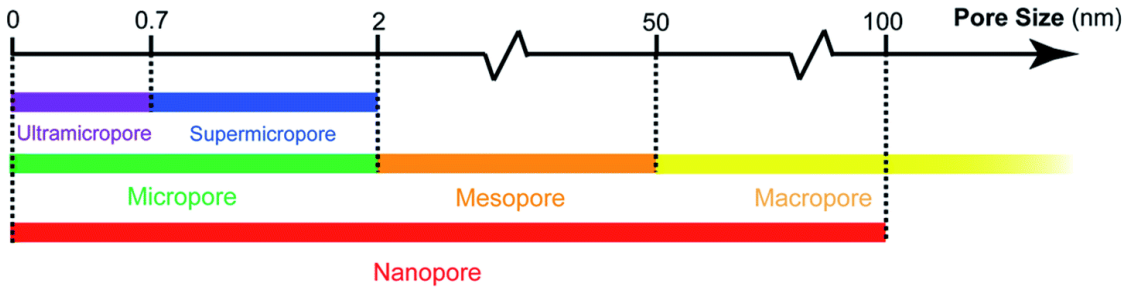

Figure 3 IUPAC classifications of pores based on pore width. Reproduced from reference [33]

The appeal of porous materials is not only owing to their extraordinary chemical and physical properties, such as chemical stability and thermal conductivity, but also their extensive presence in daily life such as bones, sponges and wood.[34] Although they can be found in nature, as a result of much research they have been developed for use in many functional and structural applications for the benefit of humankind.

According to the building blocks found in their structure, porous materials can be classified in three main categories: organic [i.e., Porous Organic Polymers (POPs)], hybrid [i.e., Metal–Organic Frameworks (MOFs)] and inorganic porous materials (i.e., zeolites, porous silicas) as shown in Scheme 1.

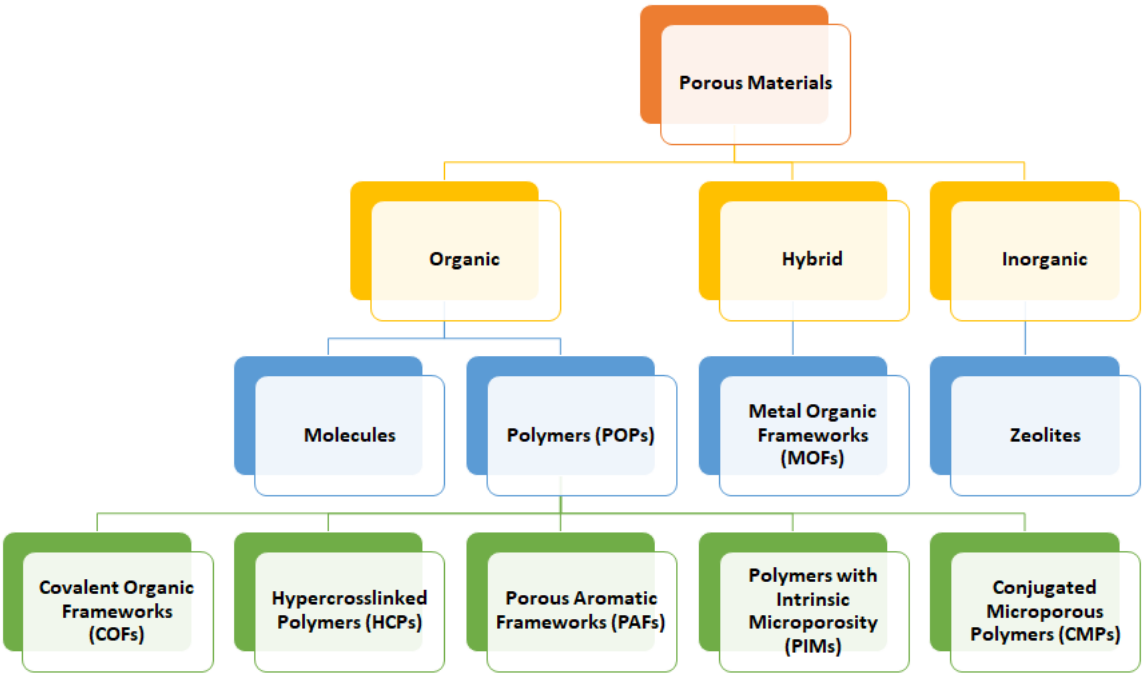

Scheme 1 Classification of porous materials according to the nature of the material. Reproduced from reference [35]

POPs, which form a novel class of porous material, are formed by covalent bonds and can be composed of building blocks that include lightweight elements such as hydrogen, carbon, nitrogen and oxygen.[36] By using numerous different sources of building blocks, the following different types of POPs can be developed: covalent organic frameworks (COFs), hyper-crosslinked polymers (HCPs), porous aromatic framework (PAFs), polymers of intrinsic microporosity (PIMs), and conjugated microporous polymers (CMPs). Among all these porous materials, CMPs have stood out owing to a variety of synthesis routes and a diversity

of building blocks, allowing for control over their structure and functionality.[13] This project is mainly focused on CMPs. Therefore, CMPs, their properties and applications, and their synthetic routes will be discussed in detail in the following section.

1.2. Conjugated Microporous Polymers (CMPs)

1.2.1. Properties of CMPs

Conjugated microporous polymers (CMPs) have received significant attention because of their properties, potential and applications since a range of conjugated microporous poly-(arylene ethynylene) networks were synthesized by Cooper et al. with Sonogashira–Hagihara coupling in 2007.[37] CMPs are π-conjugated amorphous substances that do not have a specific molecular order, which possess 3D structure. The π-conjugation, i.e., alternating single and multiple bonds, in the structure endows advantageous properties to the CMP networks, such as gas adsorption and electrochemical redox activity.[20, 38] The wide range of building blocks that can be used in the coupling allows control over the structure and functionality of CMPs. There has thus been an expanding focus on these materials owing to this structural diversity since their discovery.[37, 39, 40] CMPs have been studied in many application fields such as adsorbents (gas, dyes, solvents and other chemicals), energy storage, heterogeneous catalysis, light-harvesting materials, and photocatalysis.[20, 41-45]

CMPs not only possess low density along with high surface area, but it has been shown that they are favourable adsorbents for CO_2.[46, 47] There is a variety of conceivable approaches that could be utilised with the aim of enhancing the CO_2 uptake capability of CMPs. As an example, a widely used strategic method towards the improvement of CO_2 capture is that the framework could be decorated with particular functional groups, in particular nitrogen.[48] CO_2 uptake could be enhanced owing to the fact that nitrogen would act as a Lewis base, with CO_2 acting as a Lewis acid.

1.2.2. Synthesis of CMPs

For a CMP network to form, a reaction through building blocks should contain at least three reactive groups to ensure cross-linked network. One of the major advantages to synthesise

a 3D-structured CMP, which is mainly based on coupling reactions, is the plethora of available methods. For the synthesis of CMPs, the reactions most commonly used are: Suzuki–Miyaura,[40, 49, 50] Sonogashira–Hagihara,[51-53] Yamamoto coupling,[54, 55] Schiff-base reaction,[56-58] oxidative coupling polymerisation,[59, 60] and Buchwald–Hartwig cross-coupling.[13, 14, 61] Diverse synthesis conditions not only allow the use of a variety of functionalised monomers, moreover it provides suitable reaction conditions to whichever functional group that is intended to be added to the network.[62]

In the general route used for synthesis, the starting materials and catalyst are stirred in a convenient solvent for a certain period of time at an adequate temperature. The reaction is performed under an inert atmosphere to ensure that air does not react with the air-sensitive materials and result in changing the properties of the final compound. The precipitated product is then washed by solvents to remove the starting materials or by-products that may occur, followed by drying under vacuum to remove the solvent molecules that may have penetrated the pores.[20]

The Buchwald-Hartwig (BH) cross-coupling reaction is an extensively used Pd-catalysed synthesis method used for the formation of C(sp^2)-N bonds between amines and aryl halides, resulting in the synthesis of CMPs. The harsh reaction environments in the synthesis of aryl amines have been replaced with the emergence of the BH-coupling reactions.[61, 63]

The BH-coupling catalytic cycle is shown in Figure 4. In Step 1, the palladium(II) catalyst is reduced to a catalytically active palladium(0) complex through the oxidation of a ligand in order to easily lose a ligand in the catalytic cycle.[64] The catalytic cycle then starts with the oxidative addition of aryl halides to Pd(0) seen in Step 2. Then the amine and palladium forms a coordination by the addition of an amine, seen in Step 3. This allows the next step, deprotonation, to be easier as it increases the acidity of the proton. Afterwards, in Step 4, a palladium amide complex is formed by a strong base abstracting a proton from an amine and the halide is separated from the palladium. Lastly in Step 5), an aryl amine (the final product) is formed by reductive elimination, which can be considered the reverse of the oxidative addition step, and the catalyst is regenerated.[65-67]

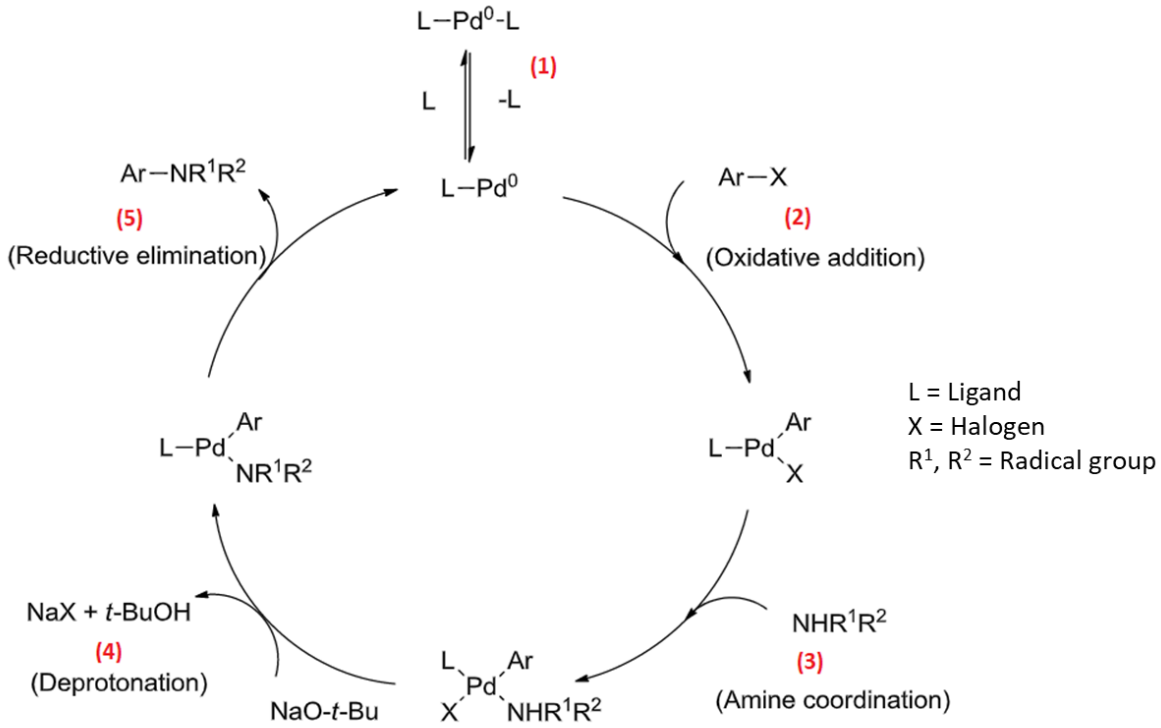

Figure 4 The catalytic cycle for Buchwald-Hartwig amination. Reproduced from reference [63]

1.2.3. Incorporation of Metal Binding Sites into CMPs

Incorporating metal binding sites in CMPs has recently drawn interest as this approach could unlock a pathway into the next generation of porous materials. As a result, a beneficial combination of physical and chemical properties, namely improved gas uptake properties, electrical conductivity and catalytic activity can be reached.[54, 68, 69] Differently from MOFs,[70, 71] metal-containing conjugated polymers are amorphous. This amorphous character allows the metal sites to be vacant and able to gain chemically activated properties.[69]

Methods that have been developed for the synthesis of metal-containing conjugated microporous polymer could be separated into two main groups: (i) first by directly doping the metal–containing co-monomer during the cross-coupling reaction, where a one-step synthesis; (ii) and, secondly by post-synthesis functionalization of CMPs with an appropriate metal species.[72-75]

1.3. Hansen Solubility Parameters (HSPs)

Choosing a solvent is an important part in the process of designing a reaction. For this particular reason, in 1967 Hansen et al. developed the Hansen Solubility Parameters (HSPs) towards understanding the solubility of a polymer in a solvent or a blend of solvents.[76, 77] Hansen proposed this model to predict the solubility of a material in a solvent. HSPs aim to quantitatively compare the compatibility of a solvent for a polymer for the purpose of designating an optimal solvent when the synthesis routes are being designed.[76]

The total cohesion energy (E) can be calculated by breaking (by evaporating) all the cohesive bonds that hold the molecules together, which is the reason that E is considered as the energy of vaporization. The underlying precept of the HSPs is assumed that the total cohesion energy comprises of three constituents that arises from dispersion, molecular and electron exchange. These interactions are, respectively: non-polar interactions, also known as dispersive forces (E_d), polar forces (E_p), which are caused by permanent dipole permanent dipole interactions, and hydrogen-bonding forces (E_h).[78]

$$E = E_d + E_p + E_h \quad (1)$$

This presupposition leads to the total Hansen parameter value of a polymer and a solvent shown in the equation below, where the subscripts, D, P, H and T mean dispersion, permanent dipole-dipole, hydrogen bonding and total interactions, respectively.

$$\delta_T = \sqrt{\delta_d^2 + \delta_p^2 + \delta_h^2} \quad (2)$$

With the intention of calculating the HSPs of a polymer, both experimental and theoretical processes can be utilised. The difference between a solvent (or solvents) respective solubility parameters and a polymer's HSPs, the resistance of a polymer against the solvent could be calculated.[79]

It is feasible to optimise the synthesis with the knowledge regarding the compatibility of solvent and polymer HSPs, aiming to enhance the yield and porosity properties. This application of HSPs enables an efficient and effective selection of suitable solvent with

particular properties in the synthesis of the polymer by controlling the interactions between the polymer and the solvent.[80]

1.4. Gas Sorption

Gas sorption is an important and comprehensive characterization technique to determine the surface area, pore size, and pore size distribution of a porous material. It is essential in order to specify, regulate and optimise materials performance.[81]

Surface area is interconnected with diverse parameters such as accessible pores, surface roughness, existence of crevices, and particle size. The porous properties of a substance could additionally influence a materials performance, including the shape, volume and size. The surface of a material is a dividing line of two separate phases which can interconnect with each other. For microporous materials, the interaction takes place between the gas molecules and the surface and could be formed by physisorption or chemisorption.[82-84]

Chemisorption occurs where gas molecules expand their ligand sphere and form a chemical bond between them and the surface of the material. Thus, these interactions result in strong bonds, which are generally irreversible and requires high adsorption enthalpies (100 to 1000 kJ mol^{-1}). In contrast, physisorption requires lower adsorption enthalpies (1–10 kJ mol^{-1}), is reversible and does not possess chemical bonds between adsorbate and adsorbent. In this case, only intermolecular forces are involved (e.g., Van Der Waals force, dipole-dipole interactions, hydrogen bonding).[32, 84, 85] The illustration of the difference between these two interactions are shown in Figure 5.

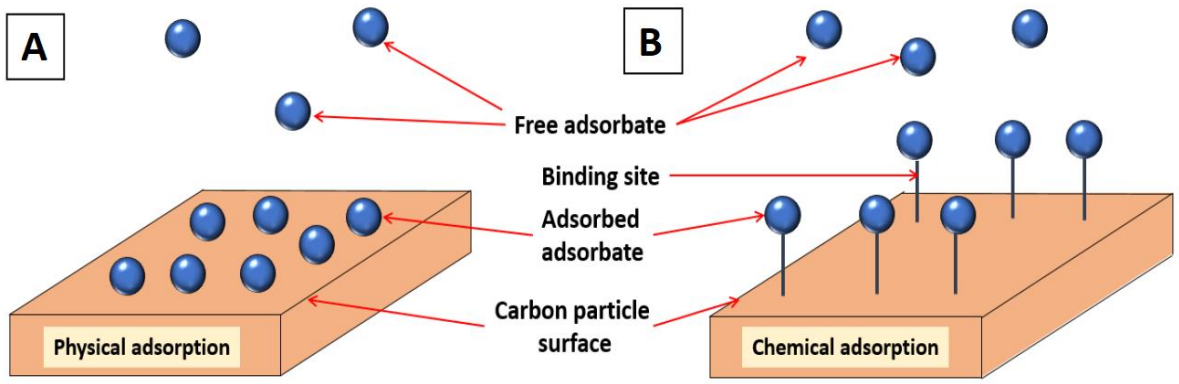

Figure 5 Illustration of the mechanisms in physisorption **(A)** and chemisorption **(B)** interactions. Reproduced from reference [86]

With the aim of characterising majority of porous materials, the procedure that is used in general and is most functional is nitrogen sorption analysis performed at 77 K.[32, 87]

1.4.1. BET Surface Area Determination

Irving Langmuir introduced a model known as the Langmuir isotherm in 1916 in regard to the adsorption of molecules on a material's surface,[88] where several presuppositions are made: a) the number of sites on a surface of a material is constant, b) the adsorption on all positions are equivalent, c) there is a dynamic balance between the free and adsorbed gaseous molecules, and d) the adsorption only occurs as a monolayer.

After further research done by Brunauer, Emmett and Teller in 1938, alterations were made where a novel model, the BET isotherm was presented.[89] Contrary to the Langmuir model, it is assumed that adsorption occurs as a multilayer. Thus, except those on the first layer, not all gas molecules have a direct connection with the surface. Accordingly, between the gaseous molecules, vapor-phase interactions are to be seen.[90, 91]

Not only the surface area is the predominant aspect in the adsorbent, the interaction between the solid and gas, the pressure of the gas and the temperature is likewise crucial. Owing to its powerful interplay between solid materials, nitrogen is generally used in BET analysis to determine the surface area. In order to strengthen the interplay between gas and solid and to detect the amount adsorbed, the measurement is carried out at nitrogen's boiling point (77K), where the gas particles could condense on the surface below its critical temperature. The polymer is loaded into a sample holder and a known volume of nitrogen gas is then slowly added to the system, and while the measurement is undertaken the pressure of the gas is increased. The collected information is then plotted as the relative pressure against the amount of gas adsorbed, which is monitored as a sorption isotherm and analysed with the BET model.[92, 93]

The surface area of a material can be evaluated by having the information about the amount and area filled in the presence of one gas molecule and with the knowledge of the quantity of the solid adsorbent. The BET surface area determination method helps to calculate the total surface area of materials with a range of 0.01 to 6000 m^2/g. Besides the

surface area of a material, the pore size and pore size distribution can also be determined by using the isotherm.

The most crucial factor in relation to accurately measuring the surface area, pore size and pore size distribution is that all contamination from the sample, which may belong to solvents and gas molecules that could have been trapped, should be removed before the measurement with a degassing process. The process is usually performed by exposing the sample to high temperature while under vacuum.

1.4.2. Physisorption Isotherms

A sorption isotherm is defined as the total adsorption/desorption process, where the quantitative association among the quantity of gas adsorbed on an adsorbent is recorded in response to a change in pressure at a constant temperature.[94] As attested by IUPAC, physisorption isotherms are primarily assigned to six types according to the characteristics of the adsorbents.[32, 87, 95, 96] The physisorption isotherm classifications are shown in Figure 6.

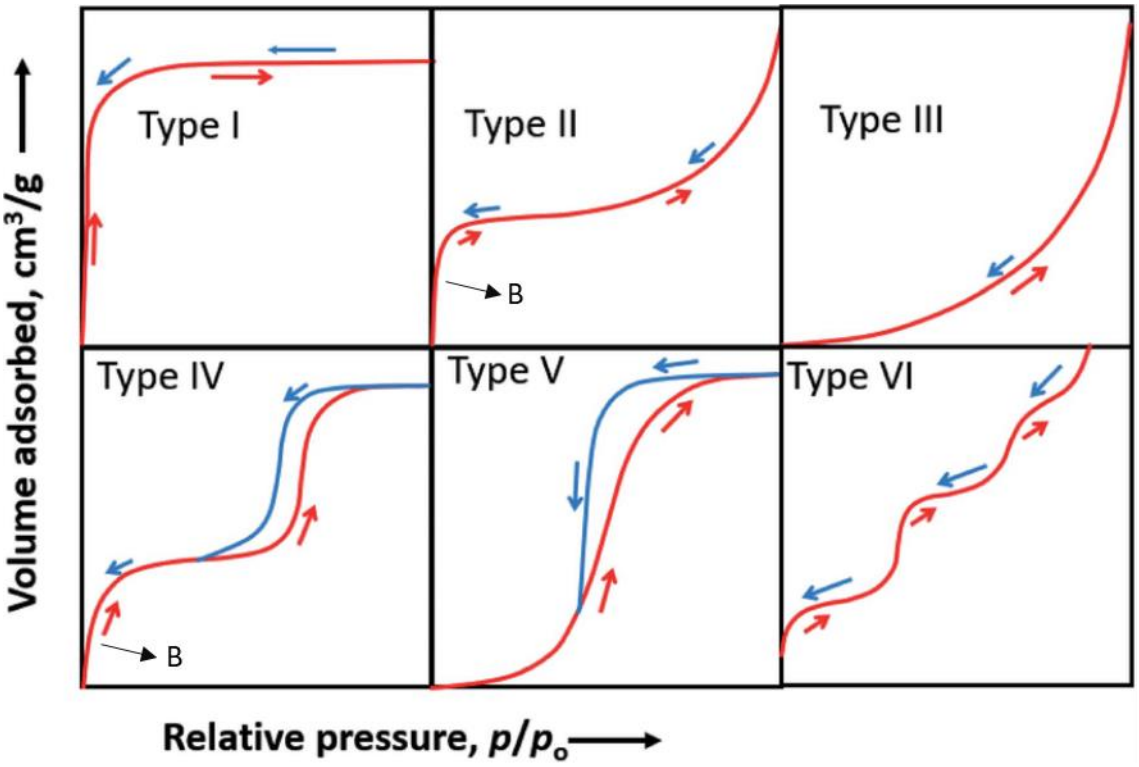

Figure 6 IUPAC classification of physisorption isotherms. Reproduced from reference [97]

A Type I isotherm is obtained by microporous materials where sorption occurs as monolayer only, which normally result with high uptake even at low pressure. Additionally, a Type II isotherm is found owing to monolayer-multilayer physisorption of gas molecules onto microporous or nonporous adsorbents, where point B (the starting point of the linear part, see Figure 6 II) in general is correlated with the fulfilment of monolayer capacity. A Type III isotherm is also obtained by microporous or nonporous materials, but different from a Type II isotherm with no point B observed. This behaviour means that the interaction between the solid material and adsorbed gas is weak, and monolayer adsorption requires much more pressure.

Type IV isotherms are obtained by mesoporous materials and exhibit a hysteresis loop. The hysteresis loops are related to capillary condensation that takes place when the pore width exceeds a certain critical width. Owing to monolayer adsorption, these materials show similarity at low pressure with Type II isotherms, where the adsorption then increases on account of capillary condensation. Type V isotherms also exhibit a hysteresis loop and indicate similarity to that of Type III at the low p/p^0 range, which is interpreted that the adsorbate and adsorbent interactions are comparatively weak. Lastly, Type VI isotherms are obtained by materials that are nonporous and have a smooth surface with multilayer adsorption.[32, 87]

1.5. Electrochemical Reduction of CO_2

One of the most sustainable methods to resolve the biggest environmental concerns is the reduction of CO_2 to other useful and valuable chemicals. From a variety of options, biochemical conversion, photo-catalytic reduction and electrochemical reduction are some of the most well-known and used CO_2 reduction methods.[98] Among these methods, conversion of CO_2 to useful materials by electrochemical reduction have been prominent as very advantageous. As can be seen in Figure 7, CO_2 could be converted to valuable products such as carbon monoxide (CO), formic acid (HCOOH) and methanol (CH_3OH).[99-101] Table 2 shows some of the half-reactions, and their potentials against the standard hydrogen electrode (SHE) at pH 7.

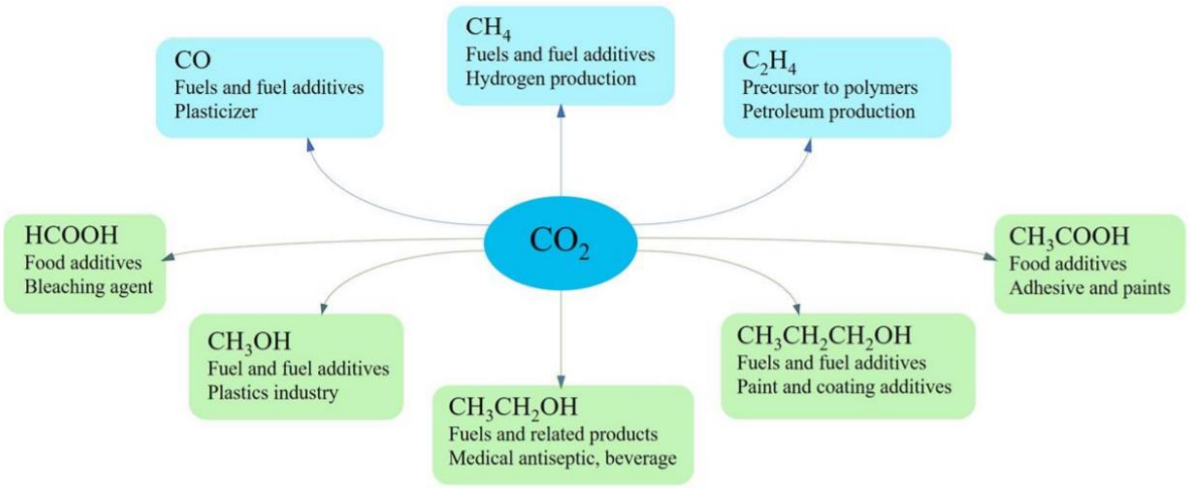

Figure 7 Electrochemical CO_2 reduction to other products and their application. Reproduced from reference[102]

Table 2 Electrochemical potentials of possible CO_2 reduction reactions in aqueous solutions. Reproduced from reference[103]

ECO_2R Reactions	**Potential vs SHE pH = 7 (V)**
CO_2 (g) + $2H^+$ + $2e^-$ → HCOOH (l)	-0.61
CO_2 (g) + $6H^+$ + $6e^-$ → CH_3OH (l) + H_2O (l)	-0.38
CO_2 (g) + $2H^+$ + $2e^-$ → CO (g) + H_2O (l)	-0.53
CO_2 (g) + $6H_2O$ (l) + $8e^-$ → CH_4 (g) + $8OH^-$	-0.25
$2CO_2$ (g) + $12H^+$ + $12e^-$ → C_2H_4 (g) + $4H_2O$ (l)	0.06
$2CO_2$ (g) + $12H^+$ + $12e^-$ → CH_3CH2OH (l) + $3H_2O$ (l)	0.08
CO_2 (g) + $5H_2O$ (l) + $6e^-$ → CH_3OH (l) + 6OH	-0.81

In the route towards initiating the CO_2 electrochemical reduction (CO_2ECR) process, the catalyst is deposited onto a conductive support such as carbon paper, glassy carbon or metal foils and bound using an ion-conducting binder as shown in Figure 8.[104] Subsequently, the electrode is then put into an electrolytic cell that contains an electrolyte to conduct an electrical current. A certain amount of potential is then applied to the system, where the CO_2 bonds are broken down by the electrons and protons.[105]

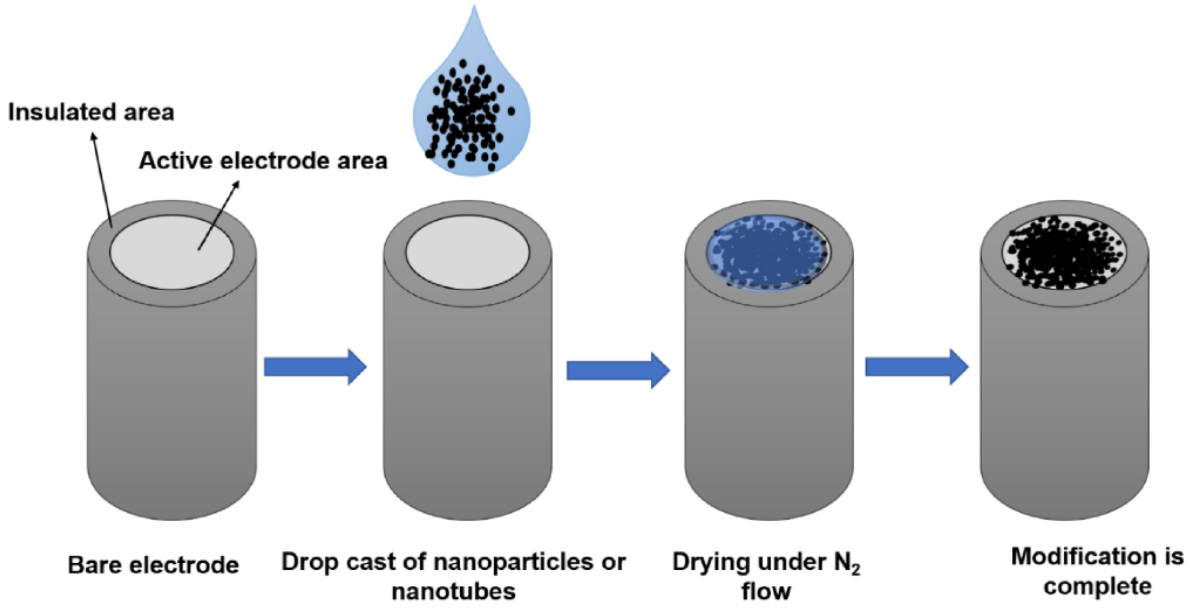

Figure 8 A schematic showing the coating of the active area of an electrode. Reproduced from reference[106]

The CO_2ECR process has many advantages. Firstly, as can be seen in Table 2, with adjusting the potential it is very simple to control the reaction. Also, the electrolyte could be recovered in order to be reused. Another advantage is that the system could be easily scaled up owing to the electrochemical setup being modular and compact. One of the biggest benefits is that the required electricity could be acquired from renewable resources.

As they have control over the stability, selectivity and activity, the properties of the catalytic materials are very important in CO_2ECR. Among others, metallic catalysts, for instance metal oxides, bimetallic systems and nanoparticles are well known for their advantageous features. These features include the production of a comprehensive range of products, which are low in price, and exhibit good stability, and large surface areas.[107] Furthermore, the number of active sites could be further increased owing to existence of metals/transition metals in their framework. For example, in the presence of Cu metal, an extensive variety of hydrocarbons could be produced; meanwhile Co and Pd produced formic acid and carbon monoxide (CO); Pt produced methanol (CH_3OH) and CO; Sn produced formic acid (HCOOH); and Zn, Au and Ag produced CO.[108]

1.6. Characterisation of CMPs

To understand the properties and functions of CMPs, it is essential to use several characterization methods. The methods applied in this research include X-ray diffraction (XRD), Fourier-transform infrared spectroscopy (FT-IR), ultraviolet–visible-near infrared spectroscopy (UV-Vis-NIR), scanning electron microscopy (SEM) and energy dispersive X-ray (EDX). FTIR and UV-Vis-NIR are used for component characterization, whilst XRD, SEM and EDX are aimed at assessing the morphology of the products.

1.6.1. X-ray Diffraction (XRD)

X-ray diffraction (XRD) is a useful analytical technique for the determination of a material's crystallographic structure. The working principle of XRD is based on exposing samples to X-rays where they are diffracted at an angle, which reveals characteristic patterns belonging to the structure. Some waves are scattered by the atoms on the surface of the material, while some pass through owing to the angle of diffraction being equal to the angle of incidence, and scatter from the next layers. This scattering results in a diffraction pattern, much like a light beam being refracted by a grating. A representation of the diffraction of X-rays can be seen in Figure 9.[109-111]

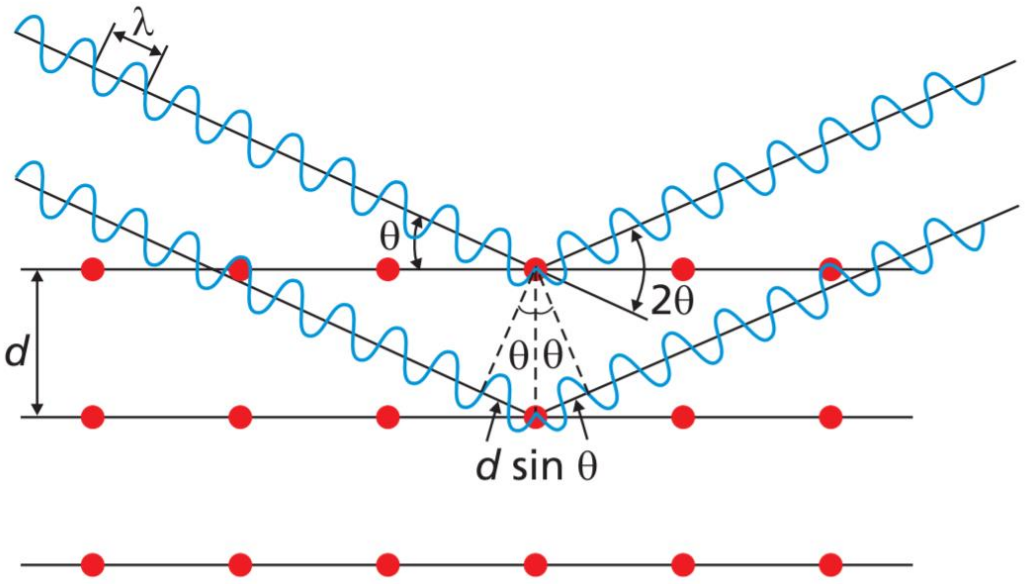

Figure 9 Schematic representation of Bragg's law of diffraction. Reproduced from reference[112]

In 1913, Bragg's law was developed by W.H. Bragg and his son William Lawrence Bragg by presenting the equation below that gives the relationship between the angles of incidence and the spacing of atomic planes in crystals.[113]

$$n\lambda = 2d \cdot \sin\theta \quad (3)$$

where d is the distance between two atomic layers, λ is the wavelength of X-rays, and n is an integer.

To study the X-ray diffraction properties of a sample, there are several methods, where powder X-ray diffraction (PXRD) is the most commonly used with porous materials. In this technique, the materials are first ground into a powder before carrying out the analysis. On account of the sample being a powder, and therefore not a single crystal, it is usually considered a very convenient method.[114]

The materials synthesised in this study are amorphous and do not have a definite regular arrangement. Owing to the fact that amorphous carbons do not diffract X-rays at a particular single angle, the XRD diffractograms are expected to show broad diffraction peaks.[115]

1.6.2. Fourier-Transform Infrared (FT-IR) Spectroscopy

Fourier-transform infrared (FTIR) spectroscopy is a technique that is used to acquire infrared spectra of gas, liquid and solids. The particular molecular groups present in the sample are responsible for the absorption of radiation at different frequencies, and will be specified in the spectrum data. The infrared absorption frequency range is from 10 – 10000 cm^{-1}: near (NIR, ν=10000 – 4000 cm^{-1}); middle (MIR, ν=4000 – 200 cm^{-1}), and far (FIR, ν=200 – 10 cm^{-1}).[116]

FTIR spectroscopy is an extensively developed analytical device in science used to differentiate the functional groups found in materials. The main idea of this method is to measure the vibrational transitions between the molecules and the wavelength of the absorbed energy with the use of an IR spectrometer. The detector then transfers the results to a graph where the wavenumber (cm^{-1}) on the X-axis is shown against the corresponding vibration energy of the molecular bonds on the Y-axis as percentage transmittance (%T).

A characteristic absorption occur at certain wavenumbers that correspond to particular vibrations, which can be used to identify and distinguish the specific chemical bonds found in a material. Owing to the fact that every material having its own characteristic fingerprint, FTIR has become an invaluable characterization method.[117-119]

1.6.3. Ultraviolet-Visible-Near Infrared (UV-Vis-NIR) Spectroscopy

Ultraviolet-visible-near infrared (UV-Vis-NIR) spectroscopy is a quantitative analytical technique that provides information about a molecule's electronic and vibrational transitions. This technique is convenient for materials that contain conjugation, alternating single and double bonds, in particular. The instrument measures the amount of light a material absorbs, transmits, or reflects at each wavelength. To accomplish this measurement, the procedure is carried out by measuring the light intensity that passes through the material being analysed. The optical absorption spectra in UV-Vis-NIR spectroscopy is between 200 and 800 nm (UV: 200 to 400 nm, and Vis: 400 to 800 nm), and could exceed to 1400 nm in the near-infrared (NIR) region.[120-122]

The formation of π-bonds occurs by the half-filled p orbitals on two atoms overlapping sideways. Molecules containing conjugated systems would cause their electrons to be delocalized because of the p orbitals overlapping while forming a π-bond. The energy gap between the π orbital and the π-star orbital decreases as the number of delocalization in a substance increase. Consequently, a bathochromic (to longer wavelength) shift in the wavelength of the light absorbed occurs.

In UV-Vis-NIR spectroscopy, the amount of light that passes through a material, which is called transmittance, is measured. The absorbance can then be calculated from the transmittance (T) with the equation below:

$$\mathrm{A} = -\log 10(\mathrm{T}) \tag{4}$$

As shown by the Beer-Lambert Law, there is a linear proportion among the absorbance and the concentration of the material found as a solution. This enables to calculate the concentration of the sample by measuring its absorbance in UV-Vis-NIR spectroscopy

The Beer-Lambert law is written as in the form equation below:

$$A = \varepsilon cd \quad (5)$$

As given in the equation; A is the absorbance, c is the solution concentration (M), d is the optical path length the light passes through (cm), and ε is the molar absorptivity or the molar absorption coefficient of the substance analysed ($M^{-1}cm^{-1}$).[123, 124]

Substances that contain atoms with non-bonding orbitals or π-bonds absorb light in the UV and Vis region, while transition-metal ions and most highly π conjugated systems, owing to having many electrons in their structure, absorb light in the NIR region.[125]

1.6.4. Scanning Electron Microscopy (SEM)

Scanning electron microscopy (SEM) is a useful investigative method where the surface of a solid material is imaged by high magnification with a focused beam of electrons. The surface of the sample is first coated with a conductive substance, usually carbon or gold, which is then scanned with a beam of high energy electrons. The image of the surface is then acquired by the detector of the electron microscope from the scattered electrons on the samples surface.[126]

SEM is a useful method to get information about the morphology and topography of a material. It is possible to obtain information about the presence of pores, texture of the surface, and size and shape of particles of the material that is being analysed. Advanced version of SEM instruments can achieve a resolution of 1 micrometer (µm).[126-128] Therefore, only a connection between the morphology and texture of the surface could be drawn rather then the porosity of the CMPs being investigated in this study.

1.6.5. Energy-Dispersive X-ray Spectroscopy (EDX)

Energy-dispersive X-ray spectroscopy (EDX) microanalysis is an analytical method used to identify a samples composition of elements, which is used conjointly with SEM. The technique is based on bombarding a sample with a high-energy electron beam to detect the characteristic X-rays generated. By focussing a beam on the sample, an electron is excited from its ground state, which causes it to eject and form a hole in the electronic structure of the element. Thereafter, an electron from a higher energy fills in this electron vacancy

where it will release energy as it relaxes (the difference between two energy levels), which is then detected by a spectrometer. The elemental composition of materials could be determined owing to the fact that each element displays a characteristic X-ray energy. The data obtained consists of a spectrum that shows peaks that correspond to the elements that are included in the composition of the sample analysed.[126, 129]

1.7. Aim and Objectives

The overall aim of this study is to synthesise novel nitrogen-rich CMPs to ensure that there are sites within the porous structure suitable for CO_2 capture and conversion applications. In order to achieve this aim, the following objectives have been identified:

- Synthesise CMPs with bipyridine and terpyridine derivatives based on tris(4-bromophenyl)amine (TBPA) and p-phenylenediamine (PPDA).
- Calculation of HSPs and choice of optimal solvent to increase the yield and total surface area.
- Study the materials' CO_2 adsorption capability (by determining their surface area and porosity using the BET method), and redox processes (by cyclic voltammetry).
- Exploration of options to bind various metal ions to the CMPs and study their activity for CO_2 capture and redox processes.

2. Methodology

In this section, the experimental part of this study, the chemicals and the instrumentation used are presented. Firstly, the general synthesis method of the CMPs will be described. Afterwards, solubility tests for HSP studies to optimise for yield and surface area will be introduced, along with the synthesis with solvents found by the calculation of HSPs. Finally, the synthesis of metal-containing CMPs will be described for the further investigations.

2.1. Synthesis Procedures

The CMPs in this study were synthesized using the Buchwald-Hartwig cross-coupling reaction. In the first part of the research, different core-to-co-monomer ratios were used to find the optimal reaction conditions and ascertain the effect of the amount of co-monomers used. In the second part, different solvents were used (from calculating the HSPs) to achieve high yields and high surface areas.

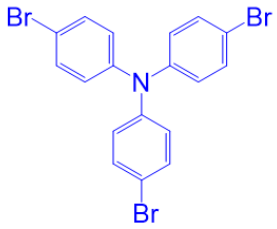

tris(4-bromophenyl)amine
(TBPA)

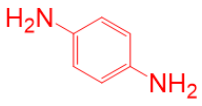

p-phenylenediamine
(PPDA)

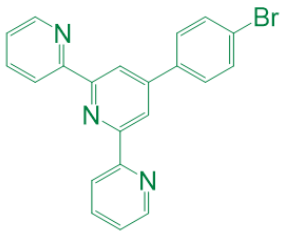

4'-(4-bromophenyl)-2,2':6',2''-terpyridine
(TP)

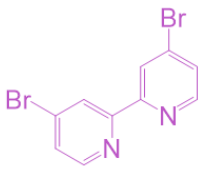

4,4'-dibromo-2,2'-bipyridine
(BP)

Figure 10 Chemical structures of monomers (TBPA, PPDA, TP and BP) used in this study

Starting materials were tris(4-bromophenyl)amine (TBPA) and p-phenylenediamine (PPDA). Two different pyridine derivatives were used in the formation of the 3D porous network as

co-monomer and extension units to explore the influence of active sites within the porous framework; 4'-(4-bromophenyl)-2,2':6',2''-terpyridine (TP) and 4,4'-dibromo-2,2'-bipyridine (BP). The chemical structures of all used starting materials are given in Figure 10.

In the first part of the research, syntheses were performed varying the relative molar ratios of TBPA:pyridine derivatives whilst keeping a constant 1.5 molar ratio of PPDA, as presented in Table 3. More detailed information regarding these parameters is presented in the following sections.

Table 3 Molar ratios of the monomers used in the synthesis

Name	Molar Ratios			
	TP	BP	TBPA	PPDA
CMP-TP-1	0.1	-	0.9	1.5
CMP-TP-2	0.2	-	0.8	1.5
CMP-TP-3	0.3	-	0.7	1.5
CMP-TP-4	0.4	-	0.6	1.5
CMP-BP-1	-	0.1	0.9	1.5
CMP-BP-2	-	0.2	0.8	1.5
CMP-BP-3	-	0.3	0.7	1.5
CMP-BP-4	-	0.4	0.6	1.5

2.1.1. Synthesis of PTPA

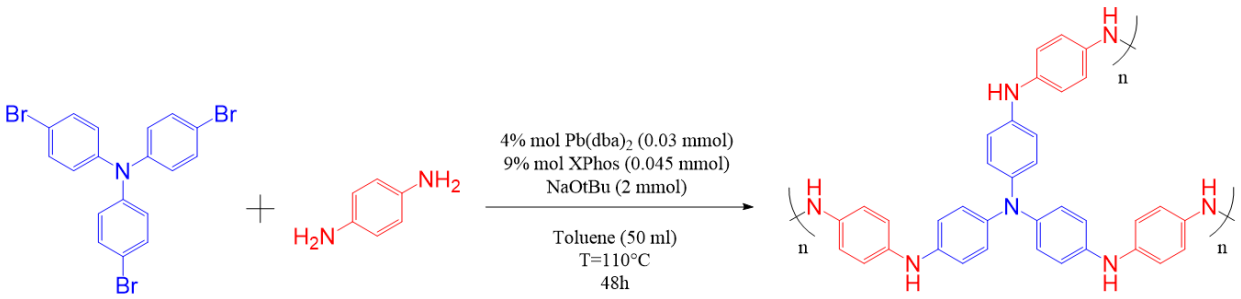

Scheme 2 Synthesis of PTPA

To compare the results of the synthesised materials, poly(triphenylamine) network (PTPA) that was reported by Faul research group in 2014 using a (1:1.5) stoichiometric ratio, was

used as control material.[61] (Scheme 2). A Schlenk tube was charged with tris(4-bromophenyl)amine (0.5 mmol, 241 mg), p-phenylenediamine (0.75 mmol, 81.1 mg), $Pd(dba)_2$ (dba=dibenzylideneacetone, 17.3 mg, 0.03 mmol) 2-dicyclohexylphosphino-2',4',6'-triisopropylbiphenyl (XPhos, 21.5 mg, 0.045 mmol), and sodium tert-butoxide (NaOtBu, 192.2 mg, 2 mmol) and placed under a nitrogen atmosphere. Anhydrous toluene (50 mL) was added, and the reaction mixture was heated under stirring to 110°C for 48 h. The reaction was cooled to room temperature and the remaining solids were washed with chloroform, hot deionized water, and methanol (200 mL each), and then dried 72 h in a vacuum oven at room temperature to obtain the corresponding dark blue product. (Yield: 68.0 %)

2.1.2. Synthesis of CMPs (CMP-TPs and CMP-BPs)

A Schlenk tube was charged with varying amounts of TP and TBPA (Table 3), p-phenylenediamine (1.5 mmol, 162.2 mg), $Pd(dba)_2$ (dba=dibenzylideneacetone, 17.3 mg, 0.03 mmol) 2-dicyclohexylphosphino-2',4',6'-triisopropylbiphenyl (XPhos, 21.5 mg, 0.045 mmol), and sodium tert-butoxide (NaOtBu, 192.2 mg, 2 mmol) and placed under a nitrogen atmosphere. Anhydrous toluene (50 mL) was added, and the reaction mixture was heated under stirring to 110°C for 48 h. The reaction was cooled to room temperature and the remaining solids were washed with chloroform, hot deionized water, and methanol (200 mL each), and then dried 72 h in a vacuum oven at room temperature to obtain the corresponding products (Scheme 3).

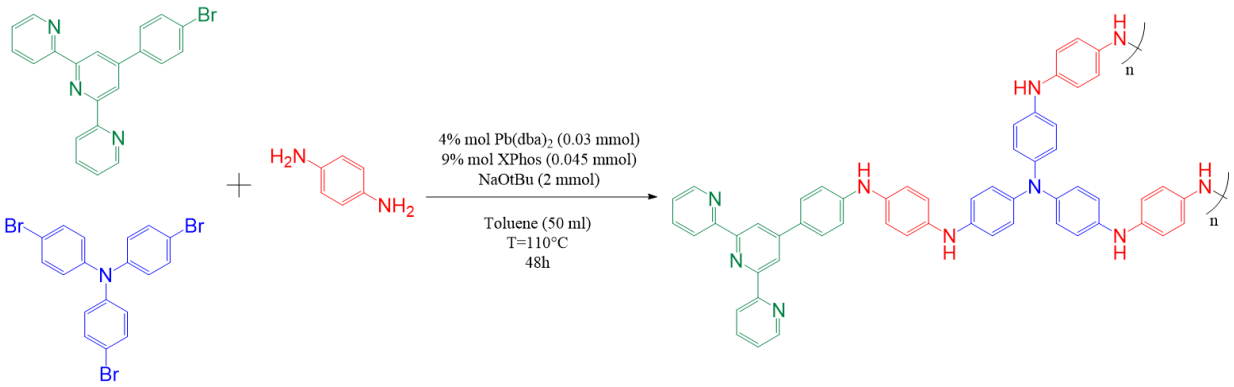

Scheme 3 Synthesis of CMP-TPs

The same reaction was also carried out by using 4,4'-dibromo-2,2'-bipyridine (Scheme 4). The yields of the samples are shown in Table 4.

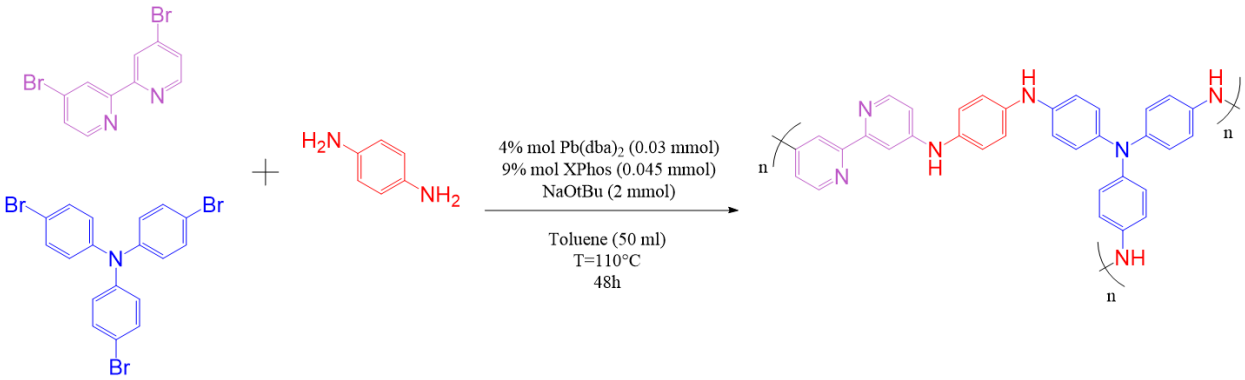

Scheme 4 Synthesis of CMP-BPs

Table 4 The amounts of co-monomers and TBPA, reaction conditions and corresponding yields in the synthesis

Name	Pyridine unit		TBPA		Conditions	Yield
	[mg]	[mmol]	[mg]	[mmol]		%
CMP-TP-1	38.8	0.1	433.8	0.9		39.5
CMP-TP-2	77.6	0.2	385.6	0.8		27.6
CMP-TP-3	116.4	0.3	337.4	0.7		25.3
CMP-TP-4	155.2	0.4	289.2	0.6	Toluene	33.5
CMP-BP-1	31.4	0.1	433.8	0.9	48h at 110 °C	48.8
CMP-BP-2	62.8	0.2	385.6	0.8		45.5
CMP-BP-3	94.2	0.3	337.4	0.7		41.2
CMP-BP-4	125.6	0.4	289.2	0.6		47.1

2.2. HSPs Study

2.2.1. HSPs Determination of CMP-TPs and CMP-BPs

Sixteen solvents (DMSO, DMF, ACN, NMP, propylene carbonate, xylene, toluene, ethanol, dioxane, chloroform, acetone, dichloromethane, ethyl acetate, hexane, THF and water) were applied in the solubility study. 2 mg of finely grounded **CMP-TP-1**, **CMP-TP-4**, **CMP-BP-**

1 and **CMP-BP-4** was added into sixteen vials each. Each vial was filled with 5 ml of one of the selected solvents. It is important to note that the amount of the polymer and solvents must be the same in all vials. The numbered vials were then put into a sonication bath for 24 hours. After sonication, the suspensions were left to settle for 1 h.

UV-Vis absorbance spectra of each polymer in the supernatant of the dispersions was recorded by UV-Vis spectrometer (UV-2600 Shimadzu), with 1 cm optical path and 5 nm slit width. The baseline (from 1400 to 220 nm) was corrected automatically by scanning the background solvent and cuvette. The absorbance intensities of each sample were recorded from 800 nm to 250 nm.

After the samples settled, the solutions were carefully pipetted from the vials and the UV-Vis absorption recorded. Before recording the UV-Vis spectrum of a new polymer+solvent pair, the baseline was corrected with the correct solvent. The absorbance observed for each sample was compared between different solvent systems. Three HSP components (δ_D, δ_P, δ_H) and total HSP (δ_T) of all the solvents were individually sorted with ascending trend. Transmission of the polymers in each solvent was plotted against the corresponding HSPs. The discrete data points were fitted by B-Spline in Origin 2018b. The maximum value from the resulting B-Spline fitting curve was considered as the corresponding HSP component of the polymer.

The maximum values from the resulting B-Spline fitting curve shows the dispersion, polar and hydrogen-bonding forces along with total solubility parameters of the polymer. δ_T of polymers were then compared with δ_T of each solvent. The difference between these δ_T values, as shown in Eq. 6, helps to understand, predict and improve the solubility, the compatibility, the stability and the efficacy between the solvent and the solute. It can be said that solvents with $\Delta\delta_T$ smaller than 1 are regarded as good, between 1-3 are intermediary, and greater than 3 are poor solvents.

$$\Delta\delta_T = \left|\delta_{T_{PTCDA}} - \delta_{T_{Solvent}}\right| \quad (6)$$

With the calculation of HSPs for 4 CMPs, DMSO, propylene carbonate and ethanol were chosen as optimal solvents for the synthesis. The result of the HSPs of the polymers along with dispersion, hydrogen bond, polar-cohesive and total HSPs measured with UV-Vis

absorbance intensity in a series of solvents can be found in the Results and Discussions section (Page 94).

2.3. Synthesis of CMPs by Results from HSPs Study

2.3.1. Synthesis of CMPs

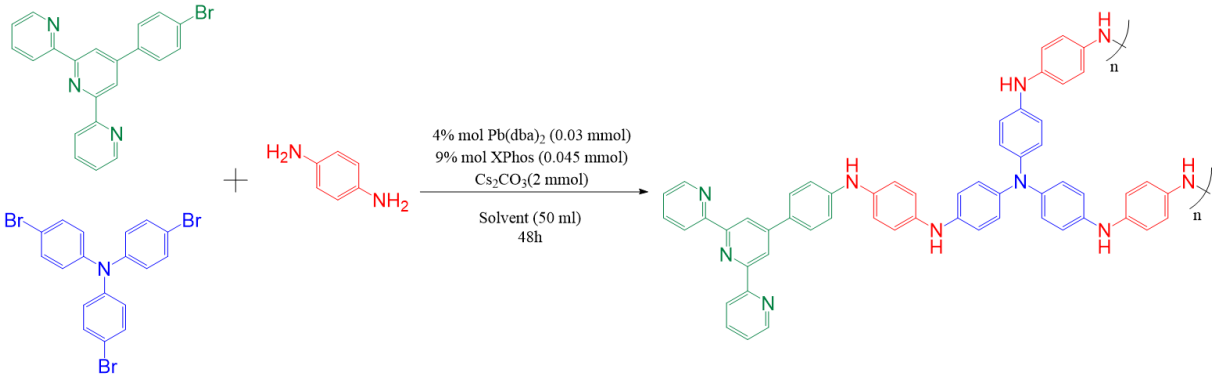

Scheme 5 Synthesis of CMP-TPs with optimal solvents

The synthesis of CMP-TPs with DMSO, propylene carbonate and ethanol, respectively, follows a similar procedure as the control reaction (Section 2.1.2., Scheme 5, page 23). A Schlenk tube was charged with varying amounts of TP and TBPA (Table 5), p-phenylenediamine (1.5 mmol, 162.2 mg), $Pd(dba)_2$ (dba=dibenzylideneacetone, 17.3 mg, 0.03 mmol) 2-dicyclohexylphosphino-2',4',6'-triisopropylbiphenyl (XPhos, 21.5 mg, 0.045 mmol), and caesium carbonate (Cs_2CO_3, 651.64 mg, 2 mmol) and placed under a nitrogen atmosphere. Solvent (DMSO, propylene carbonate and ethanol, respectively, 50 mL) was added, and the reaction mixture was heated under stirring to at suitable temperature (110°C for DMSO and propylene carbonate, and 78°C for ethanol) for 48 h. The reaction was cooled to room temperature and the remaining solids were washed with chloroform, hot deionized water, and methanol (200 mL each), and then dried 72 h in a vacuum oven at room temperature to obtain the corresponding products.

The synthesis of CMP-TPs and CMP-BPs with DMSO, propylene carbonate and ethanol were first carried out by using NaOtBu as base, however no material was observed. The base was then changed to Cs_2CO_3 which is known as a milder base. To investigate the influence of changing the base, the reaction was also carried out using toluene as solvent.

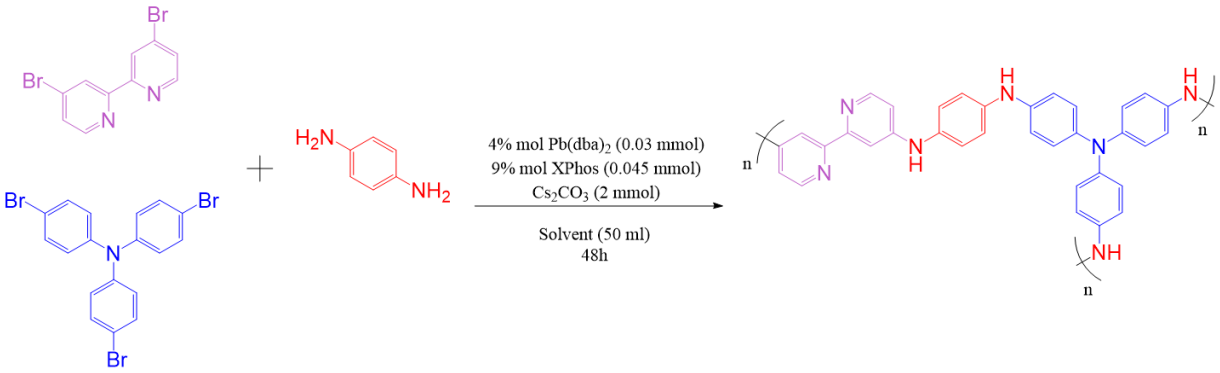

Scheme 6 Synthesis of CMP-BPs with optimal solvents

The same reaction was also carried out by using 4,4'-dibromo-2,2'-bipyridine (Scheme 6). The yields of the reactions are shown in Table 5.

Table 5 The corresponding yields of CMPs synthesised with DMSO, propylene carbonate and ethanol

Name	Pyridine unit (mmol)	Conditions	Yield (%)
CMP-TP-1-D	0.1	Solvent: DMSO	0.9
CMP-TP-4-D	0.4	48h at 110 °C	0.9
CMP-TP-1-E	0.1	Solvent: Ethanol	6.4
CMP-TP-4-E	0.4	48h at 78 °C	5.7
CMP-TP-1-1	0.1	Solvent: Propylene carbonate	19.2
CMP-TP-4-1	0.4	48h at 110 °C	39.0
CMP-TP-1-2	0.1	Solvent: Toluene	7.3
CMP-TP-4-2	0.4	48h at 78 °C	5.9
CMP-BP-1-D	0.1	Solvent: DMSO	0.5
CMP-BP-4-D	0.4	48h at 110 °C	0.5
CMP-BP-1-E	0.1	Solvent: Ethanol	6.0
CMP-BP-4-E	0.4	48h at 78 °C	4.2
CMP-BP-1-1	0.1	Solvent: Propylene carbonate	15.8
CMP-BP-4-1	0.4	48h at 110 °C	23.5
CMP-BP-1-2	0.1	Solvent: Toluene	7.0
CMP-BP-4-2	0.4	48h at 110 °C	6.4

2.3.2. Synthesis of CMPs with Higher Catalyst Loading

To further explore opportunities to enhance yields, the quantity of catalyst and ligand was increased by a factor of 10 (4% mol instead of 0.4% mol and 9% mol instead of 0.9% mol, respectively) was used in the synthesis to improve reaction conditions.

A Schlenk tube was charged with varying amounts of pyridine unit (TP or BP) and TBPA, p-phenylenediamine (1.5 mmol, 162.2 mg), Pd(dba)2 ((dba=dibenzylideneacetone) 0.30 mmol, 172.5 mg 4% mol), 2-dicyclohexylphosphino-2',4',6'-triisopropylbiphenyl (XPhos, 0.45 mmol, 214.5 mg 9% mol), and caesium carbonate (Cs_2CO_3, 651.64 mg, 2 mmol) and placed under a nitrogen atmosphere. Anhydrous solvent (toluene and propylene carbonate, respectively, 50 mL) was added, and the reaction mixture was heated under stirring to 110°C for 48 h. The reaction was cooled to room temperature and the remaining solids were washed with chloroform, hot deionized water, and methanol (200 mL each), and then dried 72 h in a vacuum oven in room temperature to obtain the corresponding products. The yields of the samples are shown in Table 6.

Table 6 The corresponding yields of CMPs synthesised with larger catalyst loading

Name	Pyridine unit mmol (mg)	Conditions	Yield %
CMP-TP-1-3	0.1	Solvent: Toluene 48h at 110 °C	39.2
CMP-TP-4-3	0.4		37.1
CMP-BP-1-3	0.1		35.9
CMP-BP-4-3	0.4		30.0
CMP-TP-1-4	0.1	Solvent: Propylene carbonate 48h at 110 °C	90.1
CMP-TP-4-4	0.4		94.2
CMP-BP-1-4	0.1		88.6
CMP-BP-4-4	0.4		89.5

2.4. Synthesis of Metal-Containing CMPs

Metal-containing CMPs were synthesised by two different methods: Route 1 is by the direct cross-coupling with a co-monomer containing metal, and Route 2 is by post-synthesis functionalised CMP with a metal.

2.4.1. Synthesis of CMPs by Direct Metal Incorporation (Route 1)

In Route 1, the syntheses were carried out by first forming a metal-containing co-monomer with the pyridine units and metal salt in an appropriate solvent. The synthesis was then continued with the Buchwald-Hartwig cross-coupling reaction by adding the remaining starting materials.

A Schlenk tube was first charged with 4'-(4-bromophenyl)-2,2':6',2''-terpyridine (0.1 mmol, 38.8 mg) and metal salt (0.1 mmol, $CuBr_2$ (22.3 mg) or $CoCl_2$ (12.9 mg)) at room temperature in propylene carbonate (50 mL) for 4 hours under a nitrogen atmosphere to form a complex to be used as a co-monomer. Afterwards, tris(4-bromophenyl)amine (0.9 mmol, 433,8 mg) as core, p-phenylenediamine (1.5 mmol, 162.2 mg, to obtain the 1:1.5 ratio of core to linker) as linker, $Pd(dba)_2$ (dba=dibenzylideneacetone, 17.3 mg, 0.03 mmol) 2-dicyclohexylphosphino-2',4',6'-triisopropylbiphenyl (XPhos, 21.5 mg, 0.045 mmol), and caesium carbonate (Cs_2CO_3, 651.64 mg, 2 mmol) is added to the solution and the reaction mixture heated under stirring to 110°C for 48 h. The reaction was then cooled to room temperature and the remaining solids are washed with chloroform, hot deionized water, and methanol (200 mL each) to remove catalyst, salt and oligomers, and then dried 72 h in a vacuum oven at room temperature to yield the corresponding amine networks. (Scheme 7)

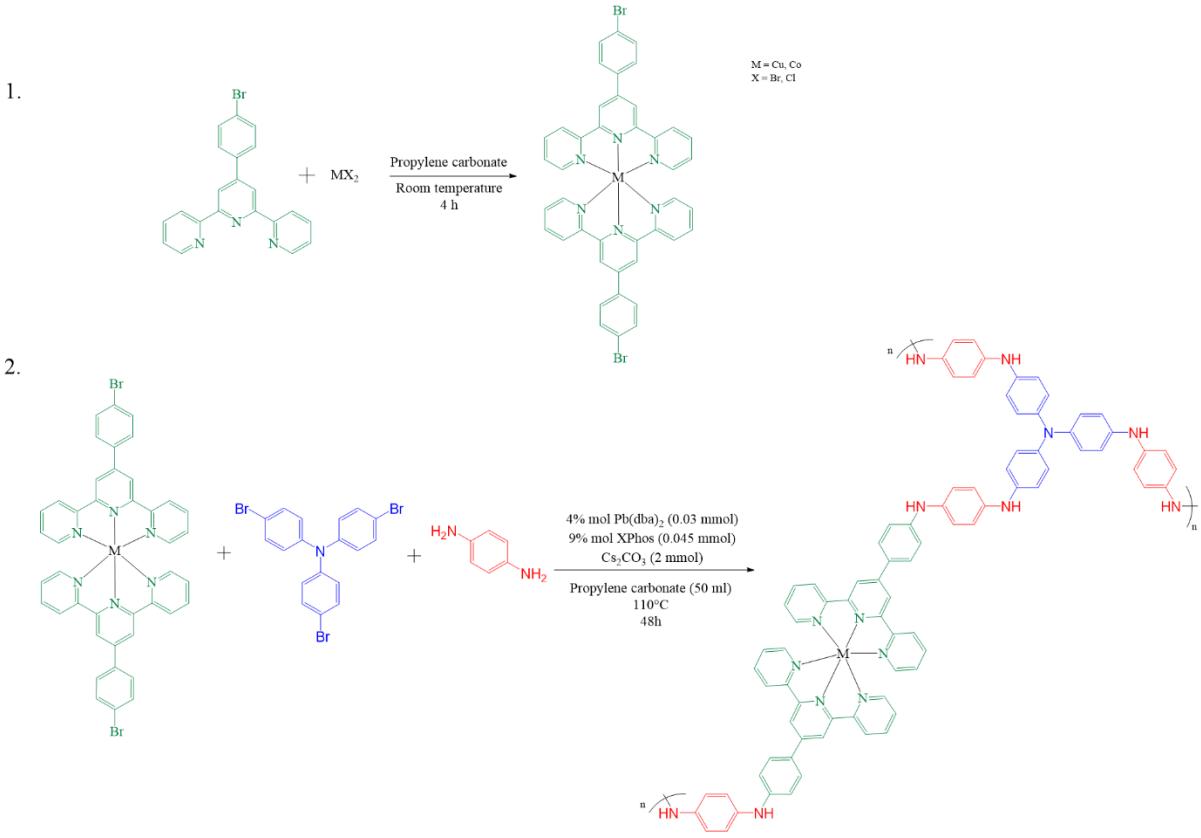

Scheme 7 Synthesis of metal-containing CMP-TPs by Route 1

The same reaction was also carried out by using 4,4'-dibromo-2,2'-bipyridine (0.1 mmol, 31.4 mg) and metal salt (0.1 mmol, $CuBr_2$ (0.1 mmol, 22.3 mg) or $CoCl_2$ (0.1 mmol, 12.9 mg)) (Scheme 8). The yields of the samples are shown in Table 6. The synthesis with $CuBr_2$ resulted in very low yields.

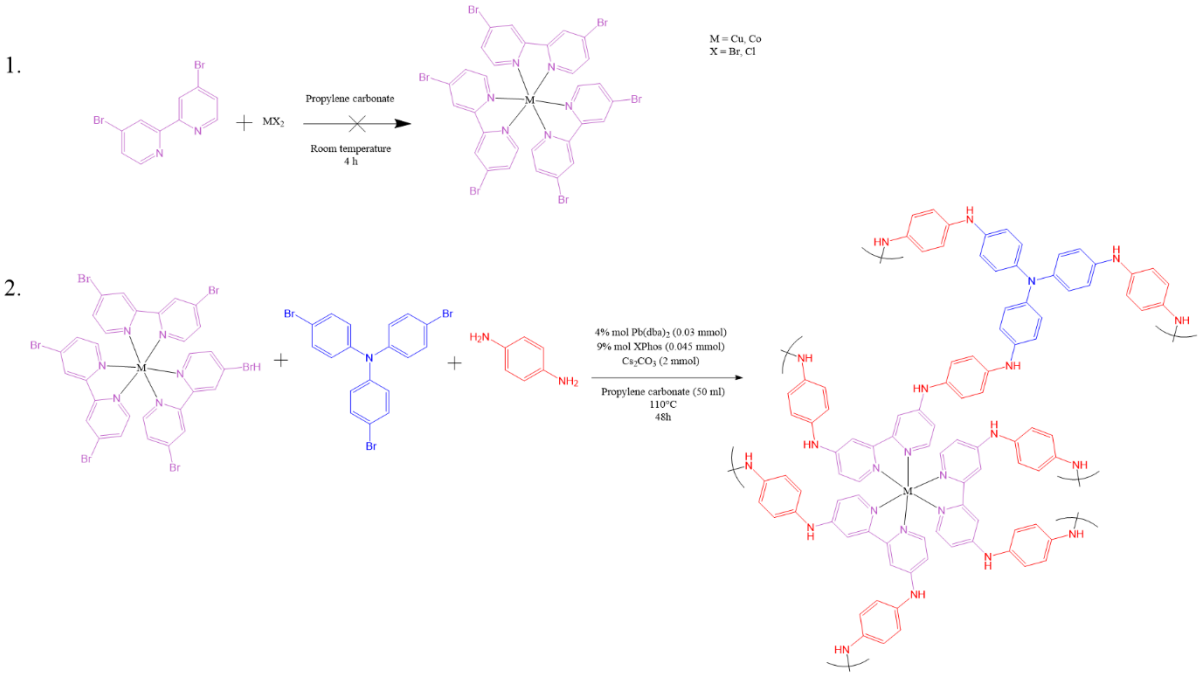

Scheme 8 Synthesis of metal-containing CMP-BPs by Route 1

Table 7 The corresponding yields of metal-containing CMPs synthesised by Route 1

Name	Pyridine unit, (mmol)	Metal salt	Yield %
CMP-TP-1-5	TP (0.1)	$CoCl_2$	15.2
CMP-TP-1-6	TP (0.1)	$CuBr_2$	---
CMP-BP-1-5	TP (0.1)	$CoCl_2$	12.2
CMP-BP-1-6	TP (0.1)	$CuBr_2$	---

2.4.2. Post-Polymerisation Metalation of CMPs (Route 2)

In Route 2, the syntheses were carried out by adding a metal salt to the already synthesised CMPs in deionized water. For this method, two previously synthesized polymers were used (CMP-TP-1-1 and CMP-BP-1-1). (Scheme 9 and Scheme 10)

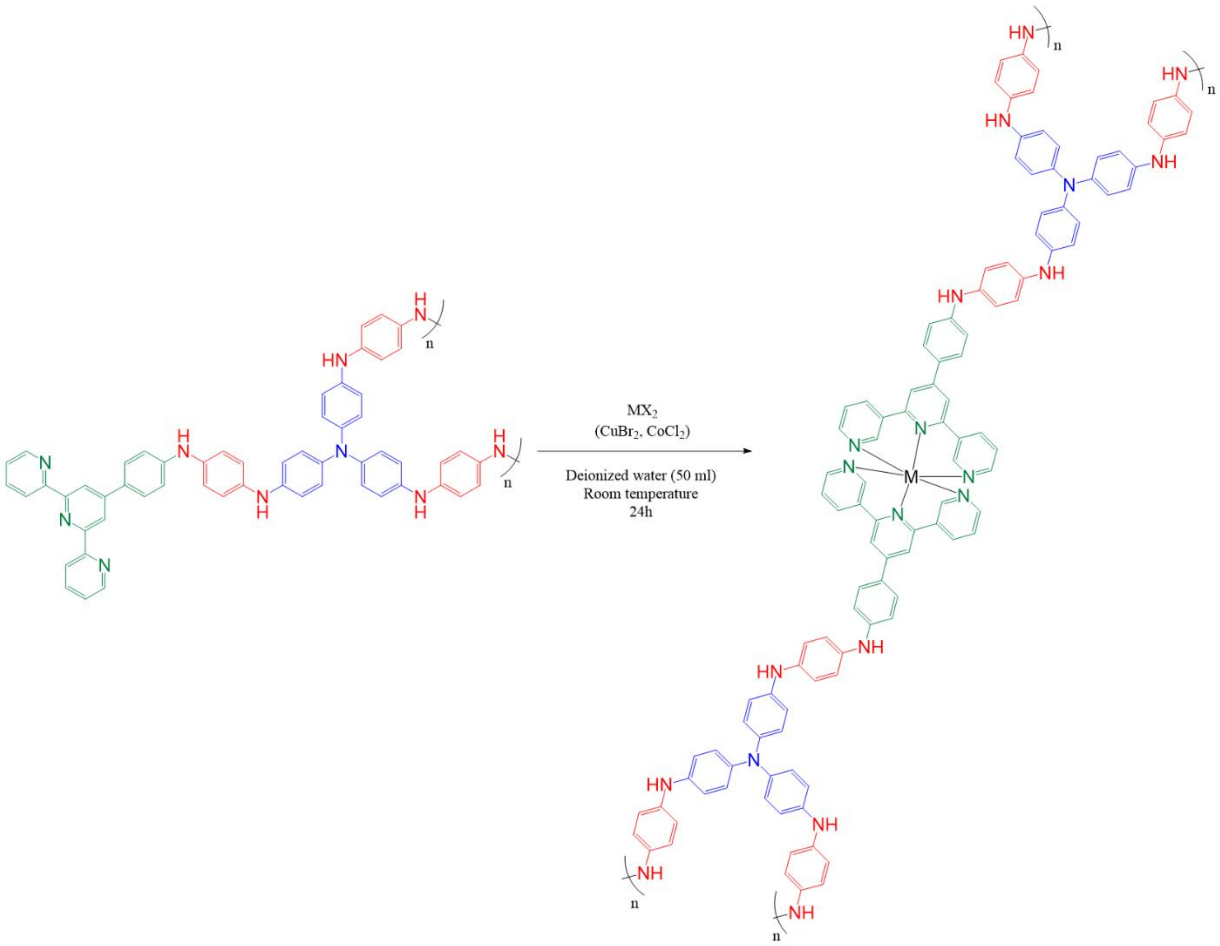

Scheme 9 Synthesis of metal-containing CMP-TPs by Route 2

Firstly, a Schlenk tube was charged with the pure polymer powder (50 mg) and dispersed into deionized water (50 ml) by sonicating for 2 h to form a homogeneous suspension, where the concentration of the solution was 1 mg mL^{-1}. A metal salt ($CuBr_2$ or $CoCl_2$) was added to the suspension under continuous stirring, with the salt concentration 0.25 mol L^{-1}. After stirring 24 hours under room temperature, the product was filtered and washed with deionized water to remove any impurities and unbound salts, and then dried 72 h in a vacuum oven at room temperature to yield the corresponding material.[130]

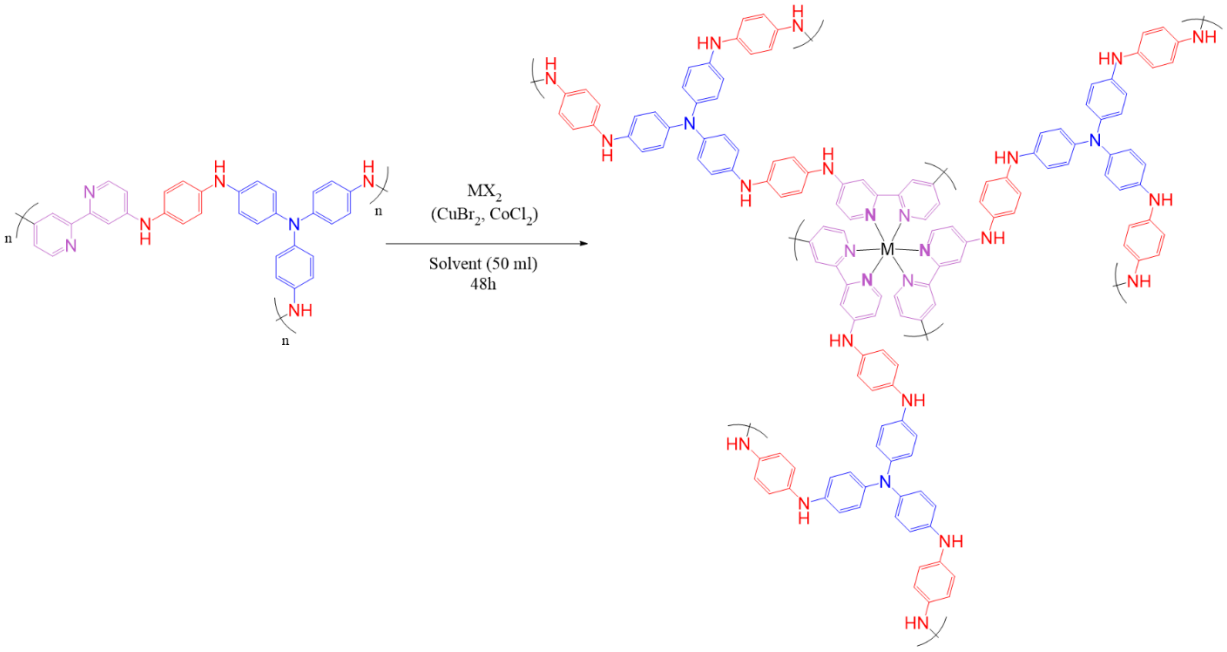

Scheme 10 Synthesis of metal-containing CMP-BPs by Route 2

The same reaction was also carried out using CMP-BP-1-1 and metal salts in two different reactions) (Scheme 10). The yields of these reactions are shown in Table 8.

Table 8 The corresponding yields of metal-containing CMPs synthesised by Route 2

Name	Pyridine unit (mmol)	Metal salt	Yield
CMP-TP-1-1-Cu	TP (0.1)	$CuBr_2$	90.11%
CMP-TP-1-1-Co	TP (0.1)	$CoCl_2$	89.72%
CMP-BP-1-1-Cu	TP (0.1)	$CuBr_2$	89.65%
CMP-BP-1-1-Co	TP (0.1)	$CoCl_2$	90.22%

2.5. Gas Adsorption-Desorption Measurements

Samples were dried on a Schlenk line for 24 h at 120 °C and 150 °C for materials synthesised by toluene and propylene carbonate, respectively. Gas sorption measurements were performed using a Quantachrome Autosorb-1MP. Degassing of the samples was performed under high vacuum in three steps: first the sample was heated to 50 °C at 1 °C min^{-1} then

held for 10 min, the sample was then heated to 100 °C at 2 °C min^{-1} and held for 100 min, and finally the sample was heated to 150 °C at 2 °C min^{-1} and held for 200 min.

Nitrogen adsorption/desorption measurements were performed at 77.4 K. CO_2 adsorption/desorption isotherms were recorded at 273 and 298 K. The specific surface areas were calculated by applying the Brunauer Emmett Teller (BET) model to adsorption or desorption branches of the isotherms (N_2 at 77.4 K) using the QuadraWin 5.05 software package. Analysis of the isotherms by commercialized Non-Local Density Functional theory (NLDFT) methodology was performed using the QuadraWin 5.05 package.

2.6. CO_2 Electrochemical Reduction

With a focus on characterizing the electrocatalytic activity of the synthesized materials in this study (CMP-TPs and CMP-BPs) for CO_2 electrochemical reduction, a three-electrode H-cell is used in the experimental setup as seen in Figure 11. The three electrodes used in the setup are: a glassy carbon as the working electrode on which a prepared CMP sample (see below) is drop cast, a calomel electrode as reference electrode, and Pt wire as counter electrode. To conduct an electrical current, potassium bicarbonate (0.1 M $KHCO_3$) is used as electrolyte. The electrolyte is saturated with argon (Ar) and CO_2 in two different containers for approximately 30 to 45 minutes before starting the experiment. The electrolyte bubbled with Ar is deoxygenated and is used for control measurements. The CO_2 saturated electrolyte is prepared by first bubbling Ar through to deoxygenate the solution, then CO_2 bubbled through.

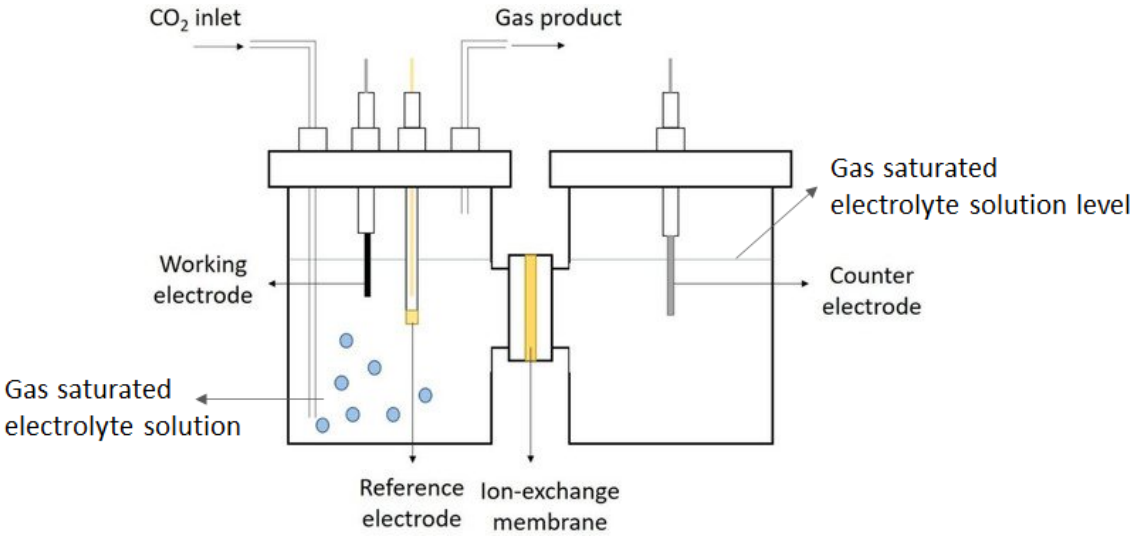

Figure 11 H-cell setup. Reproduced from reference [102]

Samples were finely ground till obtaining homogeneous powder using a mortar and pestle. 10 µL of Nafion and 1000µL of isopropanol were added to 0.2 mg of the fine powder sample and sonicated for 10 minutes. On a glassy carbon electrode, 40 µL of the dispersion is drop cast and dried in a vacuum oven at room temperature.

Cyclic voltammograms were recorded between -1.0 V and +1.0 V vs SCE (20 mV S^{-1}, 20 scans). After the measurement were taken, the potentials were converted to RHE with the help of the equation given below:

$$\mathrm{E(RHE)} = \mathrm{E(SCE)} + 0.242 + 0.059\,\mathrm{pH} \qquad (7)$$

2.7. Materials and Instrumentation

2.7.1. Chemicals

Table 9 List of chemicals

CAS NO.	Name	Purity	Source
89972-76-9	4'-(4-Bromophenyl)-2,6':2',2''-terpyridine	98%	Alfa Aesar
18511-71-2	4,4'-Dibromo-2,2'-bipyridine	98%	Thermo Scientific
564483-18-7	2-dicyclohexylphosphino-2',4',6'-triisopropylbiphenyl	98%	Sigma-Aldrich
123-91-1	1,4-Dioxane	Laboratory reagent grade	Fisher Chemical
67-64-1	Acetone	Puriss. p.a. ACS reagent. Reag. ISO, reag. Ph. Eur., >= 99.5% (GC)	Sigma-Aldrich
75-05-8	Acetonitrile	Laboratory reagent grade	Fisher Chemical
32005-36-0	Bis (dibenzylideneacetone) palladium(0)	N/A	Sigma-Aldrich
534-17-8	Caesium carbonate	ReagentPlus, 99%	Sigma-Aldrich
67-66-3	Chloroform	Puriss. p.a., reag. ISO, reag. Ph. Eur. 99.0% - 99.4% (GC)	Sigma-Aldrich
7646-79-9	Cobalt(II) chloride	Anhydrous, 97%	Sigma-Aldrich
7789-45-9	Copper(II) bromide	Anhydrous, 99%	Alfa Aesar
75-09-2	Dichloromethane	Puriss., meets analytical specification of Ph. Eur., NF,	Sigma-Aldrich

CAS NO.	Name	Purity	Source
		>= 99% (GC)	
67-68-5	Dimethyl sulfoxide	Analytical reagent grade, anhydrous, 99.9%	Fisher Chemical, Merck
64-17-5	Ethanol	99.8 % anhydrous, denatured	Sigma-Aldrich
141-78-6	Ethyl acetate	Puriss. p.a., ACS reagent, reag. ISO, reag. Ph. Eur., >= 99.5% (GC)	Sigma-Aldrich
67-56-1	Methanol	Anhydrous solvent - synthesis grade >= 99.9%	Fisher Chemical
31175-20-9	Perfluorinated resin solution containing Nafion ™ 1100W	N/A	Sigma-Aldrich
68-12-2	N,N-dimethylformamide	Laboratory reagent grade >= 99%	Fisher Chemical
540-69-2	n-Hexane	puriss. p.a., ACS reagent, reag. Ph. Eur. >= 99% (GC)	Sigma-Aldrich
872-50-4	N-Methyl-2-Pyrrolidone	ACS reagent, ≥99.0%	Sigma-Aldrich
106-50-3	p-phenylenediamine	97%	Alfa Aesar
108-32-7	Propylene carbonate	Anhydrous, 99.7%	Merck
865-48-5	Sodium tert-butoxide	98%	Acros organics
75-65-0	tert-Butanol	99%	Alfa Aesar
109-99-9	Tetrahydrofuran	contains 240 ppm BHT as inhibitor, puriss. P.a., ACS reagent, Reag. Ph. Eur. >= 99.9%	Sigma-Aldrich
108-88-3	Toluene	Laboratory reagent	Fisher Chemical

CAS NO.	Name	Purity	Source
		grade >= 99%	
4316-58-9	tris(4-Bromophenyl)amine	98%	Santa Cruz Biotechnology
1330-20-7	Xylenes	Laboratory reagent grade	Fisher Chemical

2.7.2. Instrumentation

Table 10 List of instruments

Name	Company & Type
FT-IR	PerkinElmer Spectrum 100 FT-IR spectrometer
UV/Vis NIR Spectrometer	UV-2600 Shimadzu spectrophotometer
Powder X-ray Diffraction	Bruker D8 Advance diffractometer (40 kV, 40 mA) equipped with a PSD LynxEye detector
SEM/EDX	JEOL JSM 5600LV
Gas Sorption Analyser	Quantachrome Autosorb iQ automated gas adsorption analyser
Cyclic voltammetry potentiostat-galvanostat (CV)	Model 273A, (EG&G Princeton Applied Research, USA)

2.7.3. Software

Table 11 List of software

Software
ChemDraw Professional 20.0
Origin 2018b (academic)
QuadraWin 5.05

3. Results and Discussion

The PTPA network reported by the Faul group in 2014[61] with (1:1.5) stoichiometric ratio has low surface area (52 $m^2 g^{-1}$, Table 15, page 64). Studies have shown that along with large surface area and pore volume, the CO_2 uptake performance of porous materials may also be improved by incorporating electron-rich groups such as N, O, S, and other heteroatoms[11, 131, 132], in particular nitrogen.[48] CO_2 uptake could be enhanced owing to the fact that nitrogen would act as a Lewis base, with CO_2 acting as a Lewis acid. For this particular reason, this study was carried out to synthesise novel nitrogen-rich CMPs for CO_2 capture and conversion applications. To ensure that there are sites within the porous framework that will act as binding sites, terpyridine and bipyridine building blocks were incorporated into the PTPA framework. The terpyridine derivative used was 4'-(4-bromophenyl)-2,6':2',2''-terpyridine (TP), and the bipyridine derivative used was 4,4'-dibromo-2,2'-bipyridine (BP) (as can be seen in Figure 10). While TP contains one bromo reactive unit, BP contains two bromo reactive units. This arrangement allows the bipyridine unit to extend the polymer chain to two sides, and for the terpyridine to block one end of the chain and act as a "stopper".

The methods applied to characterise the resulting polymers were XRD, FT-IR, solid-state UV/Vis NIR and SEM. N_2 and CO_2 gas adsorption analyses were performed to determine surface area, porosity and CO_2 uptake capacities of the networks.

3.1. Properties of the CMPs

In the first part of this study, the CMP-TP and CMP-BP networks, which can also be called base CMPs, were synthesised by the process reported by the Faul research group in 2014.[61] The BH reaction opens up a pathway to form carbon–nitrogen bonds between aryl halides and amines. In this study, an aniline-based diamine linker (PPDA), a trihalide core (TBPA) and pyridine-based mono or dihalide co-monomers (TP, BP) have been utilized to form two different types of CMPs. The details of the synthesis of CMP-TPs and CMP-BPs are given in Chapter 2, pages 23 and 24.

The (co-monomer+core):linker ratio was kept at 1:1.5, while the co-monomers (TP and BP) to the core composition was varied from 0.1:0.9 to 0.2:0.8, 0.3:0.7 and 0.4:0.6 to find the optimal ratio that results with the reaction that gives the best yield and CO_2 uptake properties. The cross-coupling reaction with TP in toluene resulted in dark blue, insoluble powder with yields around 30%, and reaction with BP in toluene resulted in a dark green, insoluble powder with yields around 40%. Both reactions showed maximum yield at a 0.1:0.9 co-monomer to core molar ratio. To confirm that the coupling reaction was successful, spectral and morphological analysis results and results of the surface area, porosity and CO_2 uptake capacities of the networks are discussed below.

3.1.1. XRD Investigations

X-ray diffraction (XRD) is a non-destructive technique that provides detailed information about chemical composition, physical properties and crystallographic structure of materials. CMPs are known as non-crystalline materials (amorphous solids). Therefore, they do not diffract X-rays at a particular single angle and resulting in observed broad peaks in the spectra. This technique helps to understand whether the synthesized amorphous CMPs has been purified from starting materials or by-products that may occur after synthesis.

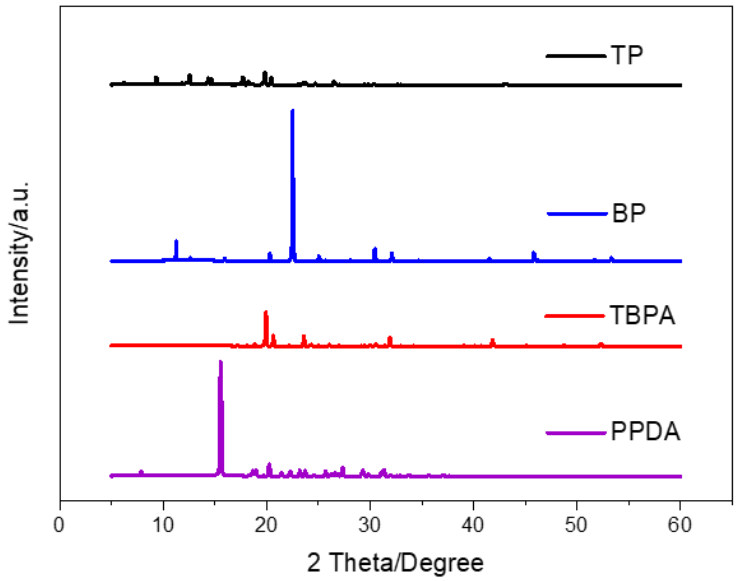

Figure 12 X-Ray diffraction patterns of the starting materials

As can be comprehended from Figure 12, the starting materials are crystalline with unique X-ray diffraction patterns and well-defined Bragg peaks.

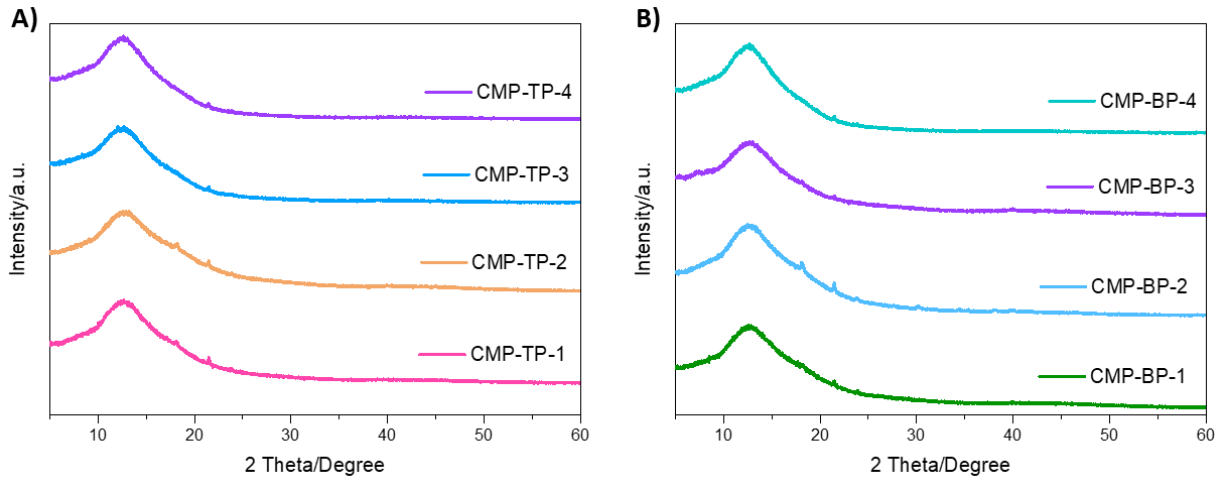

Figure 13 X-Ray diffraction patterns of **(A)** CMP-TPs and **(B)** CMP-BPs

The powder X-ray diffractograms (Figure 13) of the synthesised CMPs demonstrate broad peaks at approximately 2Θ = 10-15°. The particular reason for the broad peaks is the lack of order in the arrangement of the materials' structure, causing the X-rays to scatter in many directions. It can therefore be declared that the new synthesised materials, different from the starting materials, are amorphous. Other than the broad peaks, small sharp peaks are visible in most diffractograms. In addition, although the materials were thoroughly washed by Soxhlet extraction, there are also small crystalline peaks observed at 2Θ = 17° and 22°, which do not belong to the starting materials as can be seen compared with the patterns in Figure 12. To identify the phases that are present, the diffraction pattern of the samples were compared to a database containing reference patterns with the help of Match! Software. According to the compared patterns, it was evaluated that the crystalline peaks could belong to NaBr, that may have formed during the synthesis (see Figure 14). Figure 14 was taken from The Materials Project[133, 134] database, where the X-ray diffraction patterns were provided by computational chemistry calculations.

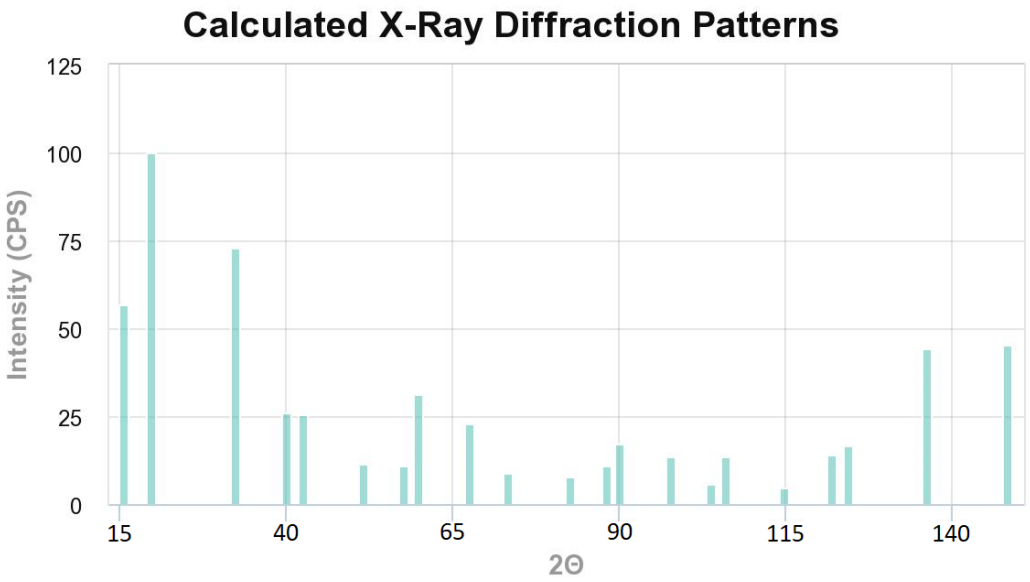

Figure 14 XRD pattern of NaBr provided from The Materials Project[133, 134]

NaBr is highly soluble in water. Therefore, the materials were thoroughly washed by Soxhlet extraction with water again. However, the crystalline peaks that belong to NaBr were still observed. It was interpreted that NaBr may have been trapped inside the polymerised CMP structures, or potentially interacted with the lone pairs of the nitrogen found in the pyridine units, making it hard to wash away.

Another reason for the unwanted crystalline peaks could be owing to the Vaseline/paraffin wax used to prevent the sample from falling out of the sample holder. The information related to the impurity peaks were evaluated from articles and could be seen in Figure 15.

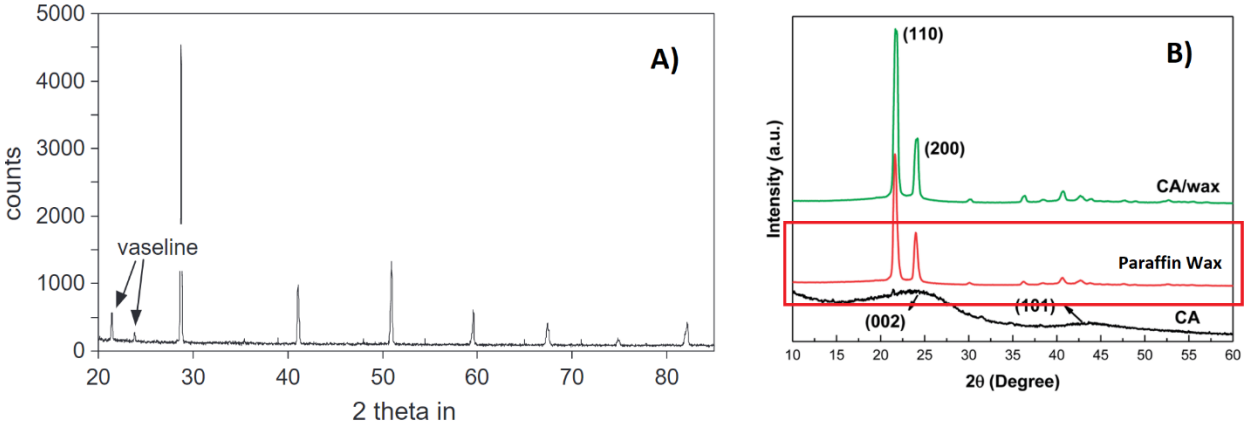

Figure 15 XRD patterns showing similar patters owing to vaseline and paraffin wax reproduced from **A)** reference [135] and **B)** reference [136]

3.1.2. FT-IR Spectroscopy Investigations

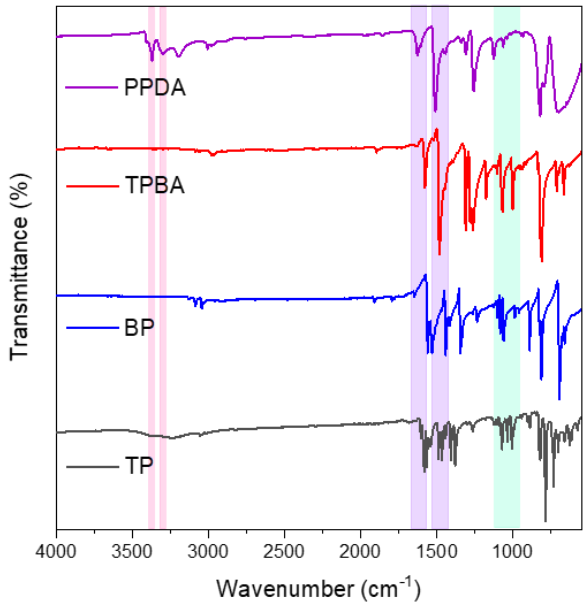

Figure 16 FT-IR spectra of the starting materials

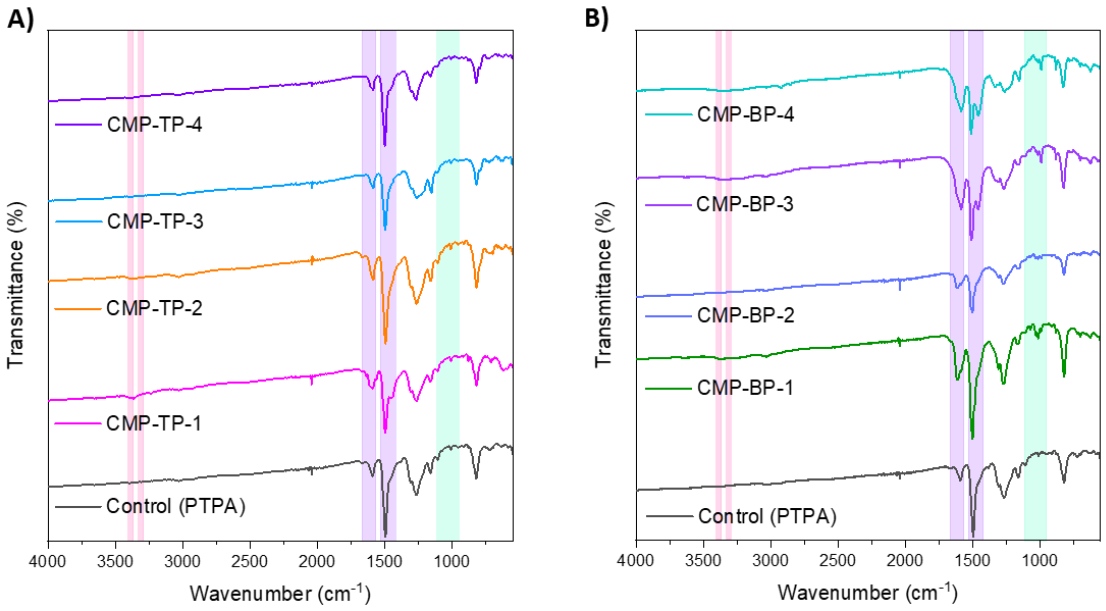

Figure 17 FT-IR spectra of **(A)** CMP-TPs and **(B)** CMP-BPs along with the control material

The FT-IR spectra of the CMP networks synthesised with different core and co-monomer-to-linker ratios indicated that the synthesis of these polymers was successful. As can be seen in Figure 17, the samples synthesised with different ratios exhibit similar spectra with the control material, PTPA (Figure 17). The spectra show that the peaks at ~3377 and 3301 cm^{-1} from the linker owing to the stretching vibration of the primary amine are absent. This

result means that the amine groups of the linker have all participated in the coupling reaction to form the porous networks. Also, it can be said that primary amines are exchanged by secondary amine fragments owing to the shift in the bands from 1630 to 1645 cm^{-1}. The peaks that belong to the aromatic C-Br from TBPA (observed at 1005 and 1075 cm^{-1}, from BP at 1062 and 1086 cm^{-1}) and from TP at (1008 and 1073 cm^{-1}) are also absent, which indicates that the bromide groups have all been eliminated to form C-N bonds and that the BH coupling was successful. The two bands at 1499 and 1589 cm^{-1} are related, respectively, to the stretching of B-type (benzenoid-type, N-B-N,) and Q-type (quinoid-type, N=Q=N) bonds. The bending band at 820 cm^{-1}, which was present in the spectra of all samples as seen in Figure 17, indicate the presence of -CH- from substituted benzene.

3.1.3. UV-Vis-NIR Investigations

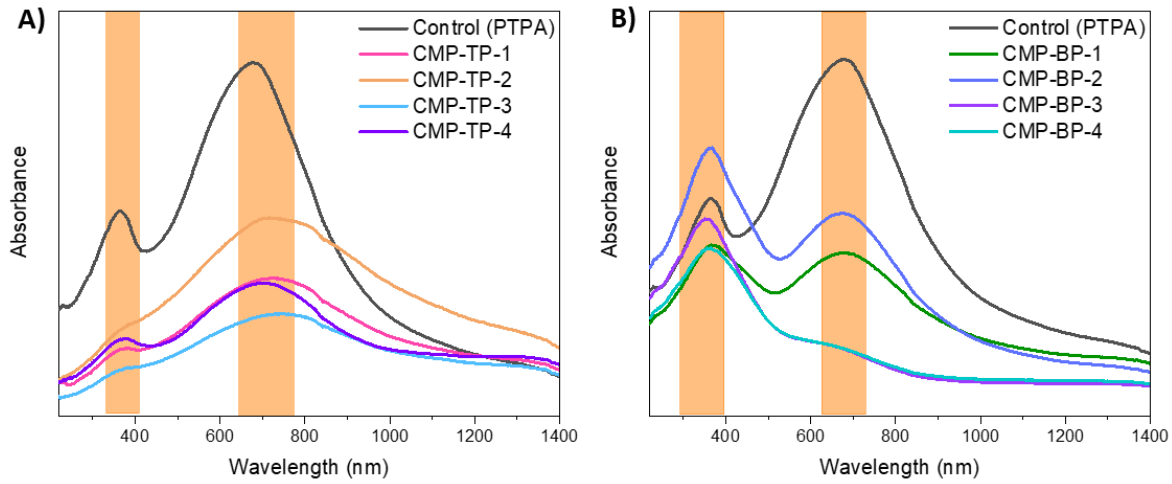

Figure 18 Solid-state UV-Vis-NIR spectra of (A) CMP-TPs and (B) CMP-BPs along with control material

Solid-state UV-Vis-NIR spectra of synthesized CMPs shown in Figure 18 exhibited two peaks, with a strong bathochromic shift owing to the extended conjugation, at 380 and 650 nm. These peaks attributed to the π–π* transition of benzenoid rings and n-π* transition of quinoid rings from the non-bonded electron pair of a nitrogen bonded to a benzenoid ring, respectively. Quinoid are oxidized derivatives of aromatic compounds. These results confirmed the creation of extended conjugated networks. Results also showed that the quinoid structure is more dominant in CMPs containing terpyridine, and in CMPs containing bipyridine benzenoid structure is more dominant.

3.1.4. SEM Investigations

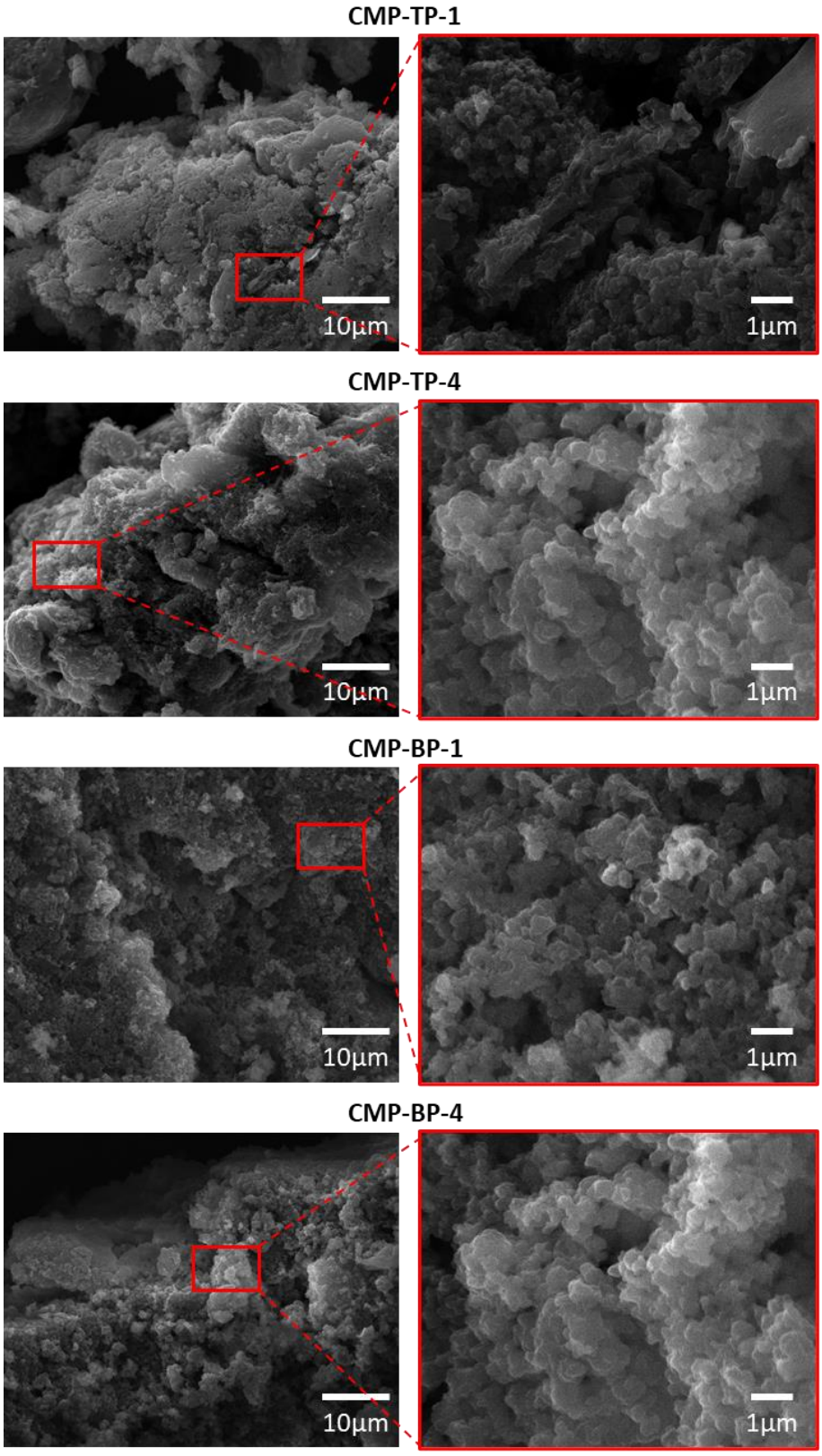

Figure 19 SEM images of CMP-TP and CMP-BP samples at different core-to-linker ratios of CMP-TP-1, CMP-TP-4, CMP-BP-1 and CMP-BP-4, respectively.

The SEM images, shown in Figure 19, are from the materials that contain the lowest and the highest co-monomer content. Even though they do not provide immediate insight into the porosity or the ability to take up CO_2, these images provide valuable information in porosity studies according to the degree of aggregation and nanoparticles shapes. The samples exhibit spherical morphologies of amorphous particles in the range of ~1 µm in size. As can be seen in Figure 19, changing the ratios of the starting materials has not changed the morphologies, where CMP-TPs and CMP-BPs all exhibited similar morphologies. The highly aggregated nanoparticles contribute to the surface area by forming interstitial spaces.

3.2. HSPs Results and Role of the Solvent

This study was undertaken to find a suitable solvent for the synthesis of CMP-TPs and CMP-BPs to optimize the yield and surface area, 2mg of the products were added in 5 mL of different solvents. The suspensions were sonicated for 24 hours, left undisturbed for 24h, and the UV-Vis spectra were recorded.

3.2.1. Solubility Tests for CMP-TP-1

In order to compare the dispersions, UV-Vis spectroscopy was performed at the same concentrations of CMP-TP-1 in sixteen different solvents (Figure 20).

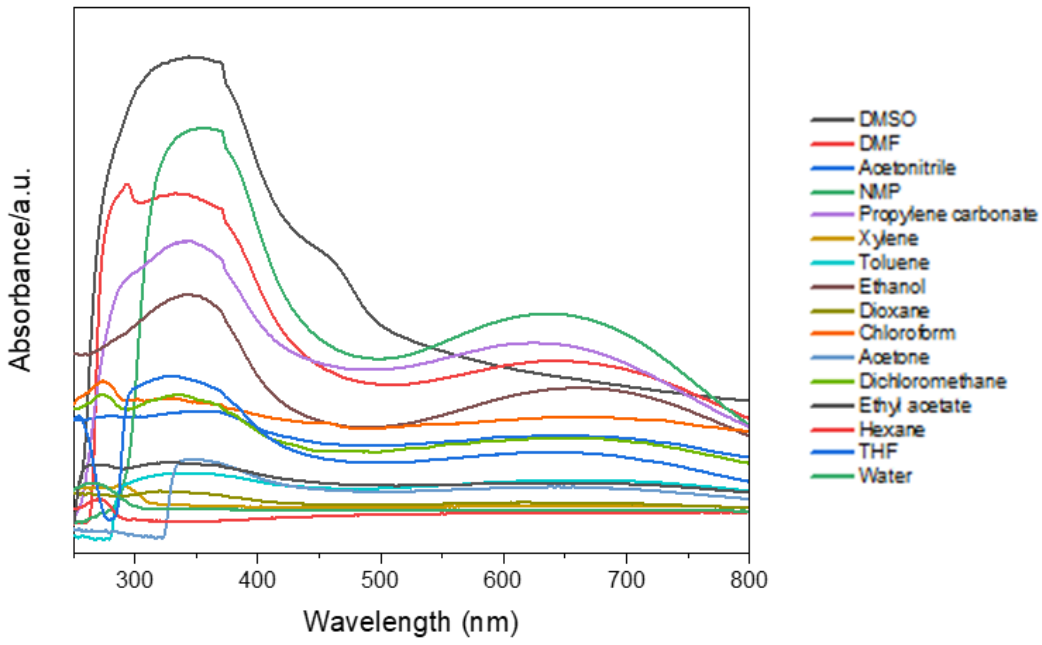

Figure 20 UV-Vis spectra for CMP-TP-1 in sixteen different solvents

Based on the intensities of UV-Vis spectra, the HSPs (as introduced in Section 1.3) of **CMP-TP-1** was calculated by first recording the maximum absorbance of each suspension corresponding to HSPs of the solvents, following by fitting with a B-Spline method.[14] The maxima established by B-spline fitting corresponds to HSPs of **CMP-TP-1**, which are δ_D=18.85, δ_P=12.82 and δ_H=10.60 (Figure 21). The total solubility parameter (δ_T) obtained from the fitting plot is 26.77 (Figure 21). By using the obtained individually fitted parameters, the total HSPs was calculate as 25.14, with an acceptable 6.1% error in the fitting plot.

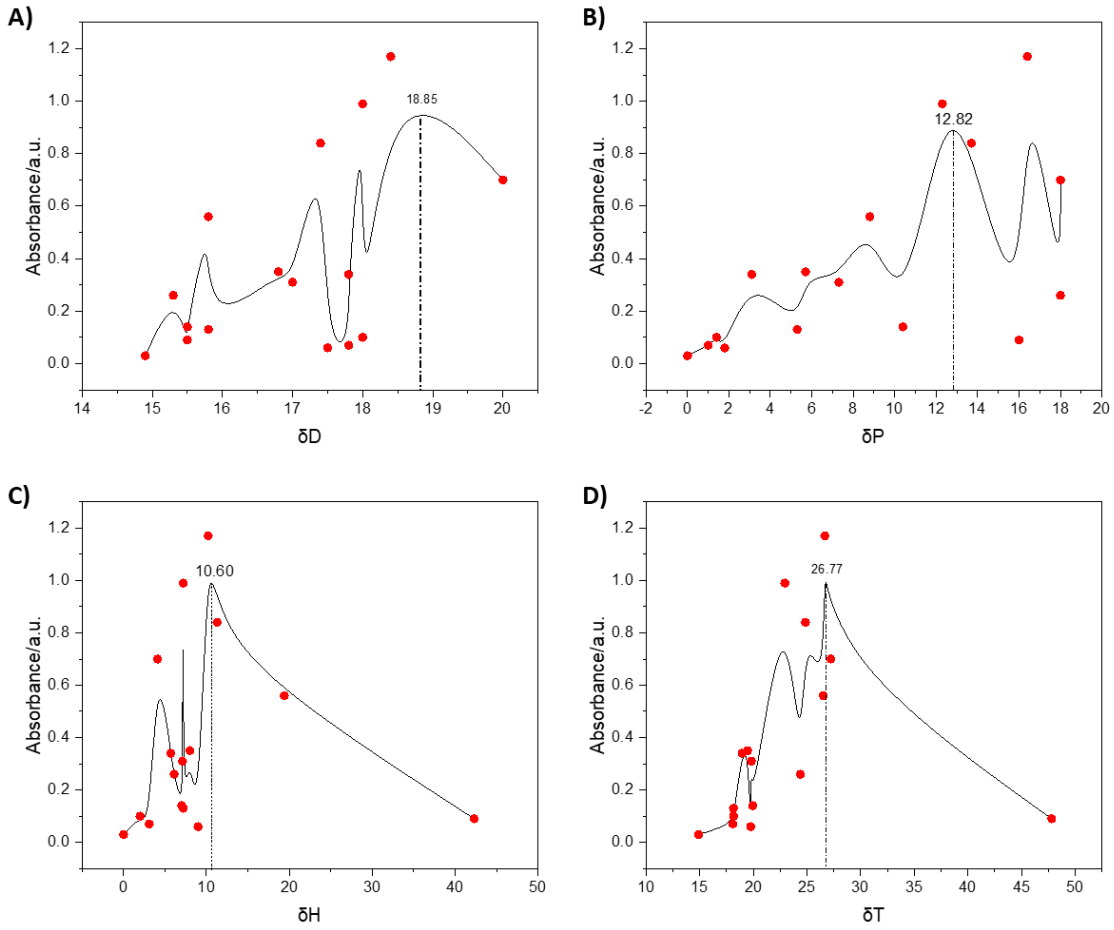

Figure 21 CMP-TP-1 concentration measured by UV/VIS spectroscopy, plotted with published Hansen solubility parameter of the chosen solvents: **(A)** disperse-, **(B)** polar-, **(C)** hydrogen-, **(D)** total solubility parameters

With the comparison of the δ_T of the solvent and the polymer, respectively, the solvents are then classified into three groupings: if the absolute difference | $\Delta\delta_T$ | is greater than 3 it is a poor solvent, if the absolute difference | $\Delta\delta_T$ | is between 1 and 3 it is an intermediary solvent, and if the absolute difference | $\Delta\delta_T$ | is less than 1 it is a suitable solvent for the dissolution of the polymer.[137] The HSPs values of the solvents used for this research were

found in literature.[76] The results of the HSP calculations for CMP-TP-1 is listed in Table 12, where the following three solvents were found suitable: ethanol, DMSO and propylene carbonate. As can be seen from Table 13, according to HSPs calculation and result, the $|\Delta\delta_T|$ of toluene and the polymer is greater than 3 and is not suitable for dissolving CMP-TP-1.

Table 12 HSPs and relative δ_T between solvents studied and CMP-TP-1

Solvent/Compound	δ_D	δ_P	δ_H	δ_T	$\|\Delta\delta_T\|$
CMP-TP-1	**18.85**	**12.82**	**10.60**	**26.77**	**-**
DMSO	*18.4*	*16.4*	*10.2*	*26.67*	*0.1*
DMF	17.4	13.7	11.3	24.86	1.91
Acetonitrile	15.3	18	6.1	24.39	2.38
NMP	18	12.3	7.2	22.95	3.82
Propylene carbonate	*20*	*18*	*4.1*	*27.22*	*0.45*
Xylene	17.8	1	3.1	18.09	8.68
Toluene	18	1.4	2	18.16	8.61
Ethanol	*15.8*	*8.8*	*19.4*	*26.52*	*0.25*
Dioxane	17.5	1.8	9	19.76	7.01
Chloroform	17.8	3.1	5.7	18.95	7.82
Acetone	15.5	10.4	7	19.94	6.83
Dichloromethane	17	7.3	7.1	19.82	6.95
Ethyl acetate	15.8	5.3	7.2	18.15	8.62
Hexane	14.9	0	0	14.9	11.87
THF	16.8	5.7	8	19.46	7.31
Water	15.5	16	42.3	47.81	21.04

**δ_D: dispersion interactions, δ_P: permanent dipole-dipole interactions, δ_H: hydrogen-bonding interactions*

The UV-Vis spectra for **CMP-TP-4**, **CMP-BP-1** and **CMP-BP-4** in the same sixteen solvents were also studied, and are presented, along with the B-spline plots and calculated HSPs results, in the Appendix, page 94. With the calculation of HSPs for **CMP-TP-4**, **CMP-BP-1** and

CMP-BP-4, the same solvents ethanol, DMSO and propylene carbonate were also found as optimal solvents for the d dispersion of the polymers.

The optimised synthesis conditions were only applied for the synthesised materials that contain highest (0.4mmol) and lowest (0.1mmol) TP and BP ratio. The result obtained by applying good solvents showed that further optimization could be made due to the extremely low yield or even no product being obtained. Researchers have shown that change in key reaction parameters such as solvent, base, temperature will influence the synthesis quite dramatically. By changing the solvent, it is possible that the other variables may now not be optimal for the reaction conditions. For example, the optimal base for a BH reaction may change depending on the polarity of the solvent used. Owing to it being a very strong base, Pd-catalysed coupling reactions with NaOt-Bu could lead to undesired side reactions and block the chains from polymerizing.[138] This observation has prompted the use of an alternative base. An inorganic base like Cs_2CO_3 could behave as a stronger base on account of the polarity of the solvent, which can increase the pKa value when dissolving.[139] With the change of base to Cs_2CO_3, the yields increased most for the reactions with propylene carbonate (from ~0.5% to 20-40%). It was then decided to move forward with this solvent. The same reaction was also carried out using toluene as solvent, thus investigating the influence of changing the base for these reactions.

3.2.2. XRD Investigations

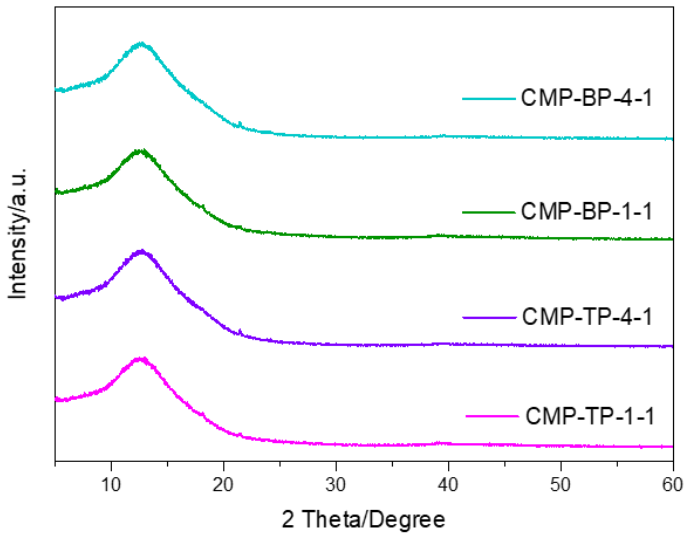

Figure 22 X-Ray diffraction patterns of reactions with propylene carbonate

The powder X-ray diffraction (Figure 22) determined from the CMPs synthesised with propylene carbonate demonstrates broad peaks at approximately 2Θ = 10-15°, which is same as seen in Section 3.1.1., page 40. It can therefore be declared that the new materials synthesised, different from the starting materials, are amorphous. Also, as same as in the first synthesised materials, there are also small crystalline peaks observed at 2Θ = 17° and 22° crystalline peaks at the materials synthesised with propylene carbonate, meaning that there are impurities. As mentioned in Section 3.1.1, the crystalline peaks could belong to CsBr that may have formed during the synthesis (see Figure 14), or the Vaseline/paraffin wax used to prevent the sample from falling out of the sample holder. (see Figure 15).

3.2.3. FT-IR Spectroscopy Investigations

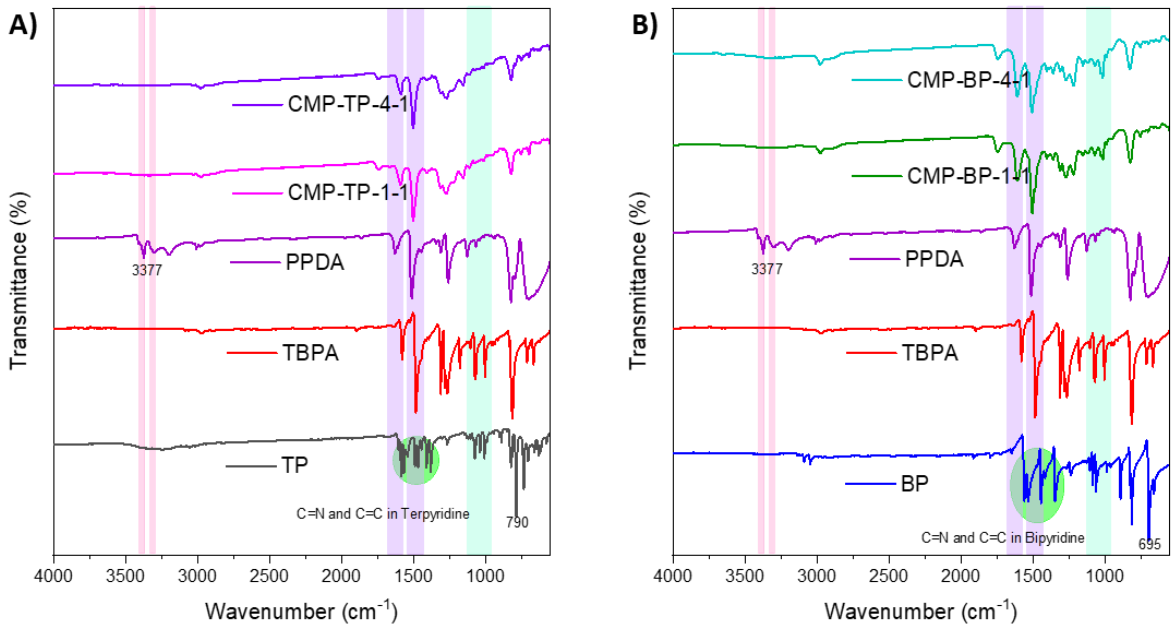

Figure 23 FT-IR spectra of the **(A)** CMP-TPs and **(B)** CMP-BPs synthesised with propylene carbonate along with the starting materials

The FT-IR spectra of the CMP networks synthesised in propylene carbonate with different core and co-monomer-to-linker ratios indicate that the synthesis of these polymers was successful. As can be seen in Figure 23, the samples synthesised exhibited similar spectra with the control CMP shown in Figure 17. The spectra show that the peaks at ~3377 and 3301 cm^{-1} from the linker (owing to the stretching vibration of the primary amine) are absent. This means that the amine groups of the linker have all participated in the coupling reaction to form the porous networks. Also, it can be said that primary amines are replaced

with secondary amine fragments owing to the shift in the bands from 1630 to 1645 cm^{-1}. The peaks that belong to the aromatic C-Br from TBPA (observed at 1005 and 1075 cm^{-1}), from BP (at 1062 and 1086 cm^{-1}), and from TP (at 1008 and 1073 cm^{-1}) are also absent, which indicates that the bromide groups have all been eliminated to form C-N bonds in successful BH coupling reaction. The two bands at 1499 and 1589 cm^{-1} are related, respectively, to the stretching of B-type (benzenoid-type, N-B-N,) and Q-type (quinoid-type, N=Q=N) bonds. The bending band at 820 cm^{-1}, which was present in the spectra of all samples as seen in Figure 22, indicate the -CH- of substituted benzene.

3.2.4. UV-Vis-NIR Investigations

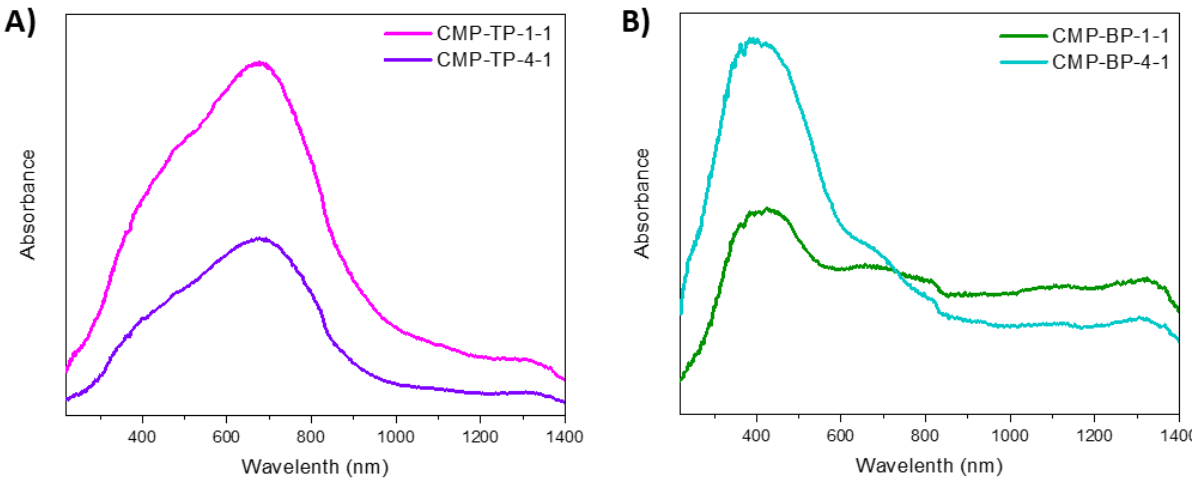

Figure 24 Solid-state UV-Vis-NIR spectrum of **(A)** CMP-TPs and **(B)** CMP-BPs synthesised with propylene carbonate

Solid-state UV-Vis-NIR spectra of CMPs synthesised with propylene carbonate shown in Figure 24 also exhibited two peaks like the control CMP, with a bathochromic shift from 380 to 400 nm and from 690 to 710 nm. These peaks are attributed to the π–π* transition of benzenoid and quinoid rings (charge transfer from HOMO of the benzenoid ring to LUMO of the quinoid ring), respectively. Results showed that the quinoid structure are more dominant in CMPs containing terpyridine, and in CMPs containing bipyridine benzenoid structure is more dominant. These results confirmed the creation of extended conjugated networks.

3.2.5. SEM Investigations

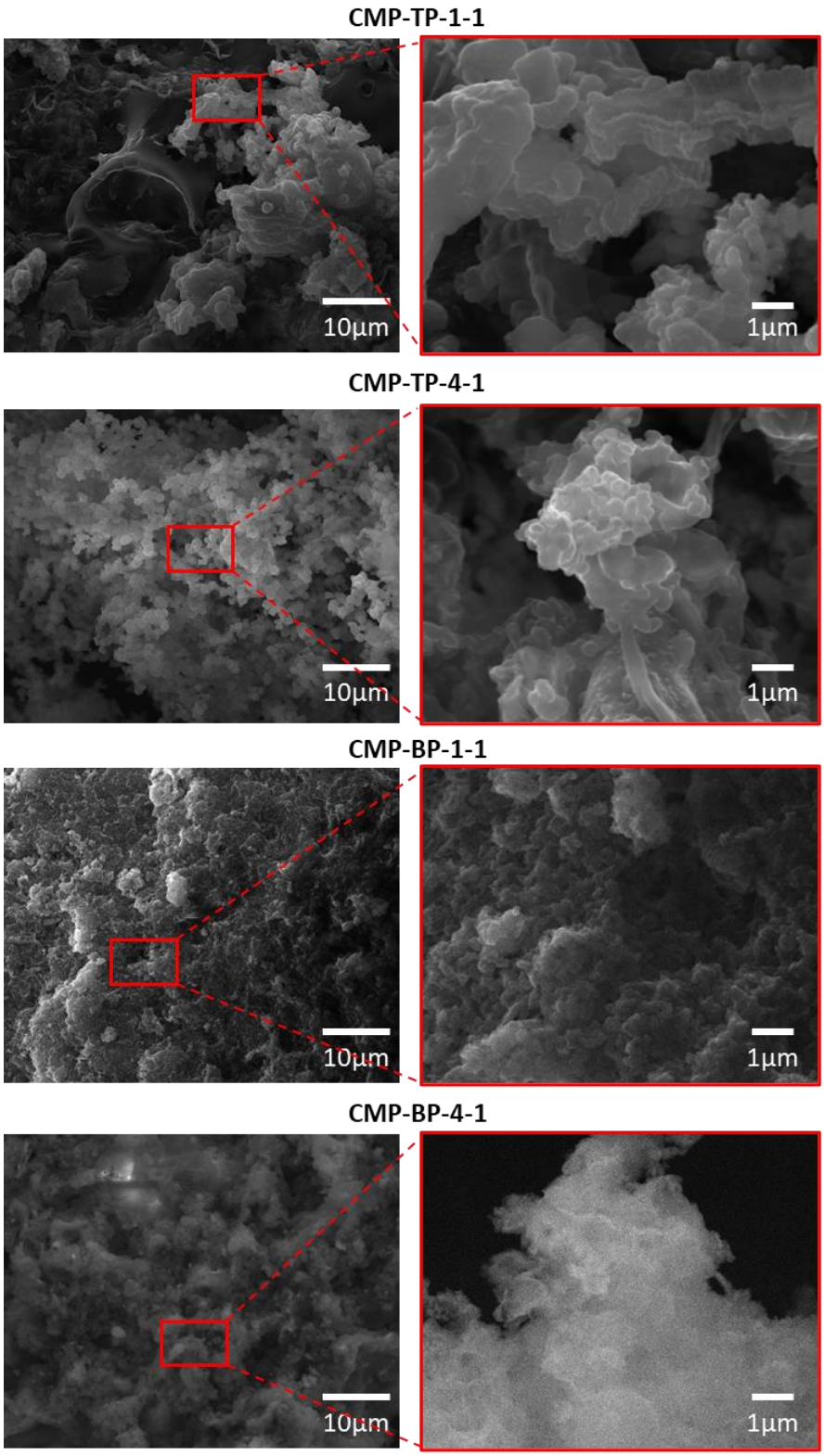

Figure 25 SEM images of CMP-TP and CMP-BP samples at different core-to-linker ratios synthesised in propylene carbonate

SEM images of the materials synthesized with propylene carbonate were taken to investigate their morphology (Figure 25). As mentioned before for synthesis with toluene, the images displayed valuable information for porosity studies according to the degree of aggregation and nanoparticles shapes. The samples mostly exhibit spherical morphologies of amorphous particles in the range of ~5 µm in size. As can be seen in Figure 25, changing the solvent has slightly changed the morphologies compared to the first synthesised CMPs, where all materials show highly aggregated nanoparticles contributing to the surface area by forming interstitial spaces.

3.3. Results for Higher Catalyst Loading

Pyridine units qualify as ligands for transition metals and form metal complexes owing to their Lewis basic character gained by the available lone pair of the nitrogen found in its structure. It is believed that the terpyridine and bipyridine units could be forming a complex with the palladium catalyst, resulting in not having enough catalyst for the cross-coupling reaction to occur. For this particular reason, the quantity of catalyst and ligand was increased by a factor of 10 (4% mol instead of 0.4% mol and 9% mol instead of 0.9% mol, respectively) to improve reaction conditions.

3.3.1. XRD Investigations

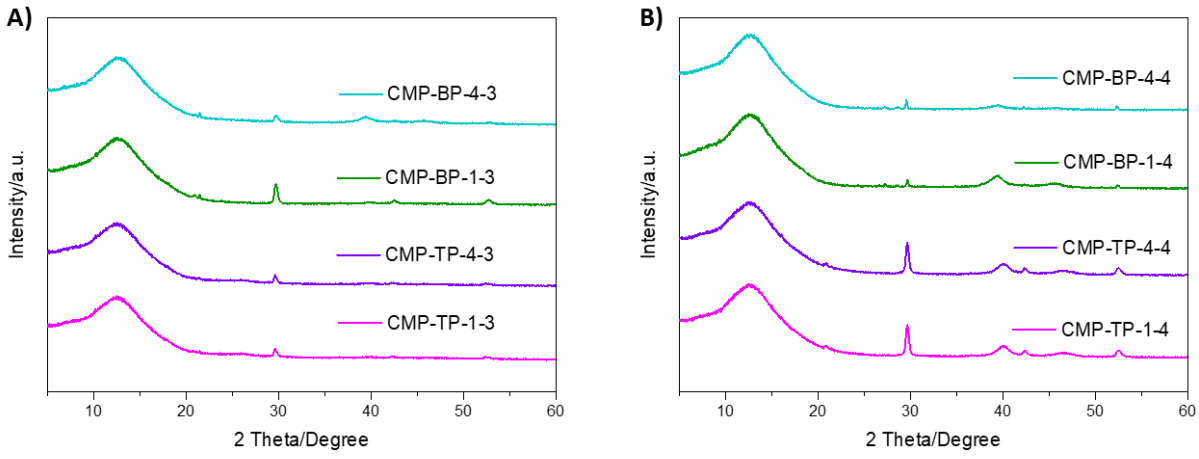

Figure 26 X-ray diffraction patterns from reactions with excess catalyst loading in **(A)** toluene and **(B)** propylene carbonate

The powder X-ray diffractogram (Figure 26) from the CMPs synthesised with an excess catalyst loading in toluene and propylene carbonate demonstrates broad peaks at approximately 2Θ = 10-15°, as found for the CMPs mentioned before. It can therefore be declared that new materials, different from the starting materials that are amorphous have been synthesised. In addition, similar to the situation mentioned in Section 3.3.1, although the materials were thoroughly washed by Soxhlet extraction, there are also crystalline peaks observed at 2Θ = 21°, 29°, 40° and 52°, which do not belong to the starting materials as can be seen compared with the patterns in Figure 12. To identify the phases that are present, the diffraction pattern of the samples were compared to a database containing reference patterns with the help of Match! Software. According to the compared patterns, it was evaluated that the crystalline peaks belong to CsBr, that may have formed during the synthesis (see Figure 26). Figure 26 was taken from The Materials Project[133, 134] database, where the X-ray diffraction patterns were provided by computational chemistry calculations.

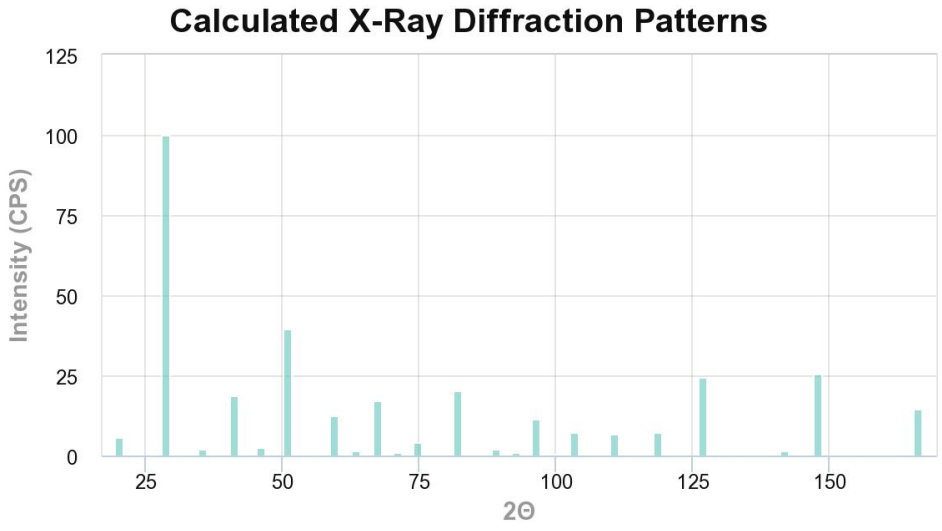

Figure 27 XRD patters of CsBr provided from The Materials Project[133, 134]

CsBr is highly soluble in water. Therefore, the materials were thoroughly washed by Soxhlet extraction with water again. However, the crystalline peaks that belong to CsBr were still observed. It was interpreted that CsBr may have been trapped inside the polymerised CMP structures, or potentially interacted with the lone pairs of the nitrogen found in the pyridine units, making it hard to wash away.

Another reason for the unwanted crystalline peaks could be owing to the Vaseline/paraffin wax used to prevent the sample from falling out of the sample holder, as mentioned in Section 3.1.1. The information related to the impurity peaks were evaluated from articles and could be seen in Figure 15.

3.3.2. FT-IR Spectroscopy Investigations

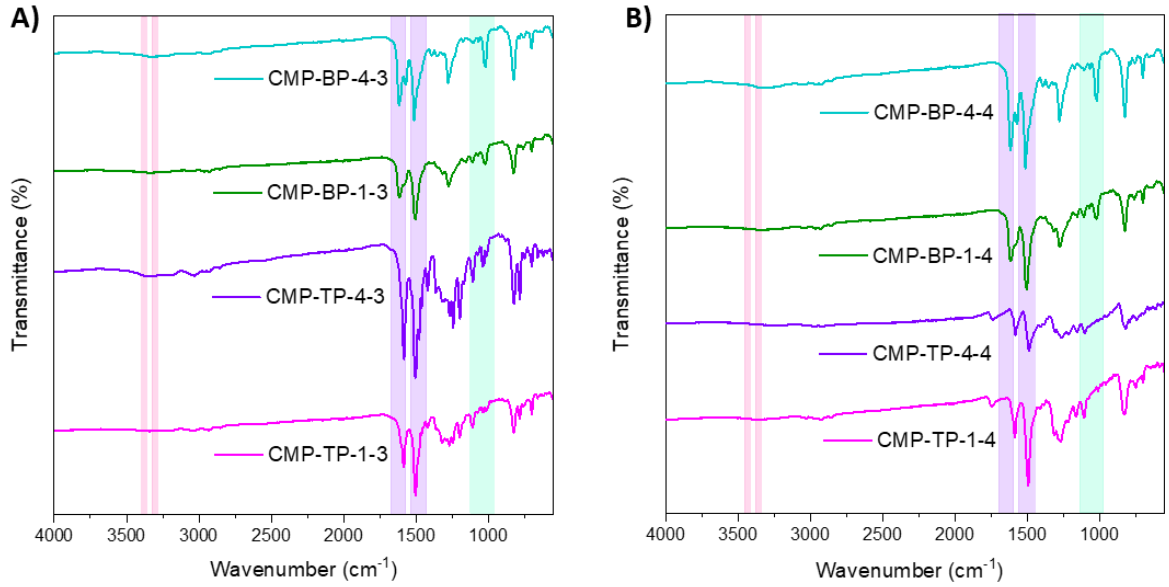

Figure 28 FT-IR spectra of reactions with excess catalyst loading in **(A)** toluene and **(B)** propylene carbonate

The FT-IR spectra of the CMP networks synthesised with excess catalyst in toluene and propylene carbonate, respectively, with different core and co-monomer-to-linker ratios indicate that the synthesis of these polymers were successful. As can be seen in Figure 28, the samples exhibit similar spectra to the control CMP shown in Figure 16. The spectra show that the peaks at ~3377 and 3301 cm^{-1} from the linker (origination from the stretching vibration of the primary amine) are absent or strongly attenuated. This means that the amine groups of the linker have all or mostly participated in the coupling reaction to form the porous networks. Also, it can be said that primary amines are replaced with secondary amine fragments owing to the shift in the bands from 1630 to 1645 cm^{-1}. The peaks that belong to the aromatic C-Br from TBPA (observed at 1005 and 1075 cm^{-1}), from BP (at 1062 and 1086 cm^{-1}), and from TP (at 1008 and 1073 cm^{-1}) are also absent or strongly attenuated, indicating that the bromide groups have all been eliminated to form C-N bonds in successful BH coupling reactions. The two bands at 1499 and 1589 cm^{-1} are related, respectively, to the

stretching of B-type (benzenoid-type, N-B-N,) and Q-type (quinoid-type, N=Q=N) bonds. The bending band at 820 cm^{-1}, which was present in the spectra of all samples as seen in Figure 23, indicate the -CH- of substituted benzene.

3.3.3. UV-Vis-NIR Investigations

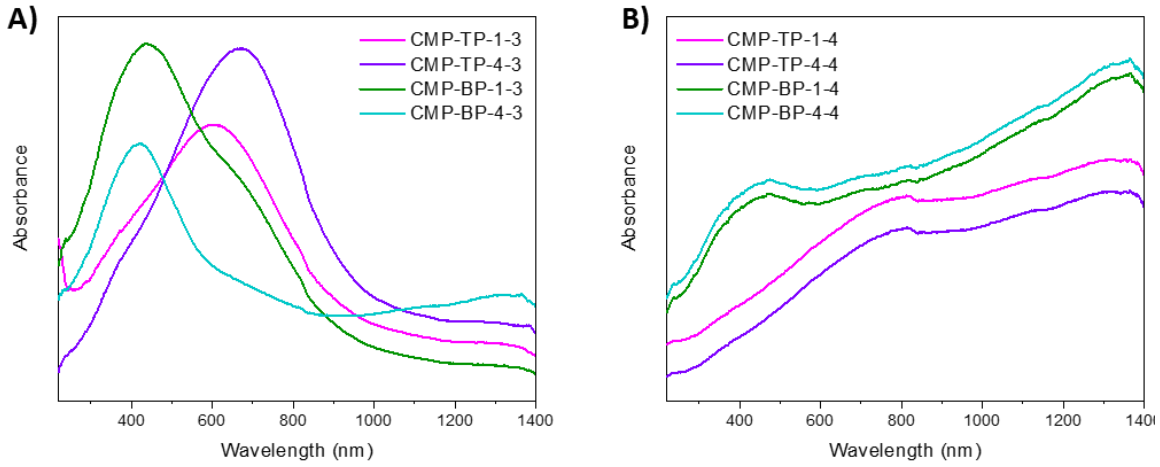

Figure 29 UV-Vis-NIR spectrum of reactions with excess of catalyst loading in **(A)** toluene **(B)** propylene carbonate

Solid-state UV-Vis-NIR spectra of CMPs synthesised with excess of catalyst loading in toluene and propylene carbonate shown in Figure 29 mostly exhibited one bathochromically shifted peak (from 650 nm to 700 nm and 380 nm to 420 nm for respectively CMP-TPs and CMP-BPs synthesised in toluene, and from 650 nm to 790 nm and 380 nm to 440 nm for respectively CMP-TPs and CMP-BPs synthesised in propylene carbonate), when compared with the first synthesised CMPs.

As can be seen in Figure 29A, the CMP-TPs synthesised in toluene exhibit only one band around 700 nm that can be attributed to the π–π* transition of quinoid rings, while the CMP-BPs synthesised in toluene exhibit only one band around 420 nm that can be attributed to the π–π* transition of benzenoid rings

As for the results of CMPs synthesised in propylene carbonate, the materials could be conductive as hinted at by the broad absorbance, which is referred to as a free carrier tail, at wavelengths longer than 800 nm. As the conjugation extends, the bands shift to broader wavelengths and gets larger. In Figure 29B, two characteristic absorption bands at 440 nm of CMP-BP and 750 nm of CMP-TPs shows the π–π* transition of benzenoid rings and

quinoid rings, respectively. These results confirm the creation of extended conjugated networks with amine linkages.

3.3.4. SEM/EDX Investigations

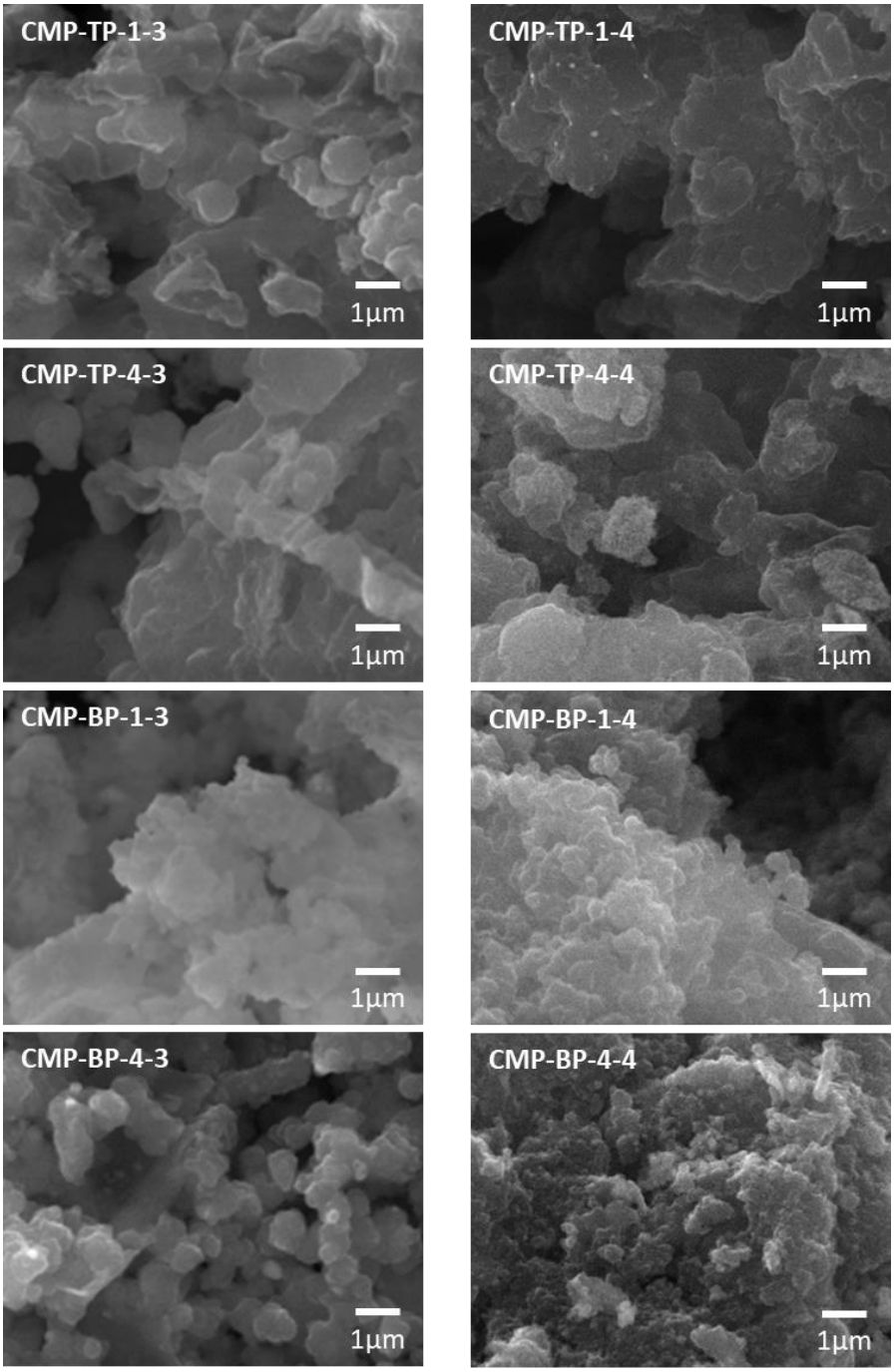

Figure 30 SEM images of CMP-TP and CMP-BP samples at different core-to-linker ratios synthesised with excess catalyst loading in toluene and propylene carbonate

In Figure 30, the SEM images of the materials synthesised with excess catalyst loading in toluene and propylene carbonate were taken to investigate their morphology. The images displayed valuable information in porosity studies according on the degree of aggregation and nanoparticles shapes. These SEM images (Figure 30) show highly aggregated amorphous spherical nanoparticles, with sizes ranging from 1 μm to much smaller particles, different from previously synthesised CMPs (Figure 19 and Figure 25). As can be seen in Figure 30, the addition of excess catalyst loading resulted with a difference in the morphologies, where some of the materials images indicate (e.g. CMP-BP-4-4) much smaller particles.

In addition, to understand the cause of the unknown crystalline peaks (Figure 26), the morphology and elemental composition were determined with SEM-EDX analyses to obtain the percentage of elements found in the CMP networks. The EDX data shown in Table 13 and 14 shows that palladium is present in the materials, along with bromide and caesium in all, and sodium and oxygen absent in some TP samples. The reason for the presence of sodium and oxygen in some samples comes from the starting materials, which decreases as the molar ratio of TP and BP increases. This decrease points out that there could be an interaction between the sodium and oxygen, and nitrogen moieties. The unexpected elements, such as Br, Pd and Cs, observed in the samples are most probably trapped in the porous materials, causing the presence of crystalline peaks in the powder X-ray diffraction results.

Table 13 EDX results for CMPs synthesised with excess of catalyst loading in toluene

Element	CMP-TP-1-3	CMP-TP-4-3	CMP-BP-1-3	CMP-BP-4-3
C	86.0	85.4	89.4	89.8
N	10.9	12.2	8.3	7.2
Br	0.8	0.9	0.6	0.6
Pd	1.3	1.4	1.0	1.4
Na	---	---	---	---
Cs	0.2	0.1	0.1	0.3
O	---	---	0.6	0.3

Table 14 EDX results for CMPs synthesised with excess of catalyst loading in propylene carbonate

Element	CMP-TP-1-4	CMP-TP-4-4	CMP-BP-1-4	CMP-BP-4-4
C	87.6	89.2	91.6	90.9
N	8.7	7.0	5.9	6.4
Br	0.3	0.6	0.2	0.3
Pd	1.1	1.2	1.1	1.3
Na	0.1	0.1	0.1	0.1
Cs	0.1	0.2	0.1	0.1
O	2.1	1.7	0.9	0.8

3.4. Metal Binding Studies

To explore the effects of binding metal ions, the CMP networks were synthesised by two different methods: Route 1 is by the direct Buchwald-Hartwig cross-coupling of tris(4-bromophenyl)amine, p-phenylenediamine and metal-complexed co-monomer (formed with metal salt + pyridine derivative), while Route 2 is by treating the bipyridine or terpyridine-functionalized CMPs with a metal ion post-synthesis. These methods could be portrayed as direct metal incorporation by copolymerization and post-synthetic metalation, respectively.[69] In Route 1, the synthesis with copper resulted in no isolable material, meaning that the cross-coupling reaction did not proceed. It is deemed that the pyridine units could not coordinate with copper(II) under the reaction conditions used, such as temperature, solvent, reaction time or ratio. On the other hand, the synthesis by Route 1 with cobalt resulted in low but enough yield to characterize the resulting material. Contrary to the first route, synthesis with Route 2 resulted in very high yields, both with copper and cobalt salts.

3.4.1. XRD Investigations

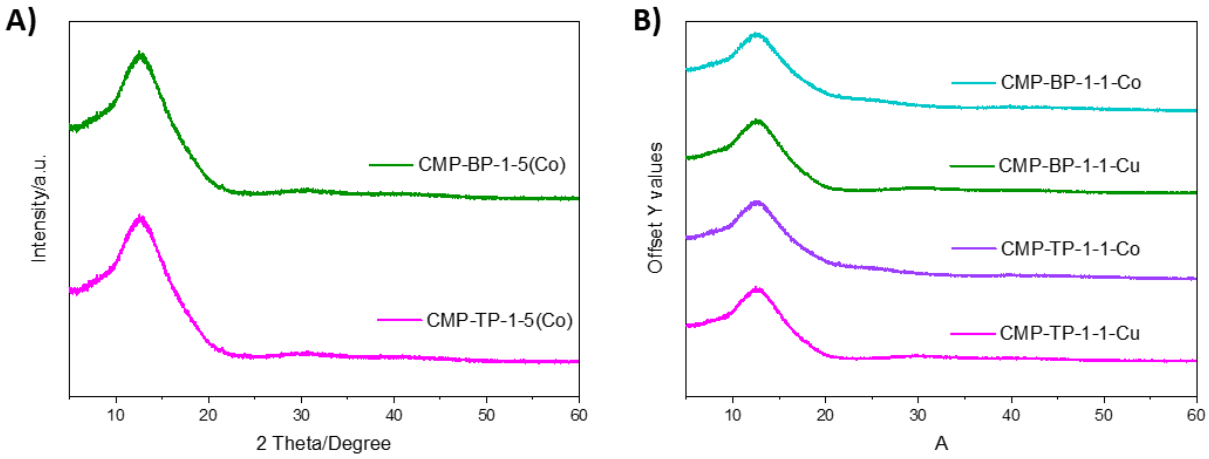

Figure 31 X-ray diffraction patterns samples from reactions of metal-containing CMPs synthesised by **(A)** Route 1 and **(B)** Route 2

The powder X-ray diffraction (Figure 31) determined from the metal-containing CMPs synthesised by Route 1 (with cobalt) and Route 2 also demonstrates broad peaks at approximately 2Θ = 10-15°. It can therefore be declared that new amorphous materials, have been synthesised. Also, there are no crystalline peaks, meaning that there are no impurities from the starting materials, any by-products formed during the synthesis, or, importantly, from any metal salts.

3.4.2. FT-IR Investigations

The FT-IR spectra of the metal-containing CMPs synthesised in propylene carbonate shown in Figure 32 indicate that the synthesis of these polymers was successful. The spectra show that the peaks at ~3377 and 3301 cm^{-1} from the linker owing to the stretching vibration of the primary amine are absent or strongly attenuated. This means that the amine groups of the linker have all or mostly participated in the coupling reaction to form the porous networks. Also, it can be said that primary amines are exchange by secondary amine fragment owing to the shift in the bands from 1630 to 1645 cm^{-1}. The peaks that belong to the aromatic C-Br from TBPA which were observed at 1005 and 1075 cm^{-1}, from BP at 1062 and 1086 cm^{-1}, and from TP at 1008 and 1073 cm^{-1} are also absent or strongly attenuated. The two bands at 1499 and 1589 cm^{-1} are related, respectively, to the stretching of B-type (benzenoid-type, N-B-N,) and Q-type (quinoid-type, N=Q=N) bonds. In all instances, the low

intensity bands observed in the region of 600–500 cm^{-1} attribute to metal-nitrogen bending vibrations.

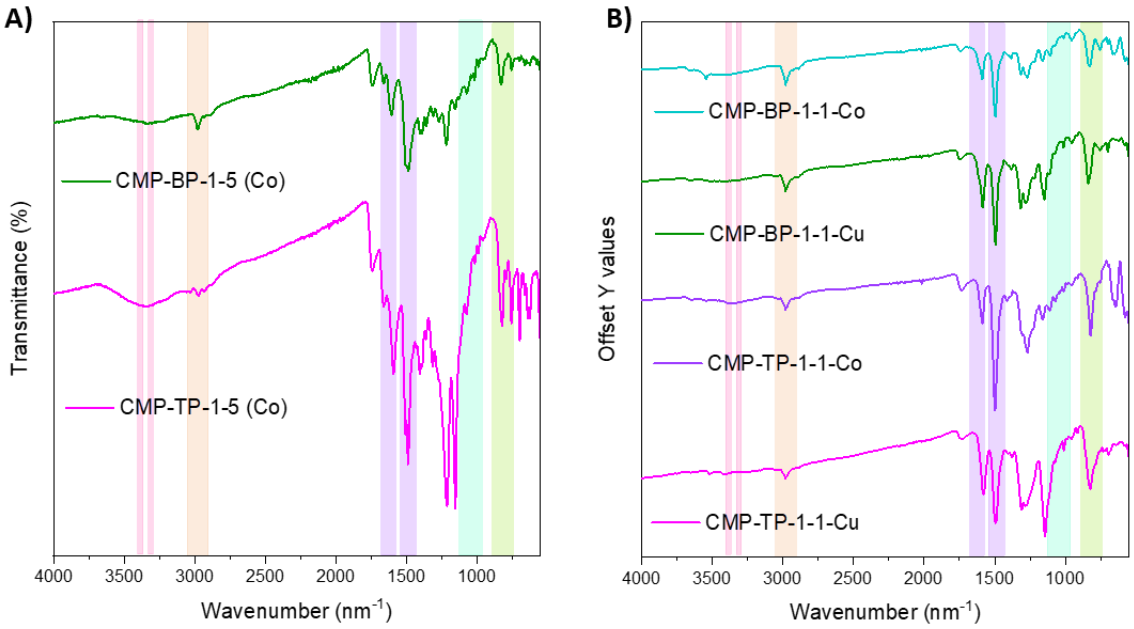

Figure 32 FT-IR spectra of metal-containing CMPs synthesised by **(A)** Route 1 and **(B)** Route 2

Also, metal-containing CMPs synthesised by direct metal incorporation (Route 1) showed a broad peak around 3700 - 3200 cm^{-1}. This broad peak is attributed to O-H stretching of the solvent (water or methanol) used for washing which indicates that the sample were not entirely dry before the FT-IR measurements.

3.4.3. UV-Vis-NIR Investigations

Solid-state UV-Vis-NIR spectra of metal-containing CMPs synthesised shown in Figure 33 mostly exhibited one peak, which are different from the control CMP as can be seen. The metal-containing systems show bathochromically shifted absorbance, which provided strong evidence of the metal-coordination interaction mechanism. According to results of CMPs synthesised by Route 1 with cobalt and by Route 2 with copper could be conductive due to broad absorbance, which are referred to as a free carrier tail, at wave lengths greater than about 800 nm. As the conjugation extends, the transitions from the bands shift to longer wavelengths, as the band gap gets larger. These results confirm the creation of extended conjugated networks with amine linkages and metal coordination.

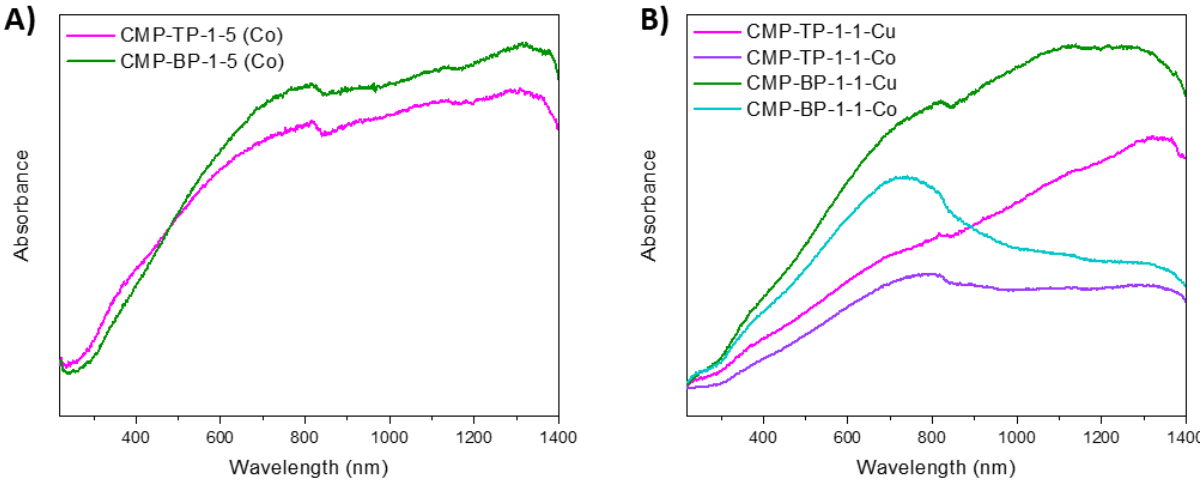

Figure 33 Solid-state UV-Vis-NIR spectra of metal containing CMPs synthesised by **(A)** direct metal incorporation and **(B)** post-synthetic metalation

Solid-state UV-Vis-NIR spectra of metal-containing CMPs synthesised shown in Figure 33 mostly exhibited one peak, which are different from the control CMP as can be seen. The metal-containing systems show bathochromically shifted absorbance, which provided strong evidence of the metal-coordination interaction mechanism as a result of metal-to-ligand charge transfer.

According to results of CMPs synthesised by Route 1 with cobalt and by Route 2 with copper could be conductive due to broad absorbance, which are referred to as a free carrier tail, at wave lengths greater than about 800 nm. As the conjugation extends, the transitions from the bands shift to longer wavelengths, as the band gap gets larger. These results confirm the creation of extended conjugated networks with amine linkages and metal coordination.

3.5. Gas Sorption Studies

The physical adsorption of gas molecules on a solid surface serves as the basis of an important analysis technique for the measurement of the surface area of materials. The surface areas and pore size distributions of the polymers were measured by N_2 adsorption and desorption at 77 K. CO_2 uptake measurements were taken at both 0°C (273.15 K) and room temperature (298.15 K).

3.5.1. Gas Sorption Studies of CMPs

In order to increase surface area and CO_2 uptake capacity, terpyridine and bipyridine building blocks were incorporated into the PTPA framework separately, and the effect of varying the ratios have been investigated. According to the IUPAC classification, both CMP-TPs and CMP-BPs show type IV sorption isotherms. The isotherms exhibit a continuous linear increase in adsorption, which occurs owing to the mesoporous adsorbent. Because of adsorbed gas involved with macrostructure and unfilled voids, a steep increase is observed after 0.9 relative pressure. In amorphous materials particularly, the cause of differentiation between adsorption and desorption curves is most probably due to blocked and narrow pores that cause difficulties for the gas molecules to enter (or leave).

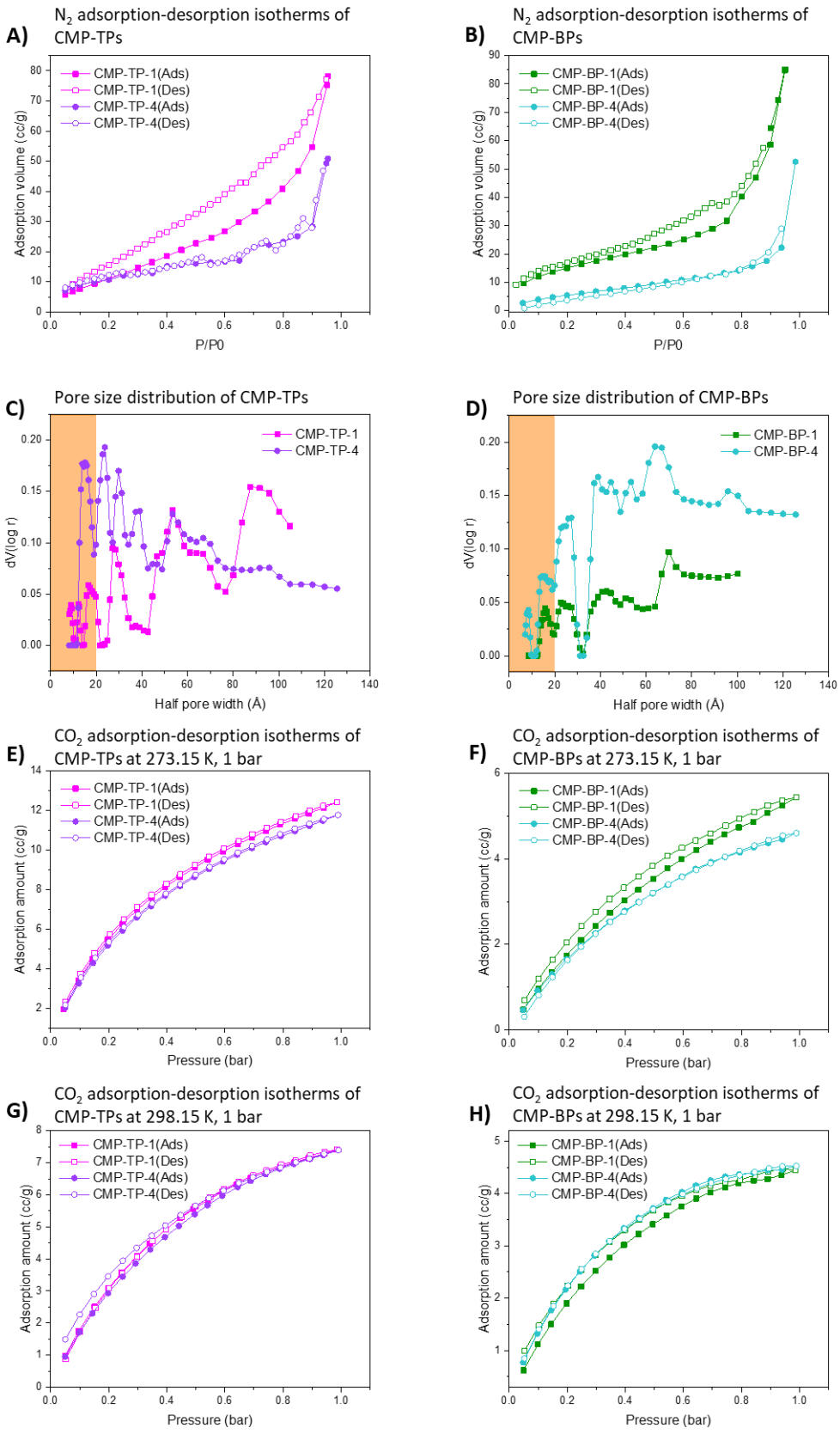

Figure 34 **(A)** and **(B)** N_2 isotherms at 77 K **(C)** and **(D)** present the PSD obtained from the N_2 isotherms via NLDFT (based on a slit-pore model). **(E)** and **(F)** CO_2 isotherms at 273.15 K, 1 bar. **(G)** and **(H)** CO_2 isotherms at 298.15 K, 1 bar for CMP-TP and CMP-BP, respectively.

As can be seen in N_2 isotherms of the polymers (Figure 34 **A** and **B**), the volume of adsorbed N_2 gas has decreased as the ratio of the pyridine units increased in both CMP-TPs and CMP-BPs. The interaction between the N_2 molecule and the material's surface functionality can shift the pore filling pressure, leading to inaccuracies in pore size calculation. In addition, the possibility of different orientations of the N_2 molecule on the surface of polar materials leads to uncertainty in the cross sectional area used for BET surface area calculations. Per IUPAC, this uncertainty in the assumed cross-sectional area can result in a reported N_2 BET surface area which differs from the true surface area of the material. As mentioned in Table 15, the surface area has also decreased. The reason for the surface area to decrease could be on account of excess of amine groups leading to weakening the networks and also changing the pore sizes to extend from micropores to mesopores or even macropores. The extension of pore sizes can be confirmed with the PSD (Figure 34 **C** and **D**).

Table 15 Surface area, porosity properties and CO_2 uptake obtained from N_2 isotherms at 77 K and CO_2 isotherms at 273.15 K and 298.15 K

Polymer Code	S_{BET}	Pore Volume	CO_2 uptake at 1 bar, [wt%]	
	(m^2/g)	(cm^3/g)	273 K	298 K
PTPA*	52	0.07	3.7	-
CMP-TP-1	49	0.114	2.4	1.5
CMP-TP-4	41	0.077	2.3	1.4
CMP-BP-1	75	0.125	1.1	0.9
CMP-BP-4	69	0.068	0.9	0.9

**The PTPA sample previously was reported by the Faul research group.[61]*

As noted in Table 15, the BET surface area of CMP-BPs is higher than both CMP-TPs and PTPA. The particular reason for the circumstance could be owing to the presence of two bromide extensions in the bipyridine derivative used. Thus, extension continues from both sides of the co-monomer allowing more nitrogen to be added into the polymer. This

circumstance is different for the single bromide-containing terpyridine derivative, where it is blocking one end of the growing polymer network.

In addition, to extract additional knowledge about the porosity properties of the polymers synthesised, CO_2 uptake at 0°C (273.15 K) (Figure 34 **E** and **F**) and room temperature (298.15 K) were also measured, results also shown in Table 15. Although the surface areas of the CMP-TPs are less than the CMP-BPs, their CO_2 uptakes are twice as high. This situation can be reconciled with the materials containing higher amine content and micropore proportion, where CMP-BPs include more mesopores than CMP-TPs.

3.5.2. The Effect of Solvent on Porosity and CO_2 Uptake

According to research, by a logical solvent choice, the porosity of materials can be increased.[140, 141] For the purpose of increasing the surface area and CO_2 uptake, HSP studies have been undertaken. From the calculations, propylene carbonate, ethanol and DMSO were chosen to be used as optimal solvents for the synthesis. It has been mentioned in Section 3.2.1 that the synthesis with DMSO and ethanol was unsuccessful, since the yields were less than 9%.

To illustrate how the chosen solvent affects the porosity, the surface areas and pore size distributions of the polymers were measured by N_2 adsorption and desorption at 77 K. CO_2 uptake measurements were recorded at both 0°C (273.15 K) and room temperature (298.15 K).

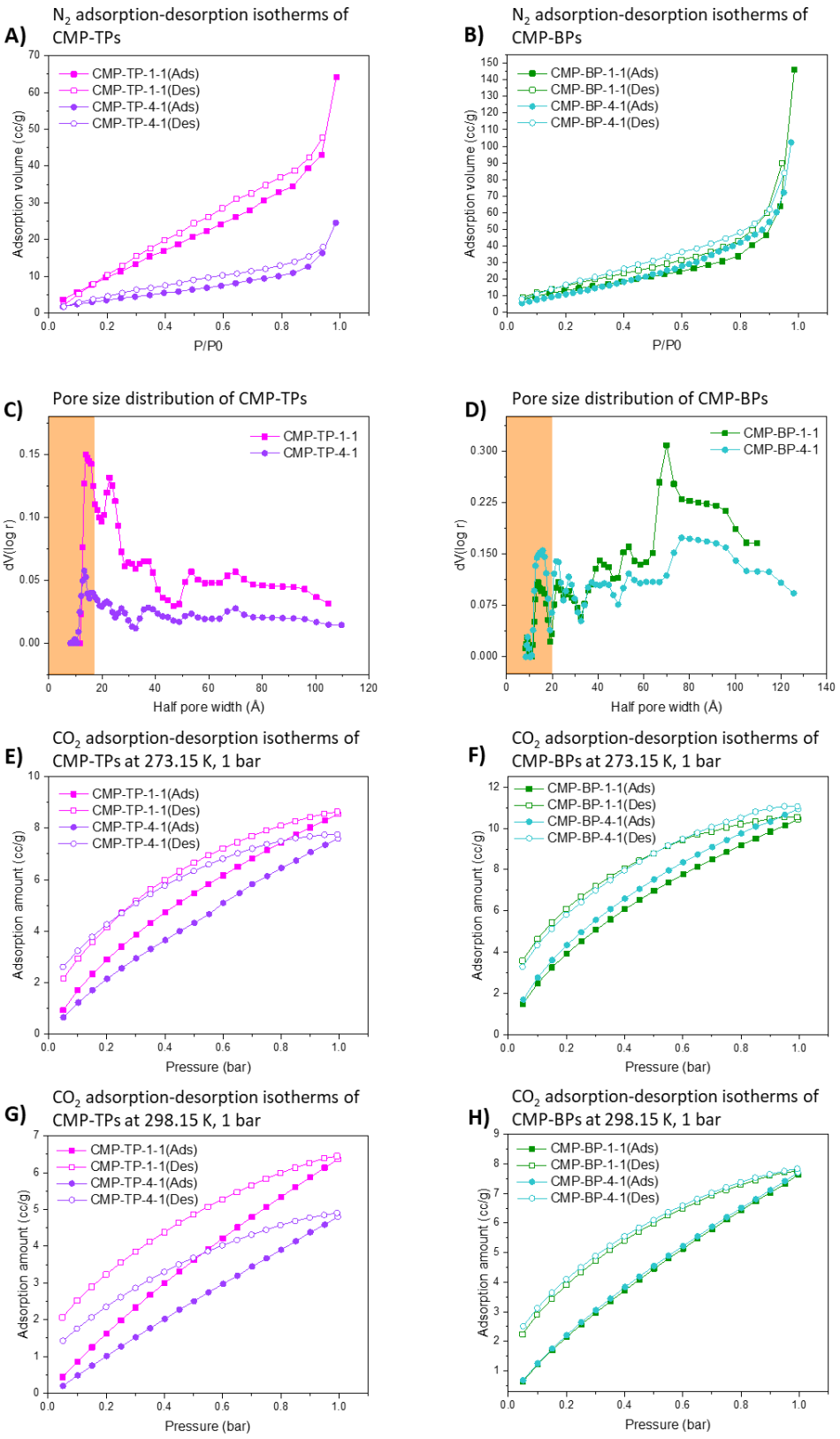

Figure 35 **(A)** and **(B)** N_2 isotherms at 77 K **(C)** and **(D)** present the PSD obtained from the N_2 isotherms via NLDFT (based on a slit-pore model). **(E)** and **(F)** CO_2 isotherms at 273.15 K, 1 bar. **(G)** and **(H)** CO_2 isotherms at 298.15 K, 1 bar for CMP-TPs and CMP-BPs synthesised with propylene carbonate.

HSP studies were used to choose a suitable solvent for the synthesis of CMPs to optimize their yield and surface area. However, as listed in Table 16, the results of the surface areas synthesised in propylene carbonate indicate that they have significantly decreased in comparison to the materials synthesised in toluene. According to the IUPAC classification, both CMP-TPs and CMP-BPs synthesised in propylene carbonate show a type IV isotherm N_2 sorption isotherms, similar to the CMPs synthesised in toluene, which occurs owing to their mesopores property. As in the previous materials, N_2 isotherms of the polymers (Figure 35 **A** and **B**), the volume of adsorbed N_2 gas decreased as the ratio of the pyridine unit increased in both CMP-TPs and CMP-BPs.

According to the PSD results, CMP-TPs synthesised with toluene mostly contain mesopores. By changing the reaction solvent to propylene carbonate, the PSD has narrowed to mostly micropores. However, CMP-TPs synthesised with propylene carbonate show similar PSDs to the ones synthesised with toluene.

In addition, to extract additional knowledge about the porosity properties of the polymers synthesised, CO_2 uptake at 0°C (273.15 K) (Figure 35 **E** and **F**) and room temperature (298.15 K) were also measured (results shown in Table 16). The CO_2 uptake of CMP-TPs decreased to 1.7 wt% from 2.4 wt% in 0°C, while for CMP-BPs it increased twice as high (from 1.1 wt% to 2.2 wt%).

Table 16 Surface area, porosity properties and CO_2 uptake obtained from N_2 isotherms at 77 K and CO_2 isotherms at 273.15 K and 298.15 K of materials synthesized with propylene carbonate (after HSPs studies)

Polymer Code	S_{BET}	Pore Volume	CO_2 uptake at 1 bar, [wt%]	
	(m^2/g)	(cm^3/g)	273 K	298 K
CMP-TP-1-1	40	0.088	1.7	1.3
CMP-TP-4-1	14	0.032	1.5	1.0
CMP-BP-1-1	50	0.129	2.2	1.5
CMP-BP-4-1	42	0.122	2.2	1.5

The difference of the Hansen solubility parameter ($|\Delta\delta_T|$) between propylene carbonate and CMP-TPs and CMP-BPs was less than 1, suggesting that the solvent was good for the synthesis. Consequently, solvents with good compatibilities with the polymer networks could contribute to phase separation at a much later stage during the polymerization, thus affording better control and thus producing a polymer with larger surface area and narrower PSD.[142-144] Although propylene carbonate seems to be optimal for the synthesis by the outcome of HSPs calculations, the results mostly show the opposite. The reason for these results to occur could be due to the polymer chains not growing, thus resulting to form oligomers other than polymers in the whole structure. It is believed that the terpyridine and bipyridine units could be forming a complex with the palladium catalyst and not leaving enough catalyst for the cross-coupling reaction to occur.

The surface area and CO_2 uptake results obtained of the pyridine-based CMPs synthesised in this study (surface area ~40-230 m^2/g, CO_2 uptake ~1.1-5.7 wt% at 0°C) are much lower than those of other CMPs reported in the literature with values of 873 m^2/g and 1003 m^2/g specific surface area, and 106 mg/g and 136 mg/g (~10.9-13.7 wt% at 0°C).[145] Further studies need to be taken in order to increase their properties (surface area and CO_2 uptake capacity).

3.5.3. The Effect of Higher Catalyst Loading

As mentioned in **Section 3.5.2**, propylene carbonate did not result in the expected increase of the surface area and lowering of the PSD of the polymer networks. It is believed that the terpyridine and bipyridine units could be forming a complex with the palladium catalyst and not leaving enough catalyst for the cross-coupling reaction to occur. For this purpose, the quantity of catalyst and ligand was increased by a factor of 10 to ensure the catalyst participated in the cross-coupling reaction. The addition of more catalyst led to increase the yield of the synthesised materials, 3 times for the materials synthesised with propylene carbonate. This approach could result in chain-growth of the polymer and improve the reaction yields, CO_2 uptake capacity and increasing the surface area.

N_2 adsorption and desorption at 77 K and CO_2 uptake measurements taken at both 0°C (273.15 K) and room temperature (298.15 K) for CMPs with 0.1:0.9 ratio of pyridine derivative:TBPA are shown in Figure 36.

As can be seen in the N_2 isotherms of both CMP-TPs and CMP-BPs polymers (Figure 36 **A** and **B**), the volume of adsorbed N_2 gas is lower for the materials synthesised in propylene carbonate, resulting in low surface area as shown in Table 17, with the surface area further decreased from 40 m^2/g to 18 m^2/g with the addition of more catalyst. The CO_2 uptake (Figure 36 **E** and **F**) of the materials did not change significantly.

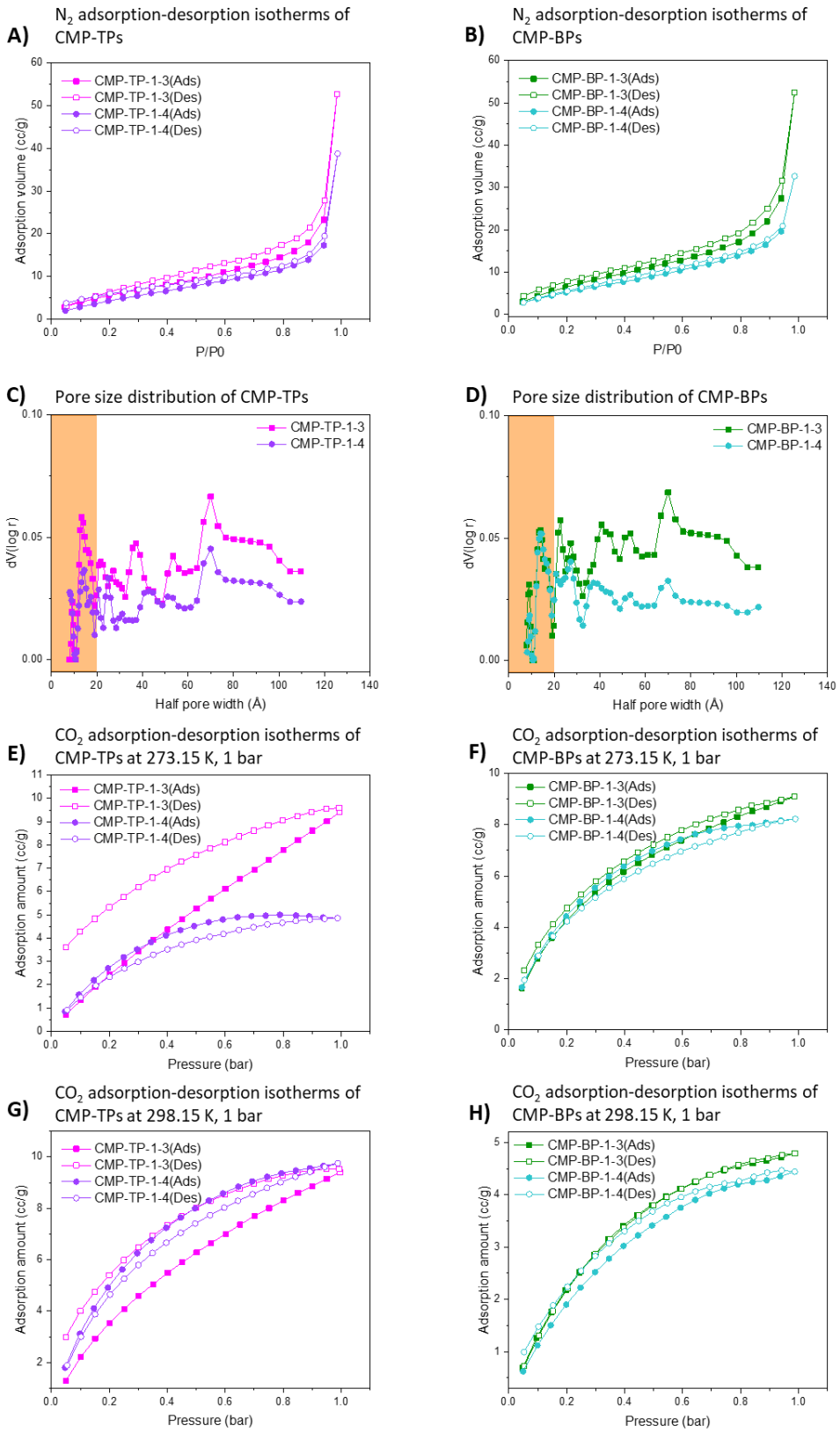

Figure 36 **(A)** and **(B)** N_2 isotherms at 77 K **(C)** and **(D)** present the PSD obtained from the N_2 isotherms via NLDFT (based on a slit-pore model). **(E)** and **(F)** CO_2 isotherms at 273.15 K, 1 bar. **(G)** and **(H)** CO_2 isotherms at 298.15 K, 1 bar for CMP-TPs and CMP-BPs synthesised with more catalyst

Although HSPs studies predicted that propylene carbonate is a compatible solvent for the synthesis, it was seen from research and results that propylene carbonate did not yield the expected results. Further studies, such as adjusting or changing the reaction conditions (temperature, reaction time, catalyst), are required in order to explore their influence in the synthesis.

Table 17 Surface area, porosity properties and CO_2 uptake obtained from N_2 isotherms at 77 K and CO_2 isotherms at 273.15 K and 298.15 K of materials synthesized with more catalyst

Polymer Code	Solvent	S_{BET}	Pore Volume	CO_2 uptake at 1 bar, [wt%]	
		(m^2/g)	(cm^3/g)	273 K	298 K
CMP-TP-1-3	Toluene	22	0.041	1.9	1.8
CMP-TP-4-3		15	0.021	1.1	0.6
CMP-BP-1-3		27	0.046	1.8	0.9
CMP-BP-4-3		19	0.031	1.7	1.3
CMP-TP-1-4	Propylene carbonate	18	0.035	1.9	1.0
CMP-TP-4-4		12	0.019	1.4	0.8
CMP-BP-1-4		21	0.031	1.6	0.9
CMP-BP-4-4		18	0.017	1.7	1.0

3.5.4. The Effect of Metal Doping

As mentioned in **Section 1.2.3,** page 7, studies have shown that modifications of porous organic polymers by inserting metal sites into their framework could improve their gas uptake properties and catalytic activity. Metal-inserted CMPs could also be useful as heterogeneous catalysts, where the combination of active metal species and high surface areas would be beneficial.[69] For this particular reason the effects on porosity features were evaluated.

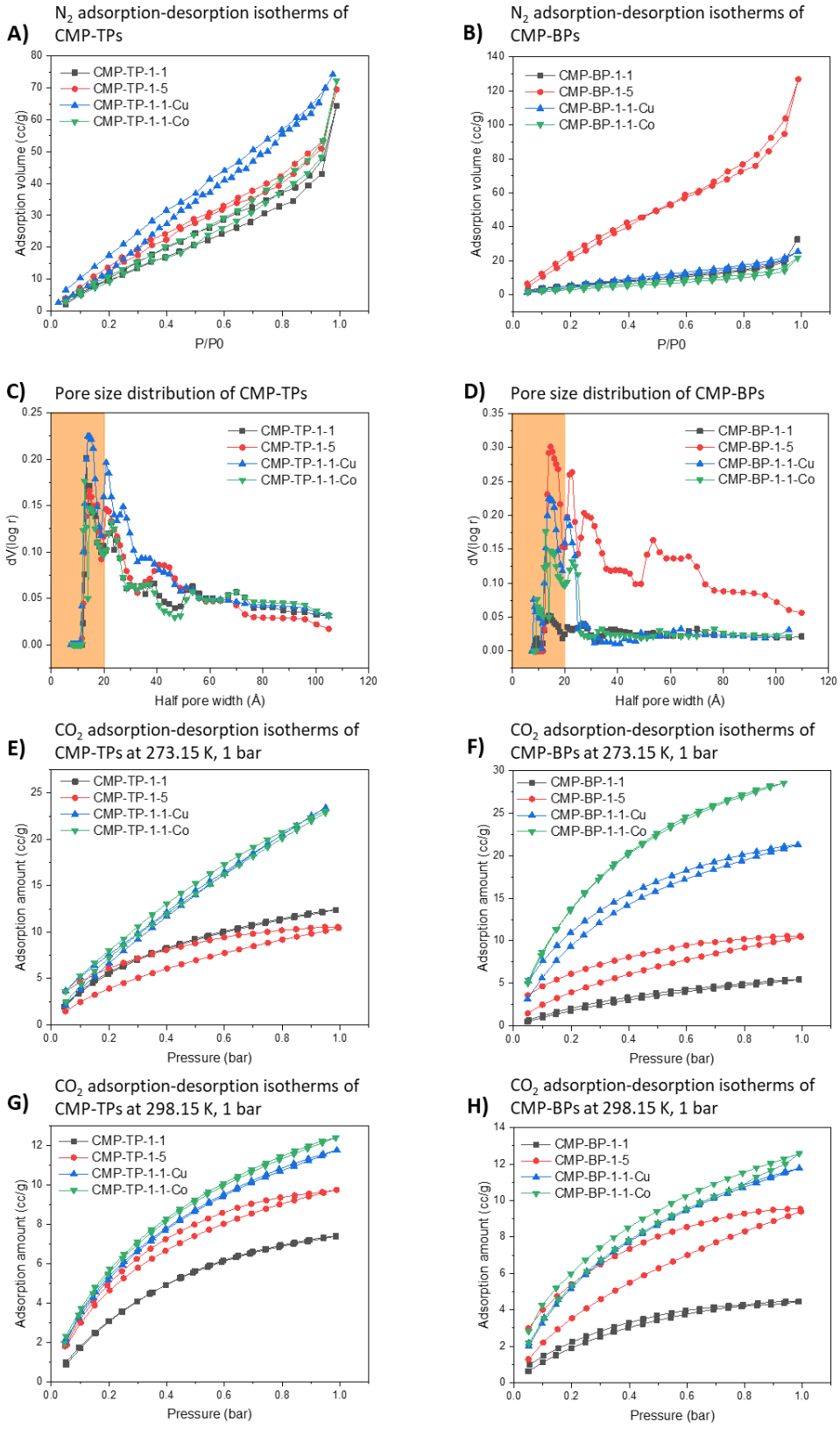

Figure 37 **(A)** and **(B)** N_2 isotherms at 77 K **(C)** and **(D)** present the PSD obtained from the N_2 isotherms via NLDFT (based on a slit-pore model). **(E)** and **(F)** CO_2 isotherms at 273.15 K, 1 bar. **(G)** and **(H)** CO_2 isotherms at 298.15 K, 1 bar for CMP-TPs and CMP-BPs synthesised with metal salts

According to the IUPAC classification, metal-containing CMPs mostly show type IV N_2 sorption isotherms (Figure 37 **A** and **B**). The isotherms exhibited a continuous linear increase in adsorption, which occurs owing to the PSD mostly showing mesopores. On account of adsorbed gas interacting with the macrostructure and unfilled voids, a steep increase is observed after 0.9 relative pressure. In amorphous materials particularly, the cause of differentiation between adsorption and desorption curves is most probably due to blocked and narrow pores causing difficulties for access of gas molecules. Other than that, CMP-TP-1-1-Cu shows a type III isotherm N_2 sorption isotherm, which is found when adsorbent-adsorbate interactions are weak for nonporous or macroporous materials (pore size >50nm) materials. According to the N_2 isotherms of the polymers (Figure 37 **A** and **B**), while the volume of adsorbed N_2 gas (and thus the surface area) has not changed for most CMPs, it rapidly increased for CMP-BP synthesised by the direct Buchwald-Hartwig cross-coupling in the presence of cobalt (to 229 m^2/g).

Table 18 Surface area, porosity properties and CO_2 uptake obtained from N_2 isotherms at 77 K and CO_2 isotherms at 273.15 K and 298.15 of materials synthesized with metal salts

Polymer Code	S_{BET}	Pore Volume	CO_2 uptake at 1 bar, [wt%]	
	(m^2/g)	(cm^3/g)	273 K	298 K
CMP-TP-1-5	107	0.078	2.1	1.8
CMP-BP-1-5	229	0.1815	2.1	1.8
CMP-TP-1-1-Cu	163	0.102	4.6	2.5
CMP-TP-1-1-Co	110	0.081	4.5	2.4
CMP-BP-1-1-Cu	204	0.173	4.2	2.5
CMP-BP-1-1-Co	122	0.1104	5.7	2.8

As can be seen in Table 18, the surface area of all materials doped with metal also significantly increased, by at least three times (for example, for CMP-BP-1-1-Cu from 50 to 204 m^2/g). The particular reason for this result could be owing to the molecular

rearrangement by the presence of metals. The metals could be organizing the layout of the molecules and resulting to enlarge the surface area of the materials. Also, the metals may have helped the pores that remained embedded to open up to the surface with the arrangement in molecules. It can also be noted that as the BET surface area increases, so does the micropore volume of the products, which was confirmed with the PSD (Figure 37 **C** and **D**). Further information gathered from the PSD of the polymers: while CMP-TPs show similar results with a little shift to more micropores, CMP-BPs show a larger shift to micropores.

In addition, to extract additional knowledge about the porosity properties of the polymers synthesised, CO_2 uptake at 273.15 K (Figure 37 **E** and **F**) and 298.15 K (Figure 37 **G** and **H**) was also measured, with the results shown in Table 18. Although the surface area of the materials synthesised by Route 1 have increased (for example, for CMP-BP-1-5 from 40 to 229 m^2/g), the CO_2 uptake did not increase at the same rate. On the other hand, it is clear that the CO_2 uptake has massively increased by Route 2 (for example, for CMP-BP-1-1-Co from 2.2 wt% to 5.7 wt% at 0°C).

3.6. CO_2 Reduction Studies

Tuneable active sites within the network of a porous material enhances the heterogeneous catalytic activity. Unlike nonporous materials, porous materials containing nitrogen atoms provide opportunities for the reactant to easily approach the catalytically active site. Furthermore, an important factor that cannot be ignored that makes CMPs convenient catalysts in electrocatalytic CO_2 reduction is their extended π-conjugated system.[146, 147] The extended π-conjugated structure of the polymer provides insolubility of the material in organic electrolytes, resulting in improved cycling stability with a longer cycle life of the materials for electrochemical applications.[148, 149] Moreover, the porosity of the material could ensure ion transportation for catalytic properties.[149] CV is a useful method to study a material's electrochemical behaviour and gain information about their oxidation and reduction potentials.

To investigate the electrochemical and redox properties of the synthesised materials in the presence of CO_2, CV measurements were obtained on a glassy carbon working electrode and

was cycled repeatedly between −1.0 V and +1.0 V vs V_{SCE}, then converted to RHE dependent on the effect of the pH, with the equation given in Section 2.5. The process of CO_2 electrochemical reduction was carried out with 0.1 M $KHCO_3$ as electrolyte at two different pH values (pH of CO_2 saturated electrolyte: 6.81-7.21, pH of argon-saturated electrolyte: 9-9.5) in a two-compartment H-cell with three-electrodes. The electrodes used are: a glassy carbon as the working electrode on which a prepared CMP sample is drop cast (prepared as seen in Figure 8), a calomel electrode as reference electrode, and Pt wire as counter electrode.

To discuss the effects of molecular structure and the change of reaction solvent on the redox properties, the CMP-TPs and CMP-BPs synthesized in toluene were examined first. The voltammograms shown in the Figure 38 are from the CV measurements under CO_2 and argon atmospheres, respectively.

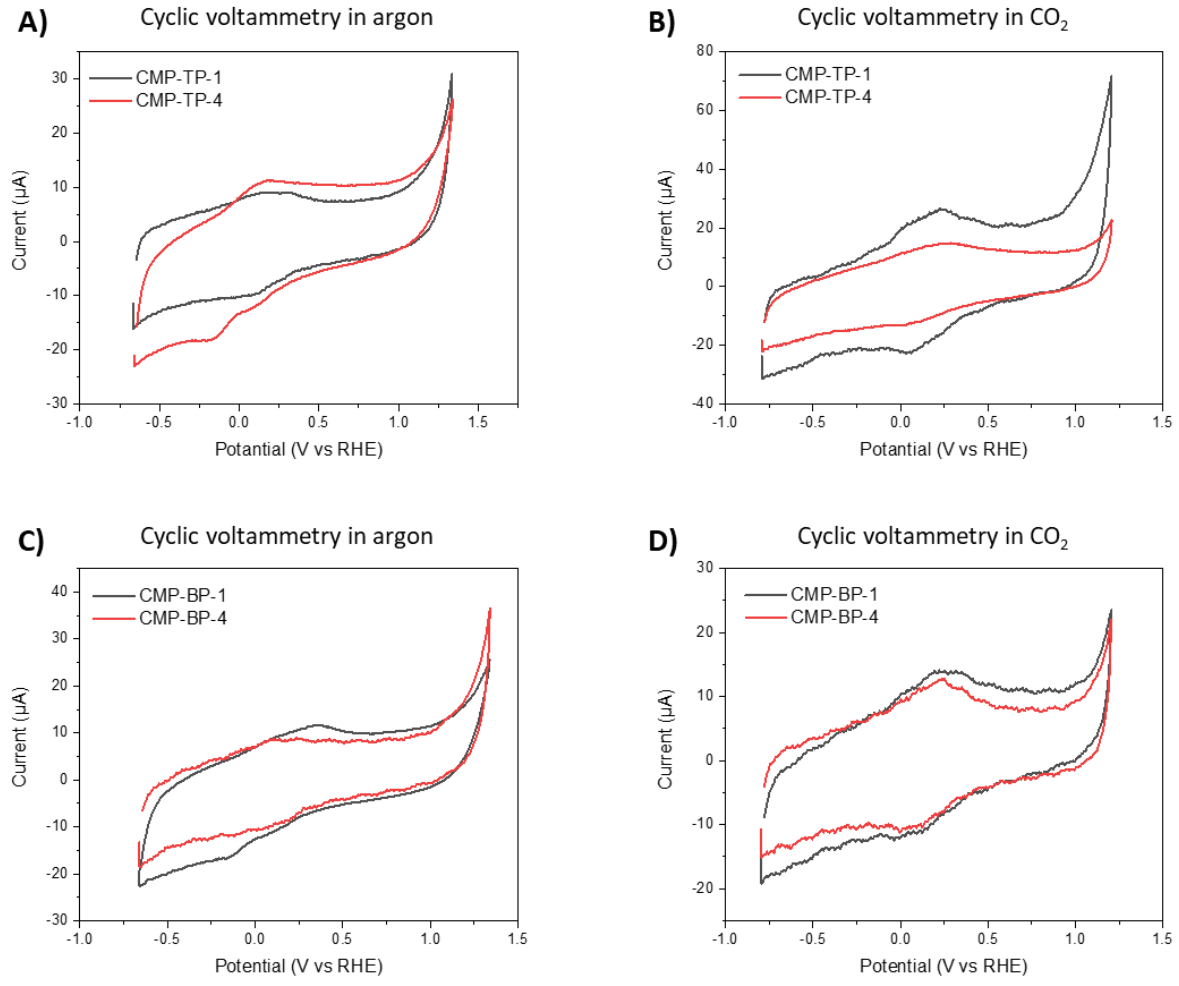

Figure 38 Cyclic voltammograms in **A)** and **C)** argon atmosphere and **B)** and **D)** CO_2 atmosphere of the CMP-TPs and CMP-BPs

As it can be seen in Figure 38, the cyclic voltammograms in both argon and CO_2 atmosphere displays oxidation and reduction peaks for the CMP-TP and CMP-BP networks. In the argon atmosphere, both CMP-TP-1 and CMP-BP-4 on a glassy carbon electrode exhibit a reduction peak at 0.10 V vs V_{RHE}, which is associated with an oxidation peak at 0.25 V vs V_{RHE}. Meanwhile, the results for CMP-TP-4 and CMP-BP-1 exhibited a reduction peak at -0.20 V vs V_{RHE}, which is also associated with an oxidation peak at 0.30 V vs V_{RHE}. In CO_2, the reduction peaks have all shifted 0.10 V vs V_{RHE} to a more positive value. This shift is due to the polymers being reduced while oxidizing the CO_2 that is being bubbled into the system.

This observed effect may also be attributed to the increased delocalization and resonance stabilization in the extended π-conjugated structure of the CMP. In a CO_2 atmosphere the current density for all materials is higher than in argon. Owing to the CO_2 capture properties of the materials, obtaining higher current for a cathode indicates that the CO_2ECR rate is faster. According to the conclusion to be drawn from the CV measurements, it could be said that the CO_2ECR rate of CMP-TP-1 is the highest among all samples with a current of 30 μA at +0.1 V vs V_{RHE}.

In order to investigate the electrochemical properties of the same materials synthesized in propylene carbonate, which was determined to be a suitable solvent for the synthesis by calculation of HSPs, the CV measurements were also taken under CO_2 and argon atmospheres. The voltammograms can be seen in the Figure 39.

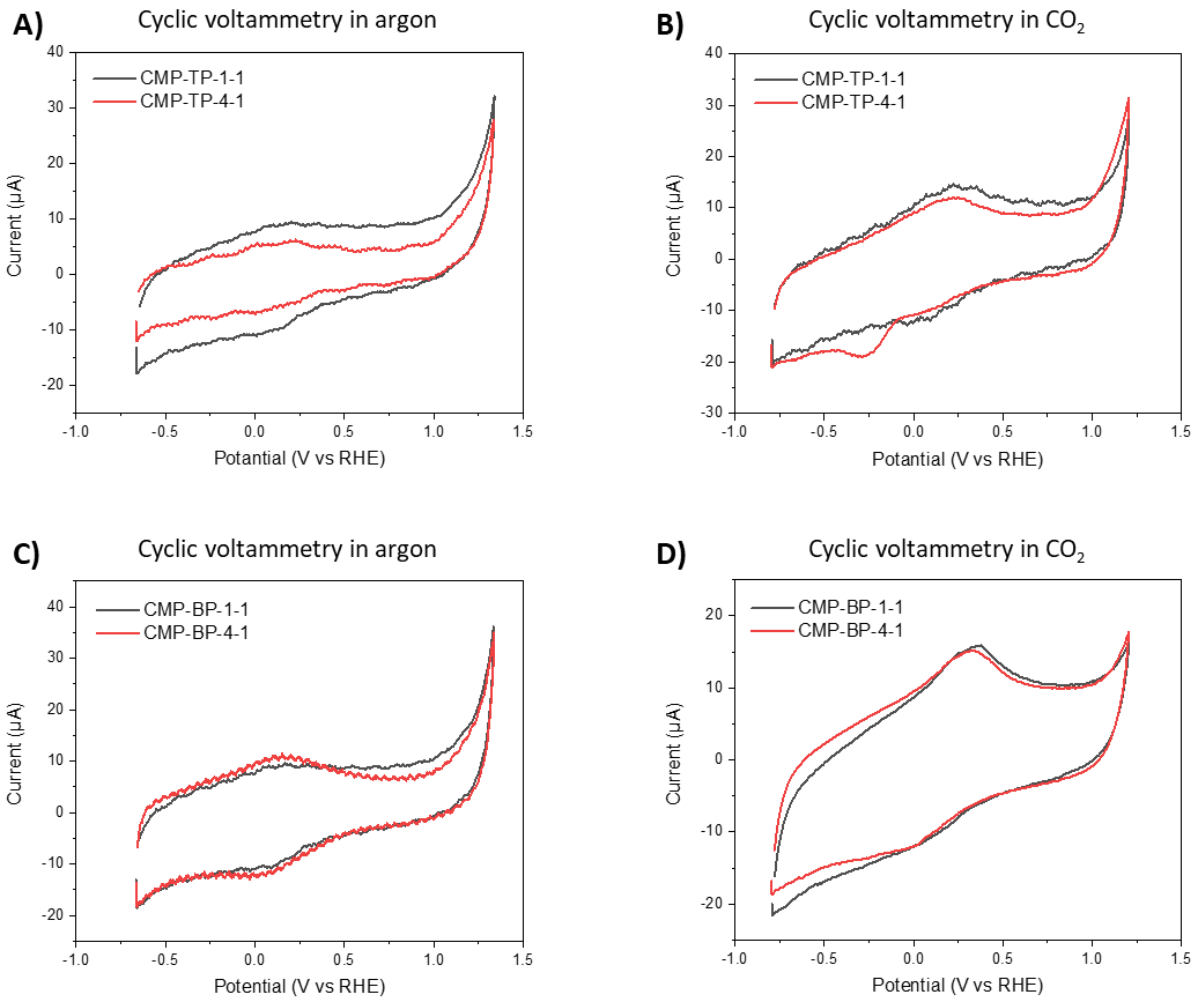

Figure 39 Cyclic voltammograms in **A)** and **C)** argon atmosphere and **B)** and **D)** CO_2 atmosphere of the CMP-TPs and CMP-BPs synthesised in propylene carbonate

The change of solvent to propylene carbonate did not change the potential states of the oxidation and reduction peaks but has led to a slight enhancement in the current a few in CO_2-saturated electrolyte (from 10 to 20 µA for CMP-TPs, and from 10 to 15 µA for CMP-BPs). These higher currents for the oxidation and reduction peak indicate that the materials display stronger responses for the electrochemical reduction of CO_2. This could mean that there is higher concentration of CO_2 at the conversion site, owing to the CO_2 capture property of the polymers.

To also investigate the electrochemical properties of the metal-doped CMPs, the cyclic voltammograms under CO_2 and argon atmospheres were also measured the curves can be seen in Figure 40.

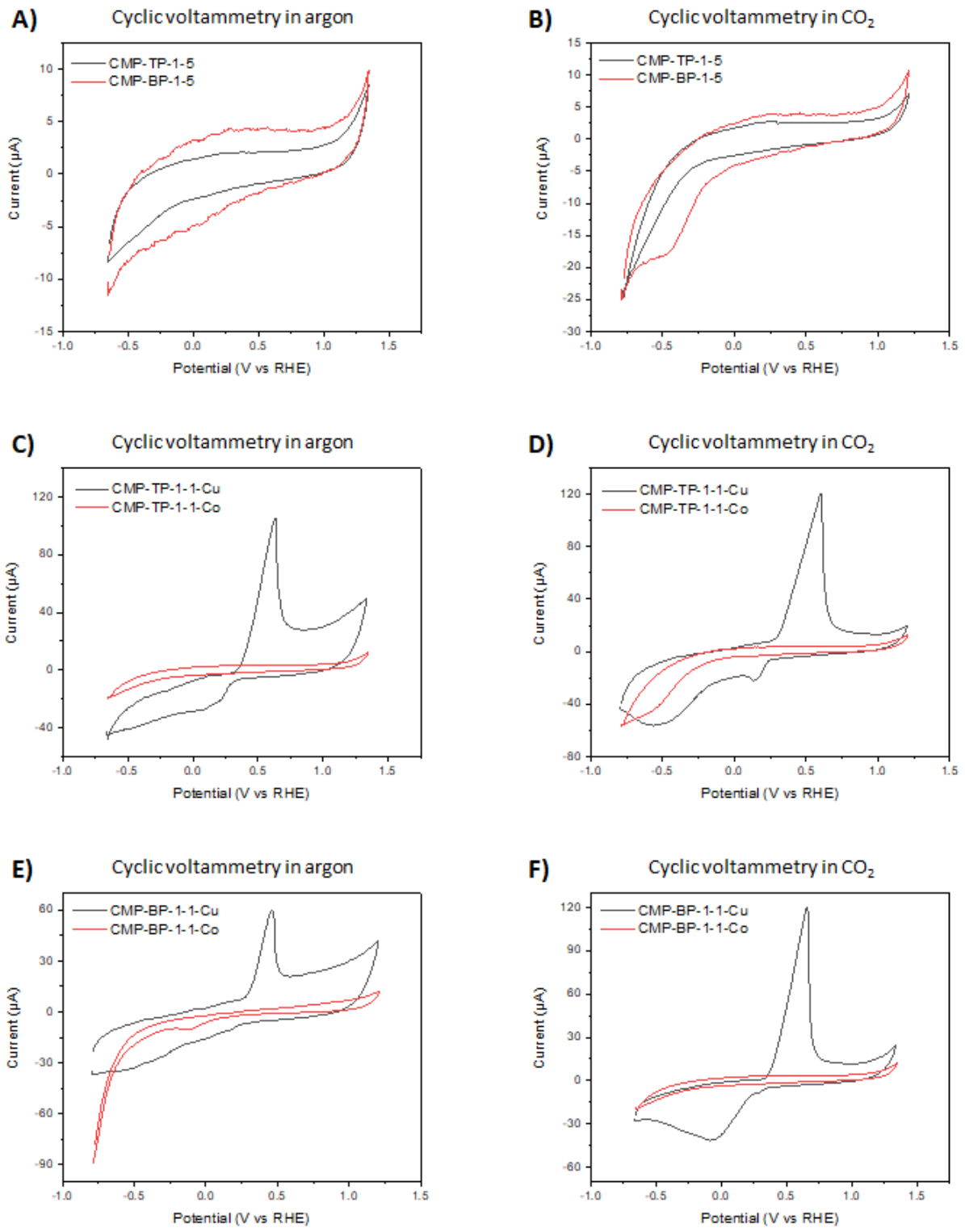

Figure 40 Cyclic voltammograms in **A), C)** and **E)** in argon atmosphere and **B), D)** and **F)** in CO_2 atmosphere of metal-doped CMP-TPs and CMP-BPs

The CV curves for the metal-inserted CMPs synthesised by Route 1 and Route 2 with cobalt both show no redox peaks as seen in the voltammograms in Figure 41 **(A)** and **(B)**. The absence of redox peaks could mean that the coordination with cobalt was unsuccessful,

resulting in no metal ions in the polymers network. Furthermore, the CMPs synthesised by Route 2 with copper show very strong redox peaks (Figure 41 **(C)**, **(D)**, **(E)** and **(F)**). In the argon atmosphere, CMP-TP-1-1-Cu on a glassy carbon electrode exhibit a reduction peak at 0.10 V vs V_{RHE}, which is associated with an oxidation peak at 0.65 V vs V_{RHE}. In CO_2, the reduction peaks have all shifted 0.10 V vs V_{RHE} to a more positive value, as explained above. In addition, these values may also be attributed to the polymer/Cu mixed particles, which would promote electron migration from the conduction band of the polymer to the metal nanoparticles. In a CO_2 atmosphere, the current density for all materials is higher in argon. Owing to the CO_2 capture properties of the materials, obtaining higher current for a cathode indicates that the CO_2ECR rate is faster.

Furthermore, CMPs synthesised by Route 2 with copper exhibit the highest current peaks, indicating higher electrocatalytic activity. According to these results, the redox activity could be greatly enhanced with the incorporation of copper species into the porous network.

4. Conclusions and Future Work

4.1. Conclusions

The functional and structural design of CMPs provides opportunities for these materials to be used in a range of applications. In this study, a new class of nitrogen-rich CMPs containing terpyridine (CMP-TPs) and bipyridine derivatives (CMP-BPs) were designed, synthesized and characterized. Additionally, the properties of these CMPs were tuned by controlling the synthesis conditions such as core-to-linker ratio and solvent. Metals were then introduced to the framework for further studies. The following conclusions were obtained based on the results.

In the first part of the study, in comparison to the PTPA sample previously reported by the Faul research group,[61] incorporating terpyridine units into the framework has led to lower surface areas from 52 m^2/g to 49 m^2/g, while incorporating bipyridine units has led to an increase to 75 m^2/g. A suggested reason for this behaviour is owing to the bulky nature of the terpyridine units, which could be leading to steric hindrance effects and resulting in a reduction in porosity. On the other hand, the CO_2 adsorption ability unexpectedly showed a decrease from 3.7 wt% to 1.1 wt%. An increase in co-monomer (TP or BP) units in the framework leads to an increase in the number of binding sites; however, the surface area and CO_2 adsorption slightly reduced.

Afterwards, calculation of HSPs was used to optimize the yield and surface area of these materials. Propylene carbonate was chosen as optimal solvent for the synthesis. However, the outcomes have shown that the surface area of the materials synthesised in propylene carbonate significantly decreased in comparison to the materials synthesised in toluene from 49 m^2/g to 14 m^2/g for CMP-TPs and from 75 m^2/g to 42 m^2/g for CMP-BPs. It was postulated that the mechanism of HSP proposed in this study is not enforceable due to having a simple method that does not take the contribution of the three sub-components into account. For this reason, it was suggested that the new toolkit (M-Locator) developed by Xue Fang et al[150] needs to be further studied to efficiently obtain HSP of the material.

Studies have shown that porous materials can be tuned by metal incorporation, whilst potentially providing additional catalytic functionality. For this reason, the presence of the well-known metal-binding bipyridine and terpyridine motifs were exploited to bind different metal ions to the CMP framework. According to the results, the surface area of all materials doped with metals have significantly increased from 14 m^2/g to 163 m^2/g for CMP-TPs and from 42 m^2/g to 204 m^2/g for CMP-BPs, along with a shift to micropores in the PSD. There is also a great increase of ~ 300% in CO_2 adsorption for the metal-containing CMPs synthesised by post-synthetic metalation. According to all observed results, the post-synthetic metalation of CMPs show promising properties related to CO_2 capture. The presence of both cobalt and copper fragments in the framework enhanced the CO_2 uptake of the CMPs to between 4.2 - 5.7 wt%, which could be related to their positive charge that would create dipole–quadrupole interactions with CO_2 molecules. Further studies should be focused on enlarging the surface area or adding more metal ions in order to increase the CO_2 uptake capacity of the materials.

In the second part of the study, preliminary investigations of the redox processes of the synthesised materials by cyclic voltammetry methods were started to understand if the materials could be used as catalysts for electrochemical reduction of CO_2. It was observed that CMP-TPs and CMP-BPs are catalytically active toward electrochemical reduction of CO_2. Furthermore, the results have demonstrated that their electrocatalytic behaviour could be further improved with the incorporating metals via metal-binding sites in the CMP framework.

4.2. Future Work

This study exemplifies rules that could assist in the future design of CMPs for CO_2 capture and conversion applications. Following on the investigations and results, nitrogen-rich CMPs, and particularly metal-containing materials synthesised in this work could find future applications as catalysts. Further studies need to be undertaken to prepare CMPs with higher surface area, narrower PSD and higher adsorption capacity. To achieve these goals,

the synthesis conditions such as changing the catalyst and ligand, and addition of inorganic salts could be investigated and applied.

Further calculations and use of HSPs (and the newly developed toolkits from the Faul Research Group)[150] in the BXJ approach are required to explore the influence of solvent quality on the final properties and function of CMPs. This investigation showed shortcomings of the current approach, as the use of the optimal solvent, propylene carbonate, did not yield the expected results.

Another area where further work is required is to investigate the electrochemical properties of the metal-containing CMPs in detail, including chronoamperometry measurements, CO_2RR electrolysis under constant potential to study the conversion of CO_2 into valuable products. If this outcome can be achieved, a number of exciting avenues will be opened up for a wide range of new applications related to sustainable fuels, feedstocks and value-added products in the future.

5. References

[1] A. Buis, A Degree of Concern: Why Global Temperatures Matter – Climate Change: Vital Signs of the Planet, 2019. https://climate.nasa.gov/news/2865/a-degree-of-concern-why-global-temperatures-matter/. (Accessed 27-04-2022).

[2] J. Houghton, Global warming, Reports on Progress in Physics 68(6) (2005) 1343–1403.

[3] D.W. Kweku, O. Bismark, A. Maxwell, K.A. Desmond, K.B. Danso, E.A. Oti-Mensah, A.T. Quachie, B. Adormaa, Greenhouse effect: greenhouse gases and their impact on global warming, Journal of Scientific Research and Reports 17(6) (2018) 1-9.

[4] L. Perkins, Global Temperature Anomalies from 1880 to 2021, 2022. https://svs.gsfc.nasa.gov/4964. (Accessed 27-04-2022).

[5] C. Le Quéré, M.R. Raupach, J.G. Canadell, G. Marland, L. Bopp, P. Ciais, T.J. Conway, S.C. Doney, R.A. Feely, P. Foster, Trends in the sources and sinks of carbon dioxide, Nature Geoscience 2(12) (2009) 831-836.

[6] E.S. Sanz-Pérez, C.R. Murdock, S.A. Didas, C.W. Jones, Direct capture of CO_2 from ambient air, Chemical Reviews 116(19) (2016) 11840-11876.

[7] Q. Wang, J. Luo, Z. Zhong, A. Borgna, CO_2 capture by solid adsorbents and their applications: current status and new trends, Energy & Environmental Science 4(1) (2011) 42-55.

[8] C. Zhang, Atmospheric CO_2 from AIRS 2002-2016, 2016. https://svs.gsfc.nasa.gov/4533. (Accessed 30-04-2022).

[9] J. Rogelj, M. Den Elzen, N. Höhne, T. Fransen, H. Fekete, H. Winkler, R. Schaeffer, F. Sha, K. Riahi, M. Meinshausen, Paris Agreement climate proposals need a boost to keep warming well below 2 C, Nature 534(7609) (2016) 631-639.

[10] J. Blau, The Paris Agreement: climate change, solidarity, and human rights, Springer2017.

[11] W. Wang, M. Zhou, D. Yuan, Carbon dioxide capture in amorphous porous organic polymers, Journal of Materials Chemistry A 5(4) (2017) 1334-1347.

[12] M. Younas, M. Sohail, L. Leong, M.J. Bashir, S. Sumathi, Feasibility of CO_2 adsorption by solid adsorbents: a review on low-temperature systems, International Journal of Environmental Science and Technology 13(7) (2016) 1839-1860.

[13] J.-S.M. Lee, A.I. Cooper, Advances in conjugated microporous polymers, Chemical Reviews 120(4) (2020) 2171-2214.

[14] J. Chen, W. Yan, E.J. Townsend, J. Feng, L. Pan, V. Del Angel Hernandez, C.F.J. Faul, Tunable surface area, porosity, and function in conjugated microporous polymers, Angewandte Chemie 131(34) (2019) 11841-11845.

[15] S.-J. Yang, X. Ding, B.-H. Han, Conjugated microporous polymers with extended π-structures for organic vapor adsorption, Macromolecules 51(3) (2018) 947-953.

[16] X. Wang, Y. Zhao, L. Wei, C. Zhang, J.-X. Jiang, Nitrogen-rich conjugated microporous polymers: impact of building blocks on porosity and gas adsorption, Journal of Materials Chemistry A 3(42) (2015) 21185-21193.

[17] L. Wang, C. Yao, W. Xie, G. Xu, S. Zhang, Y. Xu, A series of thiophene-and nitrogen-rich conjugated microporous polymers for efficient iodine and carbon dioxide capture, New Journal of Chemistry 45(42) (2021) 19636-19640.

[18] P.Z. Li, Y. Zhao, Nitrogen-Rich Porous Adsorbents for CO_2 Capture and Storage, Chemistry–An Asian Journal 8(8) (2013) 1680-1691.

[19] J. Nam, E. Jeon, S.-Y. Moon, J.-W. Park, Rearranged Copolyurea Networks for Selective Carbon Dioxide Adsorption at Room Temperature, Polymers 13(22) (2021) 4004.

[20] Y. Xu, S. Jin, H. Xu, A. Nagai, D. Jiang, Conjugated microporous polymers: design, synthesis and application, Chemical Society Reviews 42(20) (2013) 8012-8031.

[21] M.E. Davis, Ordered porous materials for emerging applications, Nature 417(6891) (2002) 813-821.

[22] P. Kaur, J.T. Hupp, S.T. Nguyen, Porous organic polymers in catalysis: opportunities and challenges, ACS Catalysis 1(7) (2011) 819-835.

[23] Y. Zhang, S.N. Riduan, Functional porous organic polymers for heterogeneous catalysis, Chemical Society Reviews 41(6) (2012) 2083-2094.

[24] L. Zou, Y. Sun, S. Che, X. Yang, X. Wang, M. Bosch, Q. Wang, H. Li, M. Smith, S. Yuan, Porous organic polymers for post-combustion carbon capture, Advanced Materials 29(37) (2017) 1700229.

[25] D.S. Ahmed, G.A. El-Hiti, E. Yousif, A.A. Ali, A.S. Hameed, Design and synthesis of porous polymeric materials and their applications in gas capture and storage: a review, Journal of Polymer Research 25(3) (2018) 1-21.

[26] A. Li, H.-X. Sun, D.-Z. Tan, W.-J. Fan, S.-H. Wen, X.-J. Qing, G.-X. Li, S.-Y. Li, W.-Q. Deng, Superhydrophobic conjugated microporous polymers for separation and adsorption, Energy & Environmental Science 4(6) (2011) 2062-2065.

[27] Q. Chen, M. Luo, P. Hammershøj, D. Zhou, Y. Han, B.W. Laursen, C.-G. Yan, B.-H. Han, Microporous polycarbazole with high specific surface area for gas storage and separation, Journal of the American Chemical Society 134(14) (2012) 6084-6087.

[28] P. Lindemann, M. Tsotsalas, S. Shishatskiy, V. Abetz, P. Krolla-Sidenstein, C. Azucena, L. Monnereau, A. Beyer, 1 5 A. Gölzhäuser, V. Mugnaini, H. Gliemann, S. Bräse and C. Wöll, Chem. Mater. 26 (2014) 7189-7193.

[29] T. Wenzel, D. Härtter, P. Bombelli, C.J. Howe, U. Steiner, Porous translucent electrodes enhance current generation from photosynthetic biofilms, Nature Communications 9(1) (2018) 1-9.

[30] R.L. Vekariya, A. Dhar, P.K. Paul, S. Roy, An overview of engineered porous material for energy applications: a mini-review, Ionics 24(1) (2018) 1-17.

[31] P. Liu, G.-F. Chen, Porous materials: processing and applications, Elsevier2014.

[32] M. Thommes, K. Kaneko, A.V. Neimark, J.P. Olivier, F. Rodriguez-Reinoso, J. Rouquerol, K.S. Sing, Physisorption of gases, with special reference to the evaluation of surface area and pore size distribution (IUPAC Technical Report), Pure and Applied Chemistry 87(9-10) (2015) 1051-1069.

[33] T. Liu, F. Zhang, Y. Song, Y. Li, Revitalizing carbon supercapacitor electrodes with hierarchical porous structures, Journal of Materials Chemistry A 5(34) (2017) 17705-17733.

[34] L.J. Gibson, Cellular solids, Mrs Bulletin 28(4) (2003) 270-274.

[35] H. Bildirir, V.G. Gregoriou, A. Avgeropoulos, U. Scherf, C.L. Chochos, Porous organic polymers as emerging new materials for organic photovoltaic applications: current status and future challenges, Materials Horizons 4(4) (2017) 546-556.

[36] N. Huang, G. Day, X. Yang, H. Drake, H.-C. Zhou, Engineering porous organic polymers for carbon dioxide capture, Science China Chemistry 60(8) (2017) 1007-1014.

[37] J.X. Jiang, F. Su, A. Trewin, C.D. Wood, N.L. Campbell, H. Niu, C. Dickinson, A.Y. Ganin, M.J. Rosseinsky, Y.Z. Khimyak, Conjugated microporous poly (aryleneethynylene) networks, Angewandte Chemie International Edition 46(45) (2007) 8574-8578.

[38] A.I. Cooper, Conjugated microporous polymers, Advanced Materials 21(12) (2009) 1291-1295.

[39] J.-X. Jiang, F. Su, H. Niu, C.D. Wood, N.L. Campbell, Y.Z. Khimyak, A.I. Cooper, Conjugated microporous poly (phenylene butadiynylene) s, Chemical Communications (4) (2008) 486-488.

[40] J. Weber, A. Thomas, Toward stable interfaces in conjugated polymers: microporous poly (p-phenylene) and poly (phenyleneethynylene) based on a spirobifluorene building block, Journal of the American Chemical Society 130(20) (2008) 6334-6335.

[41] Q. Liu, Z. Tang, M. Wu, Z. Zhou, Design, preparation and application of conjugated microporous polymers, Polymer International 63(3) (2014) 381-392.

[42] S. Luo, Z. Zeng, G. Zeng, Z. Liu, R. Xiao, P. Xu, H. Wang, D. Huang, Y. Liu, B. Shao, Recent advances in conjugated microporous polymers for photocatalysis: designs, applications, and prospects, Journal of Materials Chemistry A 8(14) (2020) 6434-6470.

[43] S. Luo, Z. Zeng, H. Wang, W. Xiong, B. Song, C. Zhou, A. Duan, X. Tan, Q. He, G. Zeng, Recent progress in conjugated microporous polymers for clean energy: synthesis, modification, computer simulations, and applications, Progress in Polymer Science 115 (2021) 101374.

[44] Y.B. Zhou, Z.P. Zhan, Conjugated microporous polymers for heterogeneous catalysis, Chemistry–An Asian Journal 13(1) (2018) 9-19.

[45] K. Amin, N. Ashraf, L. Mao, C.F. Faul, Z. Wei, Conjugated microporous polymers for energy storage: Recent progress and challenges, Nano Energy 85 (2021) 105958.

[46] Y. Luo, B. Li, L. Liang, B. Tan, Synthesis of cost-effective porous polyimides and their gas storage properties, Chemical Communications 47(27) (2011) 7704-7706.

[47] X. Zhu, C. Tian, S.M. Mahurin, S.-H. Chai, C. Wang, S. Brown, G.M. Veith, H. Luo, H. Liu, S. Dai, A superacid-catalyzed synthesis of porous membranes based on triazine frameworks for CO_2 separation, Journal of the American Chemical Society 134(25) (2012) 10478-10484.

[48] K. Huang, F. Liu, S. Dai, Solvothermal synthesis of hierarchically nanoporous organic polymers with tunable nitrogen functionality for highly selective capture of CO_2, Journal of Materials Chemistry A 4(34) (2016) 13063-13070.

[49] P. Zhang, Z. Weng, J. Guo, C. Wang, Solution-dispersible, colloidal, conjugated porous polymer networks with entrapped palladium nanocrystals for heterogeneous catalysis of the Suzuki–Miyaura coupling reaction, Chemistry of Materials 23(23) (2011) 5243-5249.

[50] B. Bonillo, R.S. Sprick, A.I. Cooper, Tuning photophysical properties in conjugated microporous polymers by comonomer doping strategies, Chemistry of Materials 28(10) (2016) 3469-3480.

[51] Q. Shi, H. Sun, R. Yang, Z. Zhu, W. Liang, D. Tan, B. Yang, A. Li, W. Deng, Synthesis of conjugated microporous polymers for gas storage and selective adsorption, Journal of Materials Science 50(19) (2015) 6388-6394.

[52] Q. Chen, M. Luo, T. Wang, J.-X. Wang, D. Zhou, Y. Han, C.-S. Zhang, C.-G. Yan, B.-H. Han, Porous organic polymers based on propeller-like hexaphenylbenzene building units, Macromolecules 44(14) (2011) 5573-5577.

[53] R. Dawson, A. Laybourn, R. Clowes, Y.Z. Khimyak, D.J. Adams, A.I. Cooper, Functionalized conjugated microporous polymers, Macromolecules 42(22) (2009) 8809-8816.

[54] J.-X. Jiang, F. Su, A. Trewin, C.D. Wood, H. Niu, J.T. Jones, Y.Z. Khimyak, A.I. Cooper, Synthetic control of the pore dimension and surface area in conjugated microporous polymer and copolymer networks, Journal of the American Chemical Society 130(24) (2008) 7710-7720.

[55] J. Schmidt, M. Werner, A. Thomas, Conjugated microporous polymer networks via yamamoto polymerization, Macromolecules 42(13) (2009) 4426-4429.

[56] G. Li, B. Zhang, J. Yan, Z. Wang, The directing effect of linking units on building microporous architecture in tetraphenyladmantane-based poly (Schiff base) networks, Chemical Communications 50(15) (2014) 1897-1899.

[57] A. Singh, P. Verma, D. Samanta, T. Singh, T.K. Maji, Bimodal Heterogeneous Functionality in Redox-Active Conjugated Microporous Polymer toward Electrocatalytic Oxygen Reduction and Photocatalytic Hydrogen Evolution, Chemistry–A European Journal 26(17) (2020) 3810-3817.

[58] M.G. Schwab, B. Fassbender, H.W. Spiess, A. Thomas, X. Feng, K. Mullen, Catalyst-free preparation of melamine-based microporous polymer networks through Schiff base chemistry, Journal of the American Chemical Society 131(21) (2009) 7216-7217.

[59] M. Yang, Y. Liu, H. Chen, D. Yang, H. Li, Porous N-doped carbon prepared from triazine-based polypyrrole network: a highly efficient metal-free catalyst for oxygen reduction reaction in alkaline electrolytes, ACS Applied Materials & Interfaces 8(42) (2016) 28615-28623.

[60] S. Ren, M.J. Bojdys, R. Dawson, A. Laybourn, Y.Z. Khimyak, D.J. Adams, A.I. Cooper, Porous, fluorescent, covalent triazine-based frameworks via room-temperature and microwave-assisted synthesis, Advanced Materials 24(17) (2012) 2357-2361.

[61] Y. Liao, J. Weber, C.F.J. Faul, Conjugated microporous polytriphenylamine networks, Chemical Communications 50(59) (2014) 8002-8005.

[62] N. Chaoui, M. Trunk, R. Dawson, J. Schmidt, A. Thomas, Trends and challenges for microporous polymers, Chemical Society Reviews 46(11) (2017) 3302-3321.

[63] M.M. Heravi, Z. Kheilkordi, V. Zadsirjan, M. Heydari, M. Malmir, Buchwald-Hartwig reaction: an overview, Journal of Organometallic Chemistry 861 (2018) 17-104.

[64] G. Zeni, R.C. Larock, Synthesis of heterocycles via palladium-catalyzed oxidative addition, Chemical Reviews 106(11) (2006) 4644-4680.

[65] N. Miyaura, S.L. Buchwald, Cross-coupling reactions: a practical guide, Springer2002.

[66] U. Christmann, R. Vilar, Monoligated palladium species as catalysts in cross-coupling reactions, Angewandte Chemie International Edition 44(3) (2005) 366-374.

[67] N. Miyaura, A. Suzuki, Palladium-catalyzed cross-coupling reactions of organoboron compounds, Chemical Reviews 95(7) (1995) 2457-2483.

[68] A. Singh, S. Roy, C. Das, D. Samanta, T.K. Maji, Metallophthalocyanine-based redox active metal–organic conjugated microporous polymers for OER catalysis, Chemical Communications 54(35) (2018) 4465-4468.

[69] J.X. Jiang, C. Wang, A. Laybourn, T. Hasell, R. Clowes, Y.Z. Khimyak, J. Xiao, S.J. Higgins, D.J. Adams, A.I. Cooper, Metal–organic conjugated microporous polymers, Angewandte Chemie International Edition 50(5) (2011) 1072-1075.

[70] M. Eddaoudi, J. Kim, N. Rosi, D. Vodak, J. Wachter, M. O'Keeffe, O.M. Yaghi, Systematic design of pore size and functionality in isoreticular MOFs and their application in methane storage, Science 295(5554) (2002) 469-472.

[71] P. Langley, J. Hulliger, Nanoporous and mesoporous organic structures: new openings for materials research, Chemical Society Reviews 28(5) (1999) 279-291.

[72] M. Crucianelli, B.M. Bizzarri, R. Saladino, SBA-15 anchored metal containing catalysts in the oxidative desulfurization process, Catalysts 9(12) (2019) 984.

[73] C.L. Smith, R. Clowes, R.S. Sprick, A.I. Cooper, A.J. Cowan, Metal–organic conjugated microporous polymer containing a carbon dioxide reduction electrocatalyst, Sustainable Energy & Fuels 3(11) (2019) 2990-2994.

[74] J. Albo, D. Vallejo, G. Beobide, O. Castillo, P. Castaño, A. Irabien, Copper-based metal–Organic porous materials for CO_2 electrocatalytic reduction to alcohols, ChemSusChem 10(6) (2017) 1100-1109.

[75] M.D. Marquez-Medina, R. Luque, A.M. Balu, F. Ivars-Barceló, C. Carrillo-Carrión, Metal doping of porous materials via a post-synthetic mechano-chemical approach: a general route to design low-loaded versatile catalytic systems, Catalysis Science & Technology 11(6) (2021) 2103-2109.

[76] C.M. Hansen, Hansen solubility parameters: a user's handbook, CRC press2007.

[77] S. Abbott, C.M. Hansen, Hansen solubility parameters in practice, Hansen-Solubility2008.

[78] V.K. Undavalli, C. Ling, B. Khandelwal, Impact of alternative fuels and properties on elastomer compatibility, Aviation Fuels, Elsevier2021, pp. 113-132.

[79] J. Lara, F. Zimmermann, D. Drolet, C.M. Hansen, A. Chollot, N. Monta, The use of the Hansen solubility parameters in the selection of protective polymeric materials resistant to chemicals, International Journal of Current Research 9(3) (2017) 47860-47867.

[80] Y. Agata, H. Yamamoto, Determination of Hansen solubility parameters of ionic liquids using double-sphere type of Hansen solubility sphere method, Chemical Physics 513 (2018) 165-173.

[81] F. Fu, L. Lin, E. Xu, Functional pretreatments of natural raw materials, Advanced high strength natural fibre composites in construction, Elsevier2017, pp. 87-114.

[82] P. Liu, Chapter Nine-Characterization Methods: Basic Factors, Editor (s): PS Liu, GF Chen. Porous Materials, Butterworth-Heinemann, 2014.

[83] D.P. Broom, K.M. Thomas, Gas adsorption by nanoporous materials: Future applications and experimental challenges, MRS Bulletin 38(5) (2013) 412-421.

[84] M. Leuenberger, M. Schibig, P. Nyfeler, Gas adsorption and desorption effects on cylinders and their importance for long-term gas records, Atmospheric Measurement Techniques 8(12) (2015) 5289-5299.

[85] J. Rouquerol, F. Rouquerol, P. Llewellyn, G. Maurin, K.S. Sing, Adsorption by powders and porous solids: principles, methodology and applications, Academic press2013.

[86] A.B.D. Nandiyanto, G.C.S. Girsang, R. Maryanti, R. Ragadhita, S. Anggraeni, F.M. Fauzi, P. Sakinah, A.P. Astuti, D. Usdiyana, M. Fiandini, Isotherm adsorption characteristics of carbon microparticles prepared from pineapple peel waste, Communications in Science and Technology 5(1) (2020) 31-39.

[87] K.S. Sing, Reporting physisorption data for gas/solid systems with special reference to the determination of surface area and porosity (Recommendations 1984), Pure and Applied Chemistry 57(4) (1985) 603-619.

[88] I. Langmuir, The adsorption of gases on plane surfaces of glass, mica and platinum, Journal of the American Chemical society 40(9) (1918) 1361-1403.

[89] S. Brunauer, P.H. Emmett, E. Teller, Adsorption of gases in multimolecular layers, Journal of the American Chemical Society 60(2) (1938) 309-319.

[90] F. Ambroz, T.J. Macdonald, V. Martis, I.P. Parkin, Evaluation of the BET Theory for the Characterization of Meso and Microporous MOFs, Small Methods 2(11) (2018) 1800173.

[91] W. Steele, G. Zgrablich, W. Rudzinski, Equilibria and dynamics of gas adsorption on heterogeneous solid surfaces, Elsevier1996.

[92] M. Naderi, Surface Area: Brunauer–Emmett–Teller (BET), Progress in Filtration and Separation, Elsevier2015, pp. 585-608.

[93] P. Sinha, A. Datar, C. Jeong, X. Deng, Y.G. Chung, L.-C. Lin, Surface area determination of porous materials using the Brunauer–Emmett–Teller (BET) method: limitations and improvements, The Journal of Physical Chemistry C 123(33) (2019) 20195-20209.

[94] J. Rouquerol, D. Avnir, C. Fairbridge, D. Everett, J. Haynes, N. Pernicone, J. Ramsay, K. Sing, K. Unger, Recommendations for the characterization of porous solids (Technical Report), Pure and Applied Chemistry 66(8) (1994) 1739-1758.

[95] J. Broekhoff, Mesopore determination from nitrogen sorption isotherms: Fundamentals, scope, limitations, Studies in surface science and catalysis, Elsevier1979, pp. 663-684.

[96] S. Lowell, J.E. Shields, M.A. Thomas, M. Thommes, Characterization of porous solids and powders: surface area, pore size and density, Springer Science & Business Media2006.

[97] K.V. Kumar, S. Gadipelli, B. Wood, K.A. Ramisetty, A.A. Stewart, C.A. Howard, D.J. Brett, F. Rodriguez-Reinoso, Characterization of the adsorption site energies and heterogeneous surfaces of porous materials, Journal of Materials Chemistry A 7(17) (2019) 10104-10137.

[98] S.C. Roy, O.K. Varghese, M. Paulose, C.A. Grimes, Toward solar fuels: photocatalytic conversion of carbon dioxide to hydrocarbons, ACS Nano 4(3) (2010) 1259-1278.

[99] M. Mikkelsen, M. Jørgensen, F.C. Krebs, The teraton challenge. A review of fixation and transformation of carbon dioxide, Energy & Environmental Science 3(1) (2010) 43-81.

[100] G. Centi, S. Perathoner, Opportunities and prospects in the chemical recycling of carbon dioxide to fuels, Catalysis Today 148(3-4) (2009) 191-205.

[101] J. Qiao, Y. Liu, F. Hong, J. Zhang, A review of catalysts for the electroreduction of carbon dioxide to produce low-carbon fuels, Chemical Society Reviews 43(2) (2014) 631-675.

[102] R. Lin, J. Guo, X. Li, P. Patel, A. Seifitokaldani, Electrochemical reactors for CO_2 conversion, Catalysts 10(5) (2020) 473.

[103] W. Zhang, Y. Hu, L. Ma, G. Zhu, Y. Wang, X. Xue, R. Chen, S. Yang, Z. Jin, Progress and perspective of electrocatalytic CO2 reduction for renewable carbonaceous fuels and chemicals, Advanced Science 5(1) (2018) 1700275.

[104] K. Liu, W.A. Smith, T. Burdyny, Introductory guide to assembling and operating gas diffusion electrodes for electrochemical CO2 reduction, ACS Energy Letters 4(3) (2019) 639-643.

[105] O. Ola, M.M. Maroto-Valer, Review of material design and reactor engineering on TiO2 photocatalysis for CO2 reduction, Journal of Photochemistry and Photobiology C: Photochemistry Reviews 24 (2015) 16-42.

[106] A.K.S. Kumar, Y. Zhang, D. Li, R.G. Compton, A mini-review: How reliable is the drop casting technique?, Electrochemistry Communications 121 (2020) 106867.

[107] A.S.R. Machado, M.N. da Ponte, CO_2 capture and electrochemical conversion, Current Opinion in Green and Sustainable Chemistry 11 (2018) 86-90.

[108] T. Liu, S. Ali, Z. Lian, B. Li, D.S. Su, CO_2 electoreduction reaction on heteroatom-doped carbon cathode materials, Journal of Materials Chemistry A 5(41) (2017) 21596-21603.

[109] B.E. Warren, X-ray Diffraction, Courier Corporation1990.

[110] C. Suryanarayana, M.G. Norton, X-ray diffraction: a practical approach, Springer Science & Business Media1998.

[111] H. Stanjek, W. Häusler, Basics of X-ray Diffraction, Hyperfine Interactions 154(1) (2004) 107-119.

[112] M. Ermrich, D. Opper, XRD for the analyst, Getting Acquainted with the Principles. Second. Panalytical (2013).

[113] W.H. Bragg, W.L. Bragg, The reflection of X-rays by crystals, Proceedings of the Royal Society of London. Series A, Containing Papers of a Mathematical and Physical Character 88(605) (1913) 428-438.

[114] A. Mezzi, S. Kaciulis, Surface investigation of carbon films: from diamond to graphite, Surface and Interface Analysis 42(6-7) (2010) 1082-1084.

[115] H. Balyuzi, R. Burge, X-Ray diffraction by amorphous polymers: Models for biological systems, Biopolymers: Original Research on Biomolecules 10(5) (1971) 777-788.

[116] C.M. Simonescu, Application of FTIR spectroscopy in environmental studies, Advanced Aspects of Spectroscopy 29(1) (2012) 77-86.

[117] A. Dutta, Fourier transform infrared spectroscopy, Spectroscopic Methods for Nanomaterials Characterization (2017) 73-93.

[118] B.C. Smith, Fundamentals of Fourier transform infrared spectroscopy, CRC press2011.

[119] P.R. Griffiths, J.A. De Haseth, Fourier transform infrared spectrometry, John Wiley & Sons2007.

[120] H.-H. Perkampus, UV-VIS Spectroscopy and its Applications, Springer Science & Business Media2013.

[121] D.C. Harris, Quantitative Chemical Analysis, Macmillan2010.

[122] D.L. Pavia, G.M. Lampman, G.S. Kriz, J.A. Vyvyan, Introduction to spectroscopy, Cengage learning2014.

[123] P. Bouguer, Essai d'optique sur la gradation de la lumière, Claude Jombert1729.

[124] W. Mäntele, E. Deniz, UV–VIS absorption spectroscopy: Lambert-Beer reloaded, Elsevier, 2017, pp. 965-968.

[125] C. Schaller, UV-Visible Spectroscopy - Metal Ions, 2020. https://chem.libretexts.org/@go/page/189755. (Accessed 30-04-2022).

[126] J.I. Goldstein, D.E. Newbury, J.R. Michael, N.W. Ritchie, J.H.J. Scott, D.C. Joy, Scanning electron microscopy and X-ray microanalysis, Springer2017.

[127] G. Leofanti, M. Padovan, G. Tozzola, B. Venturelli, Surface area and pore texture of catalysts, Catalysis Today 41(1-3) (1998) 207-219.

[128] K. Vernon-Parry, Scanning electron microscopy: an introduction, III-Vs Review 13(4) (2000) 40-44.

[129] A. Polini, F. Yang, Physicochemical characterization of nanofiber composites, Nanofiber Composites for Biomedical Applications, Elsevier2017, pp. 97-115.

[130] L. Yang, Y. Ma, Y. Xu, G. Chang, Cation–π induced lithium-doped conjugated microporous polymer with remarkable hydrogen storage performance, Chemical Communications 55(75) (2019) 11227-11230.

[131] V.A. Bolotov, K.A. Kovalenko, D.G. Samsonenko, X. Han, X. Zhang, G.L. Smith, L.J. McCormick, S.J. Teat, S. Yang, M.J. Lennox, Enhancement of CO2 Uptake and Selectivity in a Metal–Organic Framework by the Incorporation of Thiophene Functionality, Inorganic Chemistry 57(9) (2018) 5074-5082.

[132] M.S.B. Reddy, D. Ponnamma, K.K. Sadasivuni, B. Kumar, A.M. Abdullah, Carbon dioxide adsorption based on porous materials, RSC Advances 11(21) (2021) 12658-12681.

[133] A. Jain, S.P. Ong, G. Hautier, W. Chen, W.D. Richards, S. Dacek, S. Cholia, D. Gunter, D. Skinner, G. Ceder, Commentary: The Materials Project: A materials genome approach to accelerating materials innovation, APL Materials 1(1) (2013) 011002.

[134] S.P. Ong, W.D. Richards, A. Jain, G. Hautier, M. Kocher, S. Cholia, D. Gunter, V.L. Chevrier, K.A. Persson, G. Ceder, Python Materials Genomics (pymatgen): A robust, open-source python library for materials analysis, Computational Materials Science 68 (2013) 314-319.

[135] N. Zakowsky, S. Williamson, J.T. Irvine, Elaboration of CO2 tolerance limits of BaCe0. 9Y0. 1O3–δ electrolytes for fuel cells and other applications, Solid State Ionics 176(39-40) (2005) 3019-3026.

[136] Y. Li, Y.A. Samad, K. Polychronopoulou, S.M. Alhassan, K. Liao, From biomass to high performance solar–thermal and electric–thermal energy conversion and storage materials, Journal of Materials Chemistry A 2(21) (2014) 7759-7765.

[137] S. Abbott, Solubility science: principles and practice, TCNF Ltd: Ipswitch (2017).

[138] D.S. Surry, S.L. Buchwald, Dialkylbiaryl phosphines in Pd-catalyzed amination: a user's guide, Chemical Science 2(1) (2011) 27-50.

[139] G. Busca, Bases and basic materials in chemical and environmental processes. Liquid versus solid basicity, Chemical Reviews 110(4) (2010) 2217-2249.

[140] R. Dawson, A. Laybourn, Y.Z. Khimyak, D.J. Adams, A.I. Cooper, High surface area conjugated microporous polymers: the importance of reaction solvent choice, Macromolecules 43(20) (2010) 8524-8530.

[141] C. Mollart, A. Trewin, Rationalising the influence of solvent choice on the porosity of conjugated microporous polymers, Physical Chemistry Chemical Physics 22(38) (2020) 21642-21645.

[142] F.S. Macintyre, D.C. Sherrington, Control of porous morphology in suspension polymerized poly (divinylbenzene) resins using oligomeric porogens, Macromolecules 37(20) (2004) 7628-7636.

[143] J. Chen, W. Yan, E.J. Townsend, J. Feng, L. Pan, V. Del Angel Hernandez, C.F.J. Faul, Tunable surface area, porosity, and function in conjugated microporous polymers, Angewandte Chemie International Edition 58(34) (2019) 11715-11719.

[144] J. Chen, T. Qiu, W. Yan, C.F. Faul, Exploiting Hansen solubility parameters to tune porosity and function in conjugated microporous polymers, Journal of Materials Chemistry A 8(43) (2020) 22657-22665.

[145] Y. Zhang, C. Zhang, W. Shi, Z. Zhang, Y. Zhao, X. Luo, X. Liu, Pyridine-based conjugated microporous polymers as adsorbents for CO_2 uptake via weak supramolecular interaction, New Journal of Chemistry 46(14) (2022) 6394-6397.

[146] S. Ponnurangam, I.V. Chernyshova, P. Somasundaran, Nitrogen-containing polymers as a platform for CO2 electroreduction, Advances in Colloid and Interface Science 244 (2017) 184-198.

[147] W. Nie, D. Tarnopol, C.C. McCrory, The Effect of Extended Conjugation on Electrocatalytic CO_2 Reduction by Molecular Catalysts and Macromolecular Structures, Current Opinion in Electrochemistry (2021) 100716.

[148] C. Zhang, Y. Qiao, P. Xiong, W. Ma, P. Bai, X. Wang, Q. Li, J. Zhao, Y. Xu, Y. Chen, Conjugated microporous polymers with tunable electronic structure for high-performance potassium-ion batteries, ACS Nano 13(1) (2019) 745-754.

[149] L.-W. Luo, C. Zhang, P. Xiong, Y. Zhao, W. Ma, Y. Chen, J.H. Zeng, Y. Xu, J.-X. Jiang, A redox-active conjugated microporous polymer cathode for high-performance lithium/potassium-organic batteries, Science China Chemistry 64(1) (2021) 72-81.

[150] X. Fang, Hansen solubility parameters toolkits for efficient solvent selection and functionality control. *Manuscript in preparation.*, (2022).

6. Appendices

6.1. HSPs Results

6.1.1. CMP-TP-4

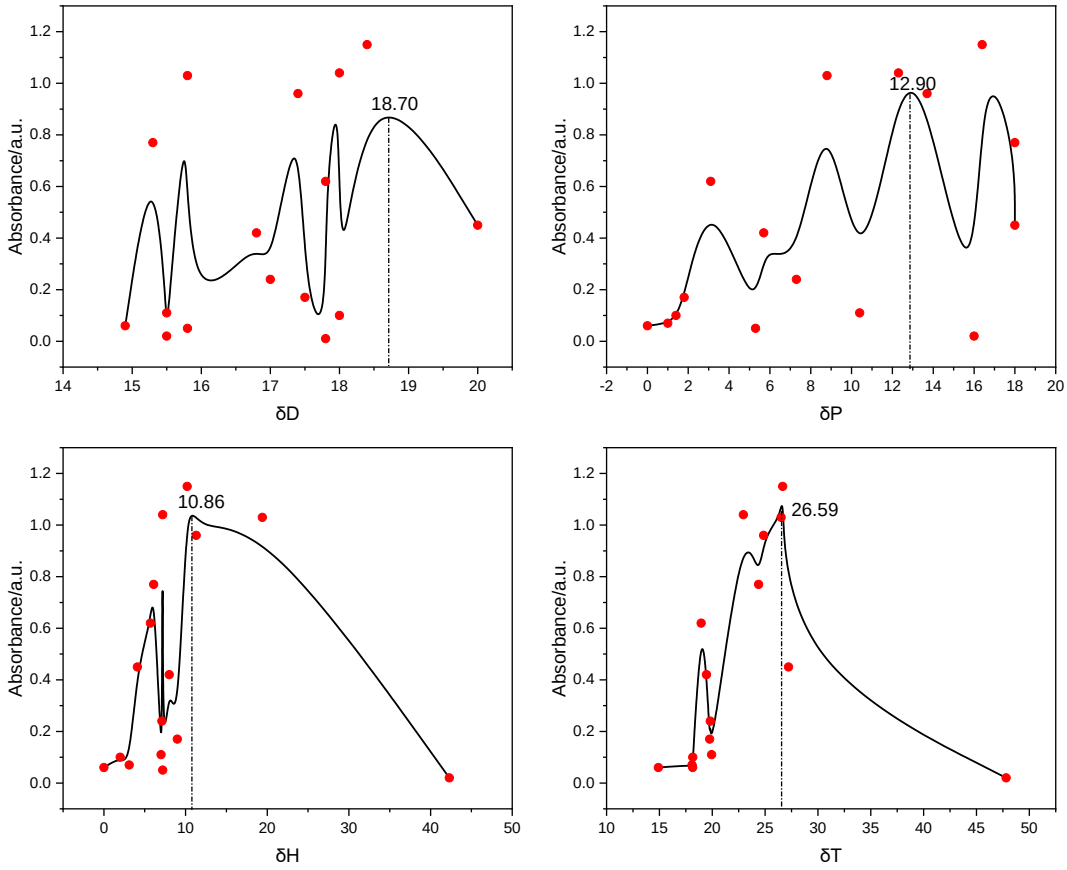

Figure 41 CMP-TP-4 concentration measured by UV/VIS spectroscopy, plotted with published Hansen solubility parameter of the chosen solvents: **(A)** disperse-, **(B)** polar-, **(C)** hydrogen-, **(D)** total solubility parameters

Table 19 HSPs of CMP-TP-4 in 16 solvents

Solvent	δ_D	δ_P	δ_H	δ_T	$\lvert\Delta\delta_T\rvert$
DMSO	*18.4*	*16.4*	*10.2*	*26.67*	*0.08*
DMF	17.4	13.7	11.3	24.86	1.73
Acetonitrile	15.3	18	6.1	24.39	2.2

NMP	18	12.3	7.2	22.95	3.64
Propylene carbonate	*20*	*18*	*4.1*	*27.22*	*0.63*
Xylene	17.8	1	3.1	18.09	8.5
Toluene	18	1.4	2	18.16	8.43
Ethanol	*15.8*	*8.8*	*19.4*	*26.52*	*0.07*
Dioxane	17.5	1.8	9	19.76	6.83
Chloroform	17.8	3.1	5.7	18.95	7.64
Acetone	15.5	10.4	7	19.94	6.65
Dichloromethane	17	7.3	7.1	19.82	6.77
Ethyl acetate	15.8	5.3	7.2	18.15	8.44
Hexane	14.9	0	0	14.9	11.69
THF	16.8	5.7	8	19.46	7.13
Water	15.5	16	42.3	47.81	21.22
CMP-TP-4	18.70	12.90	10.86	26.59	

6.1.2. CMP-BP-1

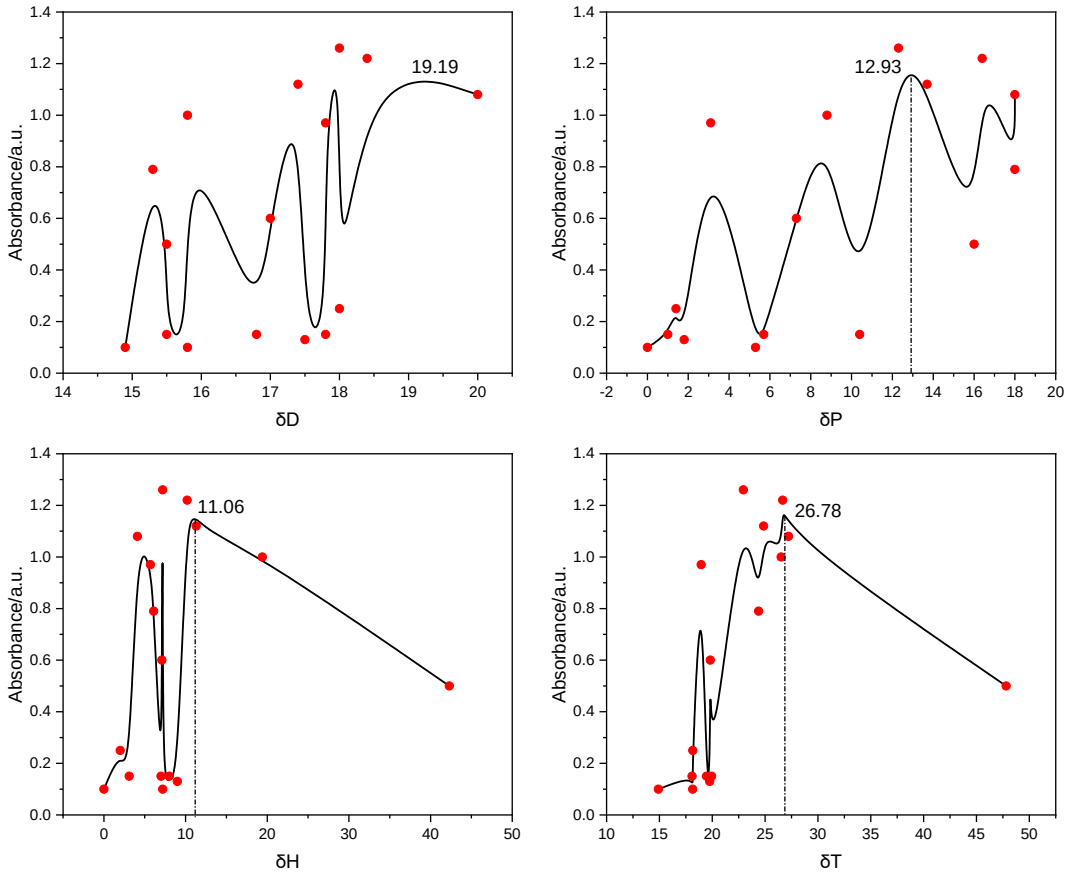

Figure 42 CMP-BP-1 concentration measured by UV/VIS spectroscopy, plotted with published Hansen solubility parameter of the chosen solvents: **(A)** disperse-, **(B)** polar-, **(C)** hydrogen-, **(D)** total solubility parameters

Table 20 HSPs of CMP-BP-1 in 16 solvents

Solvent	δ_D	δ_P	δ_H	δ_T	$\lvert\Delta\delta_T\rvert$
DMSO	*18.4*	*16.4*	*10.2*	*26.67*	*0.11*
DMF	17.4	13.7	11.3	24.86	1.92
Acetonitrile	15.3	18	6.1	24.39	2.39
NMP	18	12.3	7.2	22.95	3.83
Propylene carbonate	*20*	*18*	*4.1*	*27.22*	*0.44*
Xylene	17.8	1	3.1	18.09	8.69

Toluene	18	1.4	2	18.16	8.62
Ethanol	*15.8*	*8.8*	*19.4*	*26.52*	*0.26*
Dioxane	17.5	1.8	9	19.76	7.02
Chloroform	17.8	3.1	5.7	18.95	7.83
Acetone	15.5	10.4	7	19.94	6.84
Dichloromethane	17	7.3	7.1	19.82	6.96
Ethyl acetate	15.8	5.3	7.2	18.15	8.63
Hexane	14.9	0	0	14.9	11.88
THF	16.8	5.7	8	19.46	7.32
Water	15.5	16	42.3	47.81	21.03
CMP-BP-1	19.19	12.93	11.06	26.78	

6.1.3. CMP-BP-4

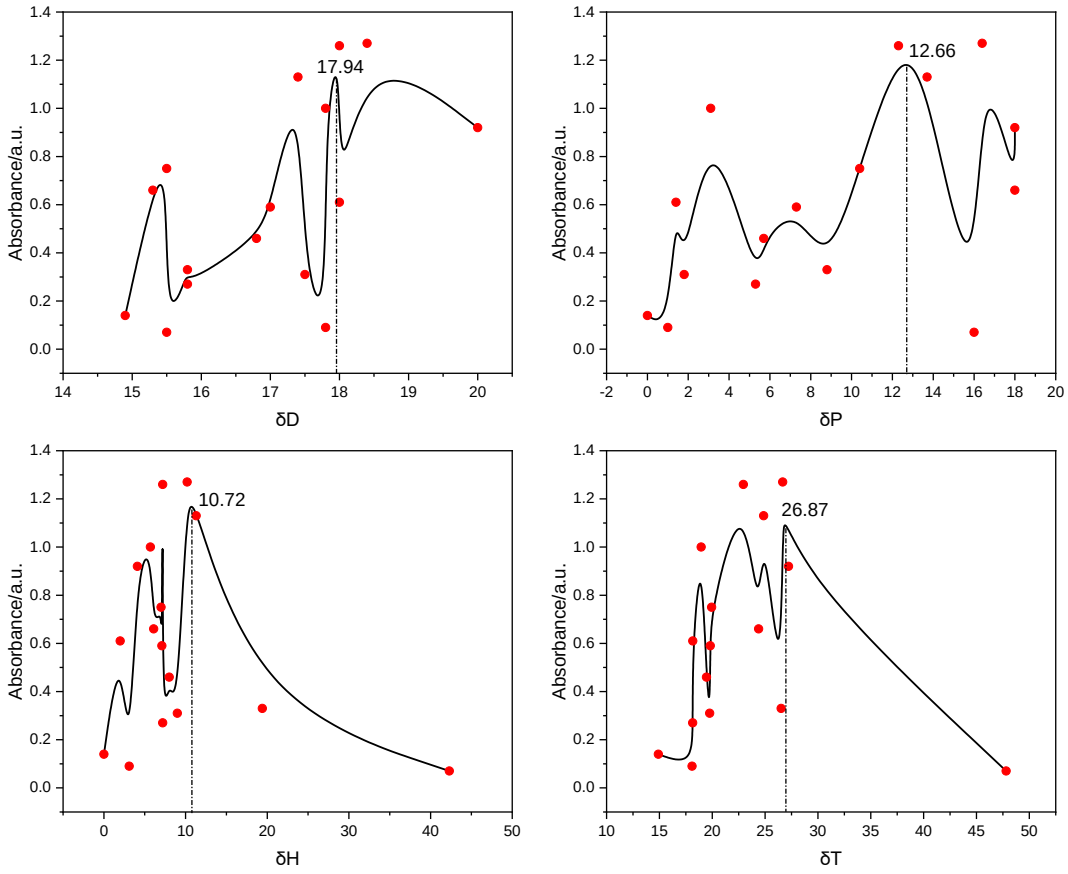

Figure 43 CMP-BP-4 concentration measured by UV/VIS spectroscopy, plotted with published Hansen solubility parameter of the chosen solvents: **(A)** disperse-, **(B)** polar-, **(C)** hydrogen-, **(D)** total solubility parameters

Table 21 HSPs of CMP-BP-4 in 16 solvents

Solvent	δ_D	δ_P	δ_H	δ_T	$\lvert\Delta\delta_T\rvert$
DMSO	*18.4*	*16.4*	*10.2*	*26.67*	*0.2*
DMF	17.4	13.7	11.3	24.86	2.01
Acetonitrile	15.3	18	6.1	24.39	2.48
NMP	18	12.3	7.2	22.95	3.92
Propylene carbonate	*20*	*18*	*4.1*	*27.22*	*0.35*
Xylene	17.8	1	3.1	18.09	8.78

Toluene	18	1.4	2	18.16	8.71
Ethanol	*15.8*	*8.8*	*19.4*	*26.52*	*0.35*
Dioxane	17.5	1.8	9	19.76	7.11
Chloroform	17.8	3.1	5.7	18.95	7.92
Acetone	15.5	10.4	7	19.94	6.93
Dichloromethane	17	7.3	7.1	19.82	7.5
Ethyl acetate	15.8	5.3	7.2	18.15	8.72
Hexane	14.9	0	0	14.9	11.97
THF	16.8	5.7	8	19.46	7.41
Water	15.5	16	42.3	47.81	20.94
CMP-BP-4	17.94	12.66	10.72	26.87	